AN INVESTIGATION OF THE HYDRODYNAMICS OF AIR LUBRICATION SYSTEMS AND THE DEVELOPMENT OF A SCALING TECHNIQUE FOR DIFFERENT DESIGNS AND OPERATIONAL CONDITIONS USING CFD

ANDREW SPITERI

A thesis submitted in partial fulfilment of the requirements for the degree of Doctor of Philosophy

April 2023

Abstract

An air lubrication system (ALS) is a green technology that has been increasing in popularity to reduce ships' emissions and improve their Carbon Intensity Indicator (CII) ratings. ALS works by injecting air underneath the hull of the ship, this modifies the turbulent boundary layer (T.B.L.) in a positive way and reduces drag. A full understanding of how this technology works and how it can be optimised is still not fully understood, due to a lack of research and many uncertain influencing variables. Also, currently, there is no clear and verified method of understanding how a scaling law can be applied to extrapolate results from model testing to full-size testing. A better understanding of the system would make ALS more efficient, optimisable at different operating conditions and a scaling law would be useful to extrapolate towing tank testing to full-size results, giving ship owners further trust in this technology.

A robust Computational Fluid Dynamics (CFD) methodology was first developed, this was done with extensive testing of boundary conditions, research on turbulence models and the addition of compressibility to the model. The CFD model was validated by comparing the behaviour and patterns from experimental results to other behaviours. Three types of testing regimes were undertaken: i) the same plate size with different depths to understand the effect of hydrostatic pressure, ii) three different plate lengths with different Reynolds numbers (Re) to understand the effect of Re, iii) three different plate sizes and depths that replicate a model test and a full-size model with a length of 65 m.

It was discovered that there is almost a linear relationship between drag reduction loss and an increase in hydrostatic pressure, with a statistical analysis r value > -0.954. A non-dimensional exercise was undertaken and whilst the final equation was not highly accurate, plotting the value of mass flow rate (MFR) and drag reduction resulted in a predictive model with over 86 % accuracy. Increasing the Re number up to $\mathrm{Re}\ x10^9$ resulted in a loss in the drag reduction effect for a mixing ratio, which is the ratio of air to water in the boundary layer, of 0.4, whilst results for a higher mixing ratio were more stable. Finally, three plate sizes were simulated representing a model size, full size and an in-between to fully understand what happens when scaling up an ALS. This resulted in an agreement of over 84 % from model scale to full scale. The difference in the drag

reduction effect is hypothesised to come from an increase in Re, an increase in turbulence and computational errors. It was concluded that when scaling up the technology the air injection area and the MFR should be scaled with the same scaling ratio.

Table of Contents

List of Tables

List of Figures

Nomenclature

α	Alpha – Void Fraction
μ	Dynamic Viscosity
σ	Sigma
λ	Scaling Factor
$\gimel$	Kinematic Viscosity
$\emptyset$	Air Layer Thickness
ρ	Density
δ	Boundary Layer Thickness
δ^*	Displacement Thickness
γ	Surface Tension
ε	Turbulent Kinetic Energy Dissipation Rate
l	Wall Unit
ω	Specific Dissipation Rate
‰	Salinity
μ_t	Turbulent Viscosity
ALDR	Air Layer Drag Reduction
ALS	Air Lubrication System
B	Width of Plate
BDR	Bubble Drag Reduction
B. L.	Boundary Layer

Ca	Capillary Number
C_f	Coefficient of Friction
CFD	Computational Fluid Dynamics
CII	Carbon Intensity Indicator
CO_2	Carbon Dioxide
D_i	Distribution of Injectors
D.R.	Drag Reduction
D	Bubble Diameter
D	Frictional Drag
DNS	Direct Numerical Simulations
EEDI	Energy Efficient Design Index
EEXI	Energy Efficiency Existing Ship Index
$F_{reduction}$	Reduction in Force
F_r	Froude Number
Fd	Froude Number for Drag Reduction
G	Gravity
GHG	Green House Emissions
Gt	Gross Tonnage
H	Hydrostatic Pressure
I_A	Injection Area
I_{AN}	Injection Angle

I_M	Injection Mode
I_x	Injection Location
K-H	Kelvin Helmholtz
IMO	International Maritime Organisation
ITTC	International Towing Tank Committee
L	Length
LES	Large Eddy Simulations
M	Mass
$\dot{m}$	Mass Flow Rate
Ma	Mach Number
MBDR	Microbubble Drag Reduction
MFR	Mass Flow Rate
N	Number of Prism Layers
NV	Numerical Ventilation
PCDR	Partial Cavity Drag Reduction
PIV	Particle Image Velocimetry
P. L	Prism Layers
Q	Bubble Volume Flow Rate
Q_a	Flow Rate Air
Q_w	Flow Rate Water
R	Stretch Ratio

R&D	Research and Design
RANS	Reynolds-averaged Navier-Stokes
Re	Reynolds Number
RST	Reynold Stress Transport
SST	Shear Stress Transport
T	Time
T.B.L.	Turbulent Boundary Layer
TKE	Total Kinetic Energy
U	Velocity
U_f	Flow Velocity
V	Velocity
V_a	Volume Air
VOF	Volume of Fluid
W	Width
We	Weber umber
W.S.A	Wetted Surface Area
Y+	Wall Distance

Dedication

This work would not have been possible without my supervisors Dr Milad Armin, Dr Eddie Blanco Davis, and Professor Jin Wang. Their constant support, help and respect motivated me to complete my research and create the best piece of work that I could. They have instilled in me a sense of commitment and professionalism that I am forever grateful for.

My parents have been a bastion of support and unconditional love and for this, I am forever indebted. Throughout my academic career, they have supported me constantly and they have sacrificed countless years of their lives to dedicate themselves to me.

Finally, I would like to dedicate my thesis to my late grandparents Vincent and Nazzarena Formosa of whom I am very proud. They grew up in war and poverty, starting with nothing. Despite their challenges, they raised a family with love and compassion. They installed in me values of respect, perseverance and resilience, values that I abide by every day, and I am very proud of.

"Ad Astra per Aspera"

1 Introduction

Shipping is the backbone of international trade as around 80 % of all global trade by volume and 70 % by value are transported via shipping (Sharifi *et al.* (2017)). Unfortunately, when comparred to other methods of transport such as rail or flight, its emissions are one of the highest. Previously international shipping's greenhouse gas emissions (GHG) were not considered threatening as shipping was thought to be the cleanest form of transportation. GHG refers to the release of gases that trap heat in the Earth's atmosphere, leading to an increase in global temperatures. The GHG emissions from shipping have increased so much that, shipping is now not considered as the cleanest form of transportation, and if shipping was treated as a country in 2015 it would have been the 6th largest emitter of energy-related CO_2 (Carbon Dioxide) Huang *et al.* (2016) as can be seen in Figure 1.

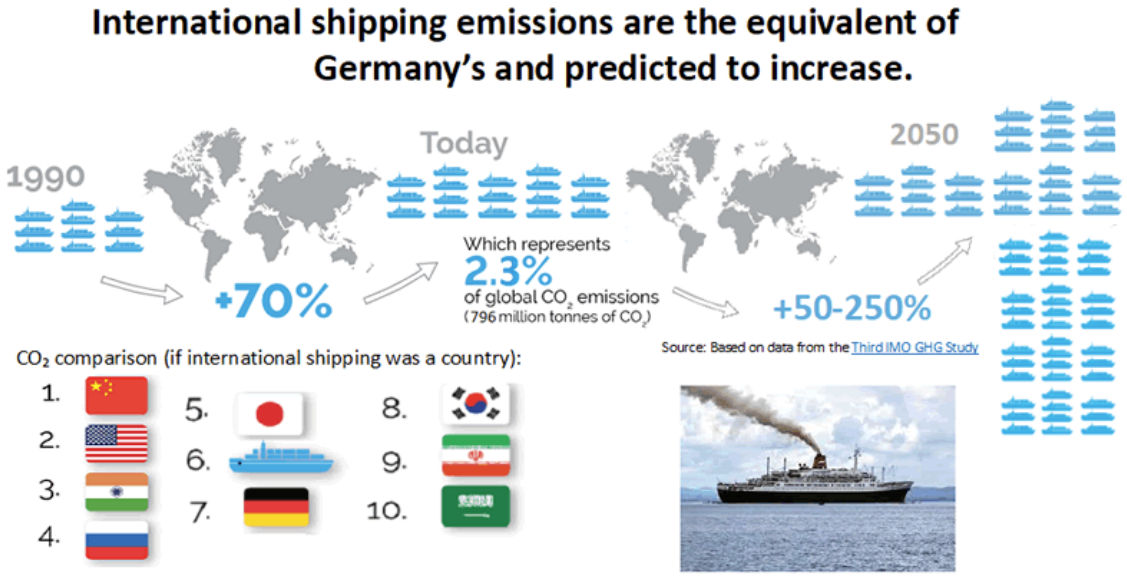

Figure 1: GHG Emissions (IMO, 2014)

To put shipping GHG emissions into perspective, the fuel consumption of ships excluding military in the year 2016 was around 250 mt. Considering that for every ton of CO_2 produced there is an increase of 5×10^{-12} °C, one billion tons of CO_2 raises the temperature by 0.005 °C every year (Busch *et al*. (2019)). These numbers are estimated to increase exponentially by 150 – 250 % by 2050 if no action is taken (Lindstad *et al.* (2011)).

With the Paris agreement aiming to keep the global average temperature below 2°C from pre-industrial levels, and to cap the overall temperature increase to 1.5°C, there has been a lot of work and effort to reduce GHG on all fronts (Nations, 2015). Since international shipping is excluded from the Paris agreement the International Maritime Organization (IMO) has set up its strategy (ICCT, 2017). This strategy aims to reduce annual international shipping GHG emissions to half of what they were in 2008 by 2050 and later phase out GHG emissions by 2100 as can be seen in Figure 2 (IMO, 2018).

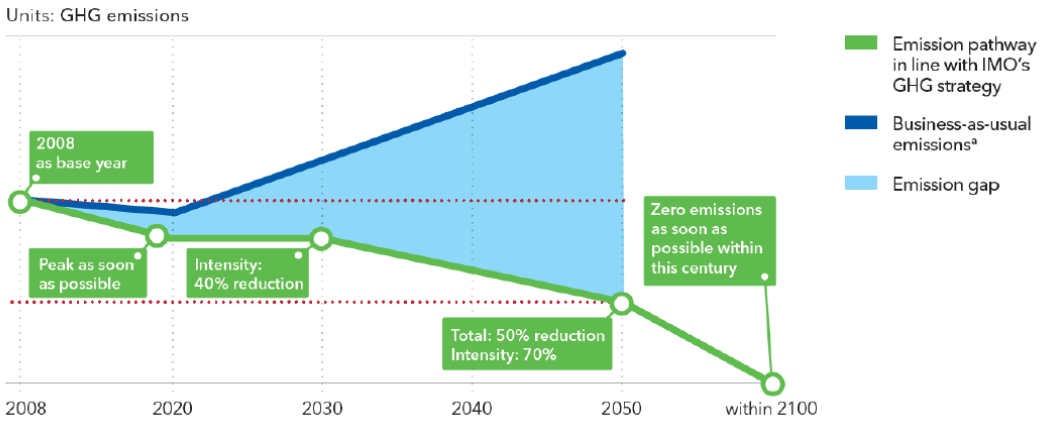

Figure 2: IMO Pathway to Zero Emissions (IMO, 2018)

Currently around 21 % of the top 30 shipping companies in every sector have a pledge for decarbonisation as can be seen in Figure 3 (Møller and Carbon, 2022).

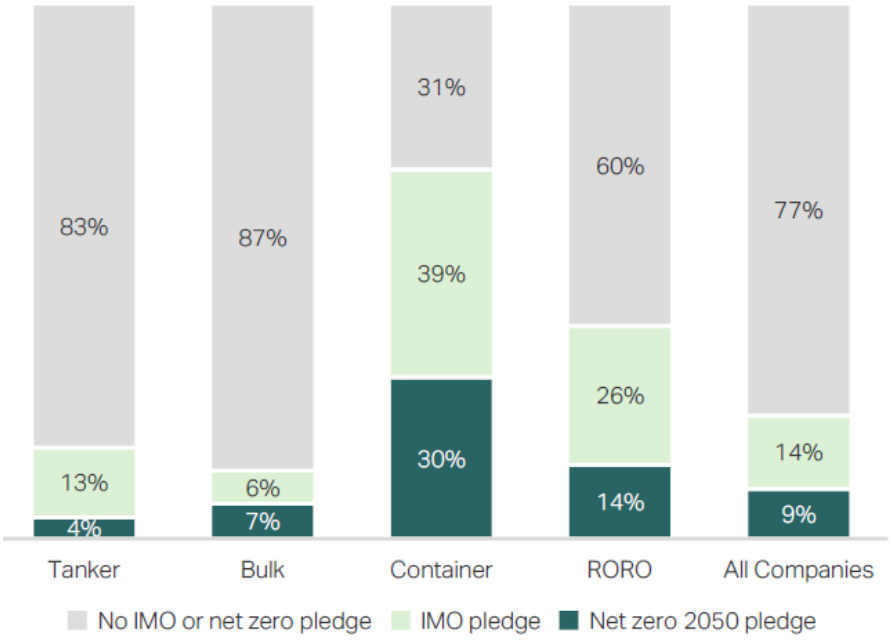

Figure 3: Shipping Companies That Have a Pledge for Decarbonisation (Møller and Carbon, 2022)

To help achieve this IMO has come up with three different indexes which are Energy Efficient Design Index (EEDI), Energy Efficiency Existing Ship Index (EEXI), Carbon Intensity Indicator (CII) (DNV, 2021).

EEDI aims to reduce fuel consumption and emissions by measuring the carbon emissions per unit of transport work. Ships built after 2013 must meet an EEDI level and every five years this level is increased. After the year 2025, all ships have to have a reduction of *30* % from an average of between 2000 and 2010 (IMO, 2011).

The EEXI is related to the technical design of a ship, and it measures the energy efficiency of existing ships. A ship must attain an EEXI approval once in its lifetime till 2023. The EEXI Value is determined by the type of ship, its capacity, and its propulsion. Every ship has a different EEXI value and must be calculated to see if it is within the EEXI value or not. If the ship is not within the EEXI calculated value then a number of mitigation actions are required (DNV, 2021). Both the EEDI and EEXI apply for ships over 400 gross tonnage (Gt)

CII is intended to measure how efficiently a ship can transport its goods or passengers. The value is calculated as CO_2 emitted per cargo-carrying capacity and nautical mile. Ships will be given a rating from A-E and the rating threshold will become more and more difficult going on to 2030 as can be seen in Figure 4. CII with be enforced in 2023 on all cargo, RoPax and cruise vessels above 5,000 Gt and trading internationally. The CII will become stricter by 2 % every year (DNV, 2022).

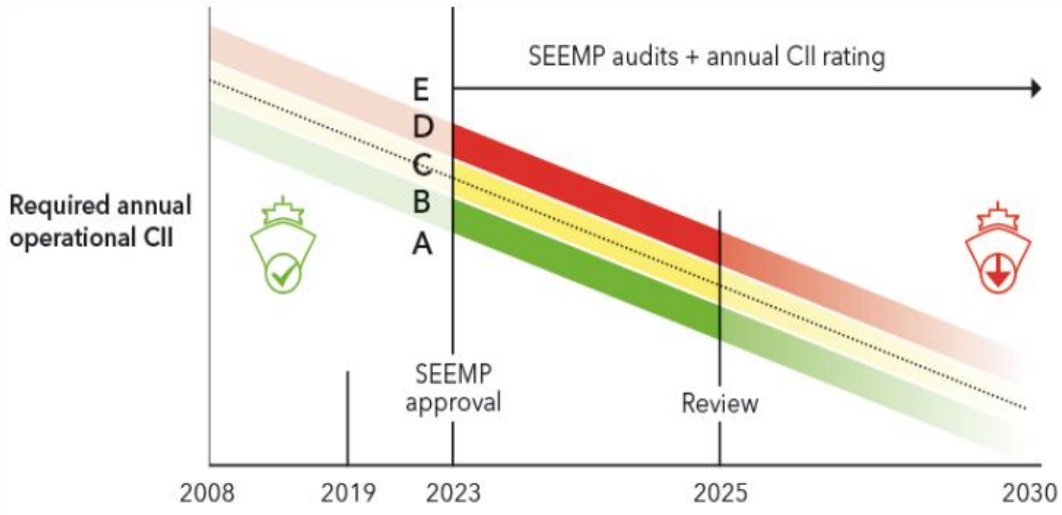

Figure 4: CII Rating (DNV, 2022)

1.1 Drag in Ships

When there is a fluid-solid interaction there will always be a resistance to fluid flow which is identified as drag (Goolcharan, 2016). The higher the resistance the higher the energy need and consequent emissions to propel the ship forward. These can be divided into two forces :

- Wave-making
- Skin-friction *(Mäkiharju et al*. (2013)).

Wave-making resistance is the resistance created due to the formation of waves as the vessel moves through the water. The waves created generate a pressure difference between the front and the back of the ship which create resistance. Skin friction is a type of hydrodynamic drag that can be split into two parts: viscous drag and pressure drag. Pressure drag is related to the pressure distribution around the ship's hull (Terziev, *et al.* (2022)). Pressure variations along the surface of the hull create eddies and turbulence in the water, which in turn then create resistance. The viscous drag force on ships refers to the resistance that a ship experiences as it moves through water due to the friction between the water and the surface of the ship. This is the most dominant component is skin-friction drag. This type of drag is caused by the viscosity of the water, which is a measure of its resistance to flow. The viscous drag force on a ship increases with the speed of the ship and the wetted surface area (W.S.A) of the ship that is in contact with the water. It also depends on the roughness of the ship's hull and the viscosity of the water. As a high Re is achieved by an increase in speed, the flow near the ship becomes more turbulent and the B.L. thickness increases. This leads to an increase of the shear stress acting on the wetted surface of the hull (Zhang, *et al.* (2019)) .

The pressure drag force can be reduced by designing the ship's hull to be more streamlined and smoother, and by using materials that are more resistant to friction such as coatings. Throughout time, many studies have tried to reduce skin friction drag with a wide spectrum of different results. Estimation shows that around 60 % of all propulsive power is used to overcome this friction (Zhang *et al.* (2019)) and (Liu *et al.* (2019)).

Another method to reduce skin friction is to reduce the drag around the W.S.A. This can be done either passively or using an active method (Sharifi *et al.* (2017)) and (Yao *et al.* (2011)).

Passive methods are those methods that do not need a continuous energy source to work like riblets, polishing and drag reduction coatings. On the other hand, active methods such as air lubrication drag reduction, require a continuous energy to supply the injection of air to reduce the wetting area or the effect of viscosity at the B.L. It has been noted that although active methods need a source of energy to reduce drag, this reduction of drag is more than that of passive methods (Yao *et al.* (2011)). The problem with this is in some cases the total saving is minimal due to the energy needed to operate the system and maintain it.

1.2 Air Lubrication Drag Reduction

This project will investigate the method of air lubrication drag reduction (ALDR) as a method of how to reduce viscous drag. Air lubrication is a technology that can be used to reduce the drag on ships, which can help to improve their fuel efficiency and reduce their environmental impact. It works by using a system of air blowers and nozzles to blow a thin layer of air bubbles onto the hull of the ship, which creates a layer of air between the hull and the water. This layer of air acts as a lubricant, reducing the friction between the ship and the water, modifying the turbulence in the B.L. and thereby reducing the drag on the ship. There are several different types of air lubrication systems, including surface effect air lubrication, submerged air lubrication, and hybrid air lubrication. Each of these systems has its own unique set of advantages and disadvantages, and the most suitable option for a particular ship will depend on a variety of factors.

In most cases air is injected most frequently through a slot, porous material, or a perforated plate. This method reduces the density of the water as it creates an air-water mixture and modifies the turbulent momentum transport. Since the bubbles are sometimes very small compared to the B.L. this process is sometimes referred to as micro bubble drag reduction (MBDR) (Mäkiharju *et al*. (2013)). Multiple researchers have agreed that as the void fraction increases, that is, the amount of air in the water, the drag decreases. Hussan *et al.* (2008) stated that with micro bubbles the reduction

can decrease by up to 70 %, whilst Verschoof *et al*. (2016) found that using a volume per cent of more than 4 % bubbles can lead to a drag reduction of up to 40 %.

1.3 Statement of Problem, Aim and Objectives

Since ALDR is an active method of reducing drag using compressors it is important to understand how the drag reduction effect works and how it can be optimised when subjected to different hydrostatic forces. It is known that no verified scaling law exists that also scales up the required flow rate. Therefore, results from model testing cannot be extrapolated to full size results. There is also a gap in knowledge when explaining how hydrostatic depth changes the drag reduction effect.

To support this research idea, the specialist committee on energy saving devices also highlight the gap in knowledge in the scaling law, therefore currently large deviations may result in extrapolation data. They also suggest that CFD testing is more valuable than towing tank testing, that CFD could be used to understand the dynamics of scaling up and that the performance of full scale ALS cannot be evaluated from the model size (ITTC, 2021).

Therefore, the aim of this work is as follows:

To investigate how air lubrication systems can be designed and operated under different conditions through modelling of their hydrodynamic behaviour.

To achieve the aim of the research the following objectives are to be understood:

1. To understand how hydrostatic depth and operating conditions effects the drag reduction effect of ALS.
2. The understand the effect of flow rates and mixing ratios on drag reduction.
3. To create a mathematical and CFD scaling technique
4. Use the data created as a possible predictive model.
5. Developing knowledge on how to model ALS with CFD and capturing different behaviours.
6. To give insight on how scaling practices should be done.

The novelty of this work is not only the objectives, but it will also give researchers and technology providers further insight on how to:

- Model ALS systems on CFD using a RANS solver and incorporating compressibility. Which to the authors best knowledge this is the first time that this is being investigated.
- An insight into how different flow rates effect drag reduction across different operating conditions
- Adjust flow rates based on the compressibility of air and changes in density at different depths.
- Optimise their system based on a ship operating condition.
- Use developed methods or calculations from this work in their processes.
- Gather a better understanding of the behaviour of ALS.

1.4 Structure of Thesis

This thesis is divided into five chapters including this chapter which is a brief introduction to the background of research, problem statement, aims and objectives.

- Chapter 2 is an in-depth literature review that focuses on studies done to understand ALS both experimentally and using CFD. Different theories on why a drag reduction is created when injected air are presented. Also, this chapter highlights the difficulties and limitations of understanding ALS. Finally, two case studies are given.
- Chapter 3 explains the methodology section of the thesis. The methodologies are divided into two sections . A numerical set up methodology and a testing methodology. The testing methodology is then divided into three separate testing regimes. The theory of how these methodologies were chosen are described in this chapter.
- Chapter 4 is the results and discussion section. This chapter includes the results from the three testing campaigns, a non – dimensionless exercise and a statistical analysis of the results. The results lead to developing a new constant sigma which can be used to define a mass flow rate for a drag reduction and a predictive model to understand how hydrostatic pressure effect drag reduction.
- The final chapter 5 is the conclusion and future work. The conclusions summarise the main findings of this thesis and further research ideas are proposed to further enhance the scaling law and the predictability of the model created.

2 Literature Review

2.1 Introduction

The use of air layers to reduce the viscous friction of hulls has been around since the 19th century when most of the studies were done on small high-speed crafts (Sindagi *et al.* (2019)). In small crafts, the hull shape is designed such that air passes under the hull and lifts the surface upward creating a planing effect, as well as reducing the wetting area (Ghassemi *et al.* (2015)). Whilst on ships air is injected through the bottom to create a B.L. of air to reduce the wetted area thus reducing frictional contact (Vijayan *et al.* (2018)) and (Jang *et al.* (2014)). Near-wall density, viscosity, and the turbulence of the B.L. also change, aiding in the reduction of drag (Sindagi *et al.* (2019)).

Throughout the years, various techniques have been proposed aiming to reduce frictional drag. In 1875, William Froude initiated the idea of reducing frictional drag between a water flow and a solid surface using a gas layer. Later this concept was patented by Laval in 1883.

Using electrolysis to generating microbubbles McCormick *et al.* (1973) were able to show a significant drag reduction effect on a submersible hull. This led to a number of laboratory tests between 1980 and 1990 using tunnels and water channels (Madavan *et al.* (1984)), (Merkle *et al.* (1990)) and (Madavan *et al.* (1985)) with the aim of understanding this effect and its variables.

The application of ALS on ships started around the late 2000's with the drive for cleaner ships and more regulations coming into force with testing being done in lakes as well as open waters (Ceccio *et al.* (2012)), (SilverStream, 2019) and (Foeth *et al.* (2009)). Nowadays ALS is considered a leading technology for emission reductions.

2.2 Air Lubrication Techniques

There are three main different air lubrication techniques. These are (Mäkiharju *et al.* (2013)):

- Bubble Drag Reduction (BDR) or MBDR
- Air Layer Drag Reduction
- Partial Cavity Drag Reduction (PCDR).

Figure 5 explains the difference between the air lubrication techniques and shows the three air lubrication regimes that are derived from the main lubrication techniques.

Terwisga (2016) divides air lubrication into two types. These are 'stratified' and 'dispersed' as can be seen in Figure 6. A stratified regime is considered as a constant air layer whilst the dispersed air regime is noted to be a liquid saturated with gas. The stratified is considered to be the best for the reduction of frictional drag (Terwisga, (2016)).

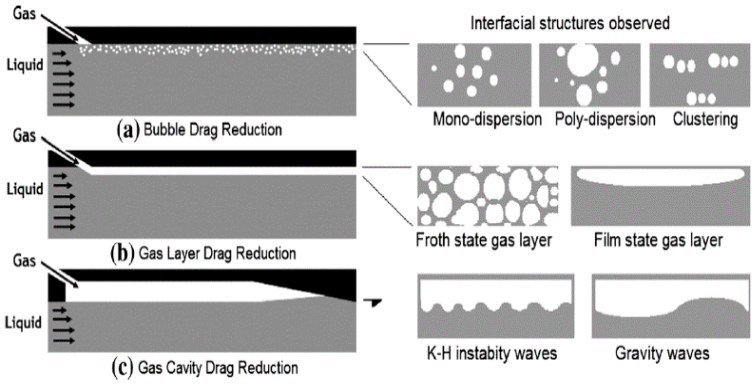

Figure 5: Air Lubrication Regime (Mäkiharju et al. 2013).

One downfall of this technology is that several compressors must be used to supply the injected air. Injecting bubbles using conventional compressors can amount to around 3-10 % of total energy consumption by a ship (Kumagai *et al.* (2015)). If a constant air layer is supplied this value would be much higher, therefore BDR is most frequently used in industry. This is where the focus of this work will be.

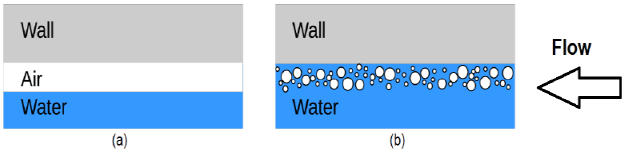

Figure 6: Air Lubrication Regimes (Terwisga, 2016).

2.3 Mechanics of Bubble Drag Reduction

The principle of drag can be understood using Equation 1

$$D = C_f \times 0.5 \times \rho \times U^2 \times W.S.A \qquad (1)$$

were, D is frictional drag, C_f is coefficient of friction, ρ is density, U is velocity and $W.S.A$ is wetted surface area. The coefficient of friction is a dimensionless value that represents the ratio of friction between two surfaces. With the introduction of bubbles into the B.L. the wetted surface area, density, and the velocity of the fluid next to the B.L. will reduce.

$$\tau_w = \nu \frac{\partial u}{\partial y} - \rho U'V' \tag{2}$$

Equation 2 is the equation of wall shear stress due to viscosity were, τ_w is the wall shear stress, ν is the kinematic viscosity, y is the wall distance, u is the velocity and $U'V'$ are a relation to Reynold's stress. Wall shear stress is a type of shear stress that occurs at the walls of a vessel. It is the force per unit area exerted on the wall of the vessel by the fluid or gas flowing next to it. In the case of ships, wall shear stress is typically caused by the water flow around the hull of the vessel as it moves through the water. Factors that can affect wall shear stress on a ship include the shape and size of the hull, the speed of the vessel, and the characteristics of the water in which the ship is operating. As the density and dynamic viscosity decreases the wall shear stress value drops as well, resulting in a drop in drag force (Sindagi *et al.* (2019)).

Now C_f can be calculated as seen in Equation 3.

$$C_f = \frac{\tau_w}{0.5 \times \rho \times U^2} \tag{3}$$

Therefore, it can be assumed that the reduction in drag is due to:

- Reduction in effective density
- Modification of turbulent B.L.
- Reduction in viscosity (Vijayakumar *et al.* (2020)).

Numerous studies have been done to measure the resultant drag force reduction. Ali *et al.* (2010) found that on flat plates that were equivalent to the wetted surface of a ship, higher drag reduction could be achieved on a lower Froude number (Fr). Hussan *et al.* (2008) stated that with microbubbles the reduction can decrease by up to 70 %, whilst

Verschoof *et al.* (2016) found that using a volume per cent of more than 4 % bubbles can lead to a drag reduction of up to 40 %.

A study done by Karniadakis *et al.* (2002) indicated that the drag reduction is due to at least three mechanisms, these being:

1. The initial injection of the micro bubbles.
2. The density effect.
3. The effect the bubbles have on the liquid turbulence

Researchers have proven that the introduction of air reduces the density of the fluid, and dynamic viscosity as can be seen in Figure 7 and Figure 8 at the surface of the hull leading to a reduction in drag (Goolcharan, 2016). In Figure 7 the dynamic viscosity is seen to reduce by 13 %.

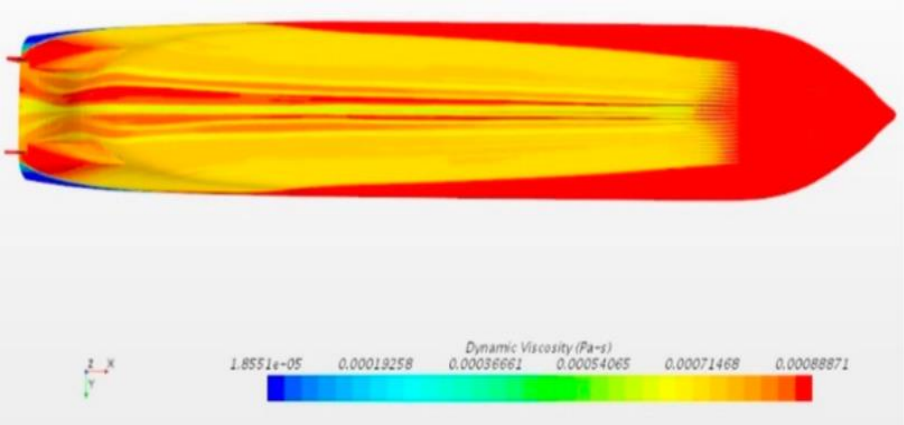

Figure 7: Dynamic Viscosity (Sindagi et al. 2019).

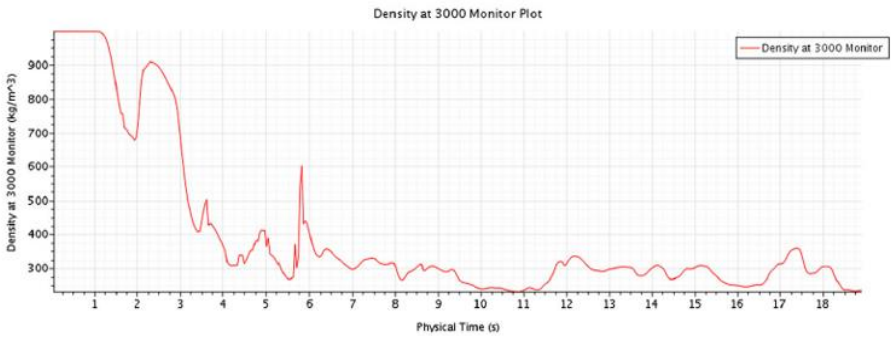

Figure 8: Density Drop When Air Is Introduced (Sindagi et al. 2019).

Some researchers believe that drag reduction is based upon the assumption that the formed bubbles move along the hull creating a slip-like condition (Kinzel *et al.* (2017)) , (Perret *et al.* (2015)). In fluid dynamics, slip refers to the difference in velocity between a fluid and a solid boundary with which it is in contact. Slip is important because it affects the amount of drag experienced by an object moving through a fluid, and it can also influence heat transfer between the solid and the fluid. There are several factors that can influence slip in fluids, including the properties of the fluid itself such as its viscosity, the geometry of the solid boundary, and the nature of the forces acting on the fluid. In some cases, the slip velocity between a fluid and a solid boundary can be described using the Navier-Stokes equations, which are a set of equations that describe the motion of fluids.

Since the bubbles have lower shear stress than most solids the resultant net shear stress is reduced. In some work, it is thought that the introduction of air reduces the overall viscosity of the B.L. and hinders turbulence production near the hull (Stephani *et al.* (2006)),(Hussan *et al.* (2008)) and (Jiménez *et al.* (1999)).

Hassan *et al.* (2006) reported that the increase of microbubbles within a B.L. is inversely proportional to the Reynolds stress. Reynolds stress measures the turbulent fluctuations in a fluid flow. It is responsible for the transfer of energy from large scales to small scales in fluid flow. This also holds for turbulence production. As more air is introduced the turbulence production is delayed (Stephani *et al.* (2006)).

According to Mengs *et al.* (1989) when bubbles split they do so by extracting turbulence energy, therefore reducing turbulence. Turbulence energy is the amount of kinetic energy present in turbulent flow. It is measured in turbulent kinetic energy (TKE), and it is the sum of the kinetic energy associated with the velocity fluctuations, related to the Reynolds stress. TKE is generated by the action of large-scale velocity fluctuations which are transferred to smaller scales via cascading. Later this was proven to be true when a particle image velocimetry (PIV) technique was used by Jacob *et al.* (2010)). Additionally, it was found that the flow velocity gradient changes in the turbulent layer. This could be because bubbles migrate into vortical structures thus disrupting them (Wendy *et al.* (2006)), (Murai, 2014) and (Elbing *et al.* (2008)).

When testing a 50 m long plate that had a scale close to that of a ship, Kodama *et al.* (2000) found that drag reduction with microbubbles is possible for large plates. Microbubbles on large surface roughness were tested by Deutsch *et al*. (2003) and they found that the drag reduction is even better on rough surfaces as bubble tend to stick to the surface prolonging their induced effect.

Madavan *et al.* (1985) discovered that for a flat plate with a length of 50 m, a drag reduction of 32 % was achievable. Watanbe *et al.* (1998) also found that a drag reduction was possible for large plates. It was also found that a drag reduction of between 50-90 % on a flat plate was possible (Merkle *et al.* (1990)).

2.3.1 Bubble Size, Bubble Behaviour, and Effect on Drag Reduction

Some researchers argue that there is an optimal bubble size in the micro-metre size. Others argue that in high Re environments of up to 25 million, any size of bubbles from 250 to 1000 μm have little significance on drag reduction results. The bubble sizes were found to be in relationship with the inlet velocity, B.L. thickness and as well as the salinity of water (Sayyaadi *et al.* (2013)) and (Wendy *et al.* (2006)). What most researchers agree on is that there has to be a relationship, that has not been defined as of yet, between flow and bubble size (Hussan *et al.* (2008)). It is important to note that the bubble size is not decided by the injection hole but by the air flow rate and the velocity in the B.L. (Ceccio, 2010). Since many researchers have opposed views on what the optimal bubble size is, this research will focus more on the flow rates being injected as it is a more controllable feature and as researchers have discussed a factor of the bubble size is the injected flow rate.

Merkle *et al.* (1990) showed that changing the size of the bubbles affected the drag reduction. The diameter of the bubble affects the trajectories which then affect the position in the B.L. Whilst, Moriguchi *et al.* (2002) discovered that air bubble diameter is dependent on flow velocity and the overall diameter has no effect on the drag reduction. On the other hand Winkel *et al.* (2004) found that bubble diameter is inversely proportional to salinity and that bubble size has a significant effect on MDBR. Takahashi *et al.* (2001) researched BDR at a Re of 25 million and found that bubble size and B.L. thickness did not have a significant effect on the drag reduction achieved. Tsail *et al.* (2011) and Kawamura *et al.* (2002) discovered that bubble sizes ranging from 0.05

mm to 2 mm did not affect drag reduction, but their volume within the B.L. was what affected drag reduction. Work done by Zhao *et al.* (2022) suggests that small bubbles will increase the D.R. effect whilst larger bubbles can even increase the overall drag.

It has to be said that although there is a vast body of literature talking about bubble size and the positions of bubbles within the B.L., the difficulty of accurately capturing and measuring the bubbles has to be kept in mind (Hashim *et al.* (2015)). When considering the scales of micro and nano bubbles, and the inaccuracies of capturing bubble image, physical testing can give little insight into what is the optimal size. More effort should be made in working in air to water ratios as these can be easily calculated and controlled.

Lu *et al.* (2005) and Kitagawa *et al.* (2005) agree that the drag reduction effect is related to bubble deformation. When the bubbles are in a T.B.L., a behaviour of bubble splitting and coalescence will occur. Bubble coalescence is a phenomenon were multiple bubbles merge into a bigger one. When two bubbles come into contact, the surface tension creates a force that pulls the bubbles together. As the bubbles merge, their surfaces fuse, and the total surface area decreases. This process can continue until the bubbles form a single large bubble. This process is dependent on the flow velocity, impurities in the water and the turbulence within the T.B.L. (Perret *et al.* (2015)).

As the bubbles move away from the injector the population of the bubbles and their size will vary due to the downstream distance and B.L. flow speed. Using Equation 4 the maximum stable bubble size D_{max} within a T.B.L. can be related to the fluid density ρ, surface tension γ and turbulent kinetic energy dissipation rate ε. The bubble diameter is also dependent on the vertical location of the bubble withing the T.B.L. (Hinze, 1955). If bubble size is proven to be an important factor in drag reduction Equation 4 proves that the breakdown of T.K.E is an important factor D.R.

$$D_{max} \approx \left(\frac{\gamma}{2\rho}\right)^{\frac{3}{5}} \varepsilon^{-\frac{2}{5}} \tag{4}$$

When the bubbles split, the diameter is reduced making the bubbles smaller. When the bubbles become smaller, they will be pushed away from the wall due to buoyancy effects and turbulent eddies. This will result in a restoration of the T.B.L. and reduction

of void fraction. As the smaller bubbles escape the T.B.L. further away from the injection point, only the larger bubbles will be left, leading to an overall reduction of void fraction and bubble concentration (Kawamura *et al.* (2003)). The higher the Re, the higher the turbulence shearing effect and bubble breaking; therefore, bubble escaping will increase. This can result in a problem of persistence down stream of injection (Pavlov *et al.* (2020)).

Sanada *et al.* (2009) observed that the bubble trajectory and its place within the T.B.L. is strongly dependent on the Re. Legendre *et al.* (*2*003) used Direct Numerical Simulations (DNS) to model two spheres to study their relative motion and direction. It was concluded that direction and motion changed in accordance with the Re.

Kawamura *et al.* (2002) concludes that as the bubbles flow away from the injector they converge to an equilibrium value that is dependent on the local shear rate. Splitting takes places at around 1 – 10x the B.L. thickness while coalescence takes place at 100 x the B.L. thickness.

Hassan *et al.* (2006) reported that an increase in microbubble concentration leads to a reduction in the Reynolds stresses and turbulence production in the B.L. Sindagi *et al.* (2019) stated that the drag reduction by MBDR is due to alteration of the viscosity density of the fluid in the B.L. These changes reduce the Reynolds' stresses which reduce shear stress. Work done by Gao *et al.* (2023) states that the existence of bubbles within the B.L. reduces the effect of formation and development of turbulence, if the air is injected in the laminar region.

Work by Hara *et al.* (2011) used image analysis to study frictional-drag reduction by microbubbles in a turbulent channel flow and found that the oscillatory motion in the vertical axis reduced the Reynolds stresses near the wall. It has been found that viscosity decreases for a small portion of air, but at a high Re, the turbulent stress has greater importance on drag than viscous stress. Kitagwa *et al*. (2004) and Ferrante *et al.* (2004) discovered that the bubbles introduced deform in a favourable orientation to the flow reducing turbulent stress.

Studies have shown that bubble splitting in the B.L. reduces the turbulence energy. When the turbulence energy is suppressed the turbulence withing the T.B.L. is also

supressed. This makes the condition within the B.L. to be more favourable for bubbles. (Hashim *et al.* (2015)), (Ferrante *et al.* (2004), (H.Miyata, 2001) and (Xu *et al.* (2002)).

Sanders *et al.* (2006) proves that the shear flow of the B.L. will not let the bubbles be in contact with the hull. The bubbles will be suspended at a location underneath the surface unless the bubbles coalesce and stratify. This thin layer of liquid between the hull and bubbles is sometimes called "liquid layer" and can be seen in Figure 10 (Elbing *et al.* (2008)).

Figure 9 is a schematic drawing of how bubbles influence the B.L. once injected. Part A shows how initially the B.L. is divided into a viscous sub layer, buffer layer, outer layer and finally the flow region. Part B demonstrates how another layer is added, that of the bubbly two-phase layer between the outer layer and buffer layer (Adrian, 2007). This agrees with the findings from Madavan *et al.* (1984)), (Merkle *et al.* (1990)),(Miyata, 2001) and (Hussan *et al.* (2008)) were it was deduced that the concentration increases away from the wall up to a peak value, then decreases to zero once in the free stream.

Fully understanding the size of bubbles on drag reduction is limited as bubbles immediately break up or coalescence and there is no way of controlling them within the B.L. (Kawamura *et al.* (2002)). This difficulty in understanding the effect of bubble sizes behaviour within the B.L. further highlights the need to put more effort in understanding the effects of flow rates rather than bubble sizes.

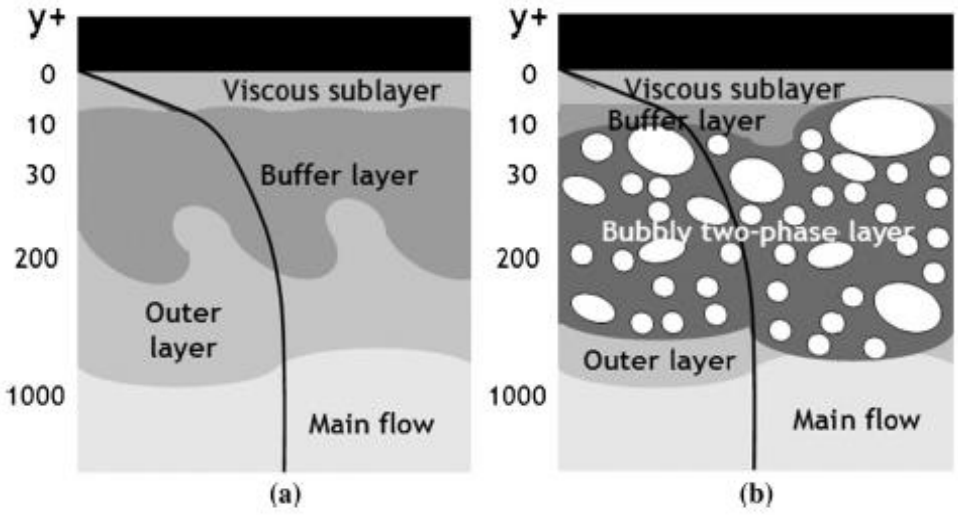

Figure 9: Boundary Layer With And Without Air Injection (Adrian, 2007)

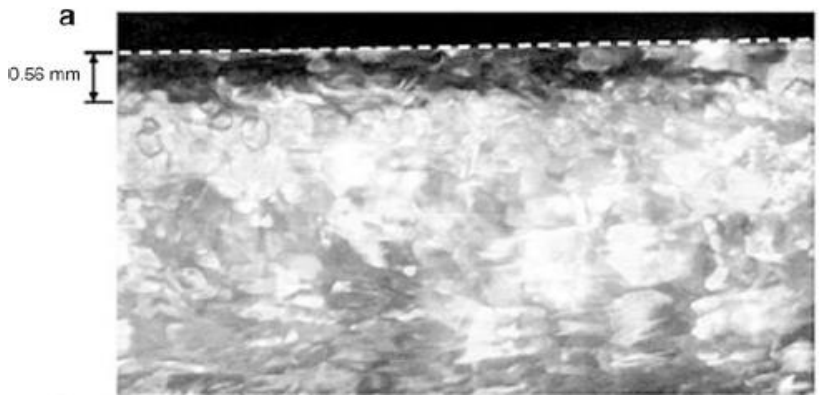

Figure 10: Observing The Liquid Layer (Elbing et al. 2008)

2.3.2 Dimensions of Wetted Surface Area

Work done by Sindagi *et al.* (2019) shows how the coefficient of friction (CF) increases further away from the injection both longitudinally and transversely as can be seen in Figure 11.

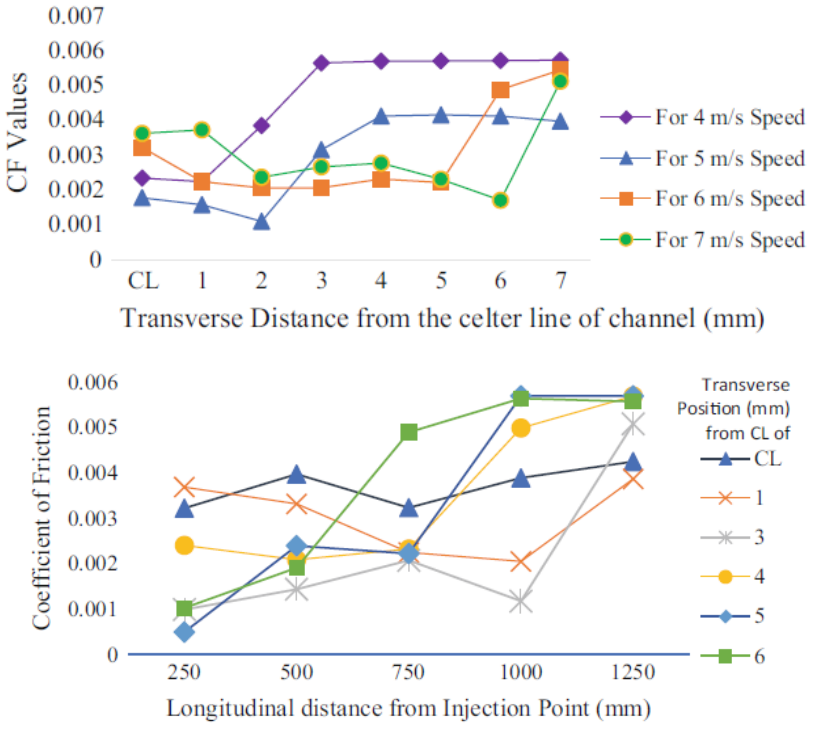

Figure 11: Increase Of Coefficient Of Friction With Distance From Injector (Sindagi et al. 2019)

Kodama *et al.* (2002) showed that drag reduction in the spanwise direction is not uniform and it decreases further away from the centreline of injection. Sanders *et al.*

(2006) and Elbing *et al.* (2008) reported that the drag reduction effect is lost the further downstream the drag is measured. This was thought to be due to the near-wall shears in the B.L. This wall shear makes the bubbles move from the wall's surface. Harleman (2012) later confirmed this. Therefore, the shape with respect to the injection point is also an important parameter. Jang *et al.* (2014) did a study whereas a side wall of 10 mm height was put on a flat plate to avoid bubble escaping and using a side wall proved to be more effective.

2.3.3 Air Injection and Volume Fraction

The influence of the void fraction has been discussed greatly as well. The void fraction is a measure of the empty space or "void" in a material. It is expressed as a ratio of the volume of the void space to the total volume of the material. In this research the void fraction is a ratio of air to water. Many researchers agree that increasing the void fraction of air decreases drag. However, it was stated by H.Miyata *et al.* (2001) that this only holds if the fraction of air increases near the wall, and Deutsch *et al.* (2003) say that there exists a point, at which once exceeded, the addition of more air starts reducing the effect of drag reduction. For MBDR to be as efficient as can be the air injection rate has to be optimised Kodama *et al.* (2000)).

A study done on a 70 cm catamaran model by Sayyaadi *et al.* (2013) found that there exists an optimum injection rate, and once this injection rate is exceeded there is a reduction in a drag effect. Tsai *et al.* (2011) discovered that an increase in air injection is equal to an increase in drag reduction up to a certain limit. It was discovered that for every velocity there exists an optimal injection rate. If this injection rate is exceeded the drag reduction effect starts to decrease. This theory is supported by many researchers as well (Shereena *et al.* (2014)), (Latorre, (1997)) and (Jang *et al.* (2014)).

It can also be noted that for almost all experimentation the higher the speed the less the drag reduction. There seems to be a point were increasing speed seems to reduce drag reduction. This could be due to the fact that as the velocity of the vessel increases the wave making resistance component of the ship increases, reducing the viscous friction part (MARIN, 2011) (Yao *et al.* (2011)), (Sayyaadi *et al.* (2013)), (Tsai *et al.* (2011)), (Kodama *et al.* (2000)), (Sindagi *et al.* (2019)) and (Wu *et al.* (2008)) all reported this. Turbulence also plays a big part as the vessel goes faster the turbulence will

increase and the bubbles will get sucked out of the B.L. It should be added that in most studies the injection ratio is kept the same and the velocity of the water or model is increased. This velocity increase changes the B.L. thickness and profile, as the B.L. is dependent on the velocity as can be seen in Equation 16, and hence the ratio of air to B.L. thickness. Therefore, a higher velocity means that the air to water mixing ratio is decreased leading to a less drag reduction.

Till now there is no correct way to estimate the air injection rate, but it can be evaluated as an index of boundary water flow. This can be calculated by using common turbulent fluid relations (Sayyaadi *et al.* (2013)).

Equation 5 explains alpha (α) is the ratio of injected flow rate (Q_a) over water flow rate (Q_w) inside of the B.L.

$$\alpha = \frac{Q_a}{Q_w} \tag{5}$$

Equation 6 shows that using the turbulent boundary theory the water flow rate can be calculated.

$$Q_w = U_f \times (\delta - \delta^*) \times B \tag{6}$$

Solving Equations 5 and 6 results in Equation 7 from the work of Sayyaadi *et al.* (2013) which includes the parameters of a flow as can be seen in Table 1.

Table 1: Table of Flow Parameters

Parameters of a flow	
B	Width of Plate
U_f	Flow Velocity
δ	Boundary Layer Thickness
$\gimel$	Kinematic Viscosity
L	Length of Plate
V	Velocity of Plate
W	Width of Plate

$$Q_w = 0.293 \times L^{0.8} \times \gimel^{0.2} \times V^{0.8} \times W \tag{7}$$

Figure 12 shows that the optimal injection rate varies between 0.4 and 0.6; this is also recorded by (Latorre, (1997)) .

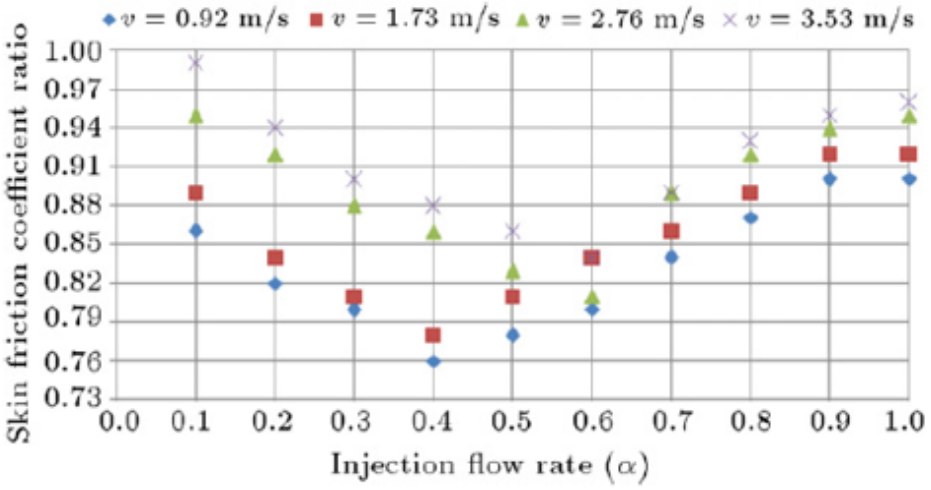

Figure 12: Ratio Skin Friction vs. Injection Rate for Four Different Velocities (Sayyaadi et al. 2013).

2.4 Hydrostatic pressure

Hydrostatic pressure is the pressure exerted by a fluid at rest due to the force of gravity. It is proportional to the depth and density if the fluid. Pressure also plays a big part in the drag reduction effect. Full-scale trials on the Pacific Seagull and M.V. Soyo showed that at a fully loaded state the drag reduction effect is less. From 10 % to 5 % and from 5 % to 3 % respectively. At a fully loaded state, the vessels sit lower therefore there is larger hydrostatic pressure acting on the hull (Hoang *et al.* (2009)) and (LTD, (2014)). Ceccio *et al.* (2010) discovered that for air injection that is transitional i.e., starts as an air layer and ends up as a bubble and a fully developed layer, the effect of depth at slow speeds results in an increase of power needed via the compressors. This can be seen in Figure 13.

Ceccio *et al.* (2010) state that the work done by a pump to inject air at a given depth increases around the square of the ship's draft. This higher hydrostatic pressured then leads to the compressibility of air and a higher mass flow rate is needed to supply air at a given rate.

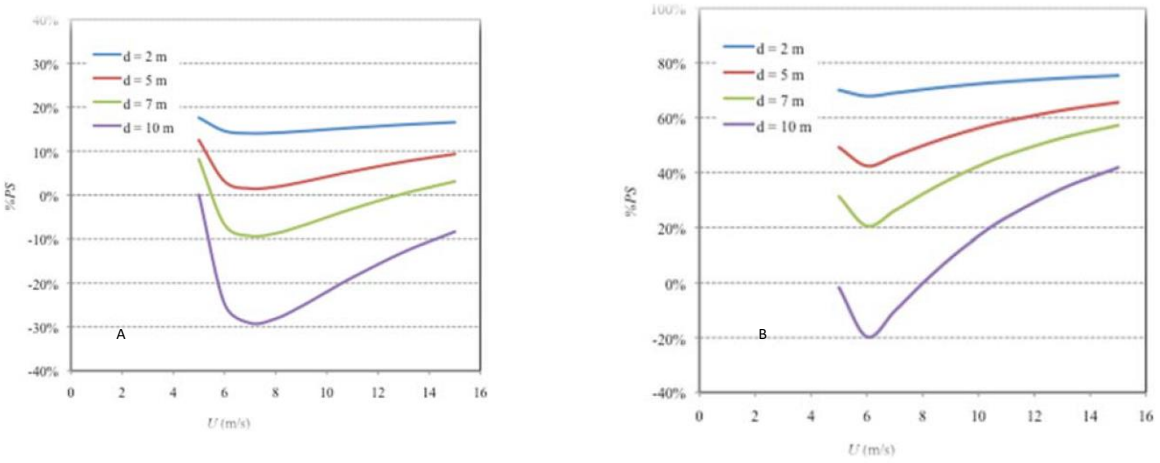

Figure 13: A) Transitional Air Layering and B) Fully Developed Air Layer At Different Depths (Ceccio et al. 2010).

Kodama *et al.* (2000) suggested that the Fr based on the depth of water should be calculated as seen in Equation 8, with F_d being the Froude number for depth, U the velocity, g is gravity and D is depth. The higher the Fd number the higher the D.R. effect. From the equation it can be noted that increasing the depth (D) of the water will reduce the Fd number hence reducing the drag reduction effect.

$$F_d = \frac{U}{\sqrt{gD}} \tag{8}$$

As the hydrostatic forces with depth increase on the bubble the forces acting on the bubble change. Therefore, the buoyancy force and size of the bubble will change. As the size of the bubble changes the ratio of the bubble layer thickness to the B.L. changes. This is one of the main problem when it comes to scaling (Murai, (2014)).

2.5 Density Ratio

A parametric study showed that decreasing the density of injected gas increased drag reduction. This indicates that density modification plays an important role in the drag reduction phenomenon (Skudarnov *et al.* (2005)).

The reduction in density reduces the effective viscosity in the B.L. This has been attributed to a reduction in drag reduction. Also, the reduction of viscosity decreases

the turbulent momentum transfer leading to a drag reduction effect (Legner *et al.* (1984).

The density ratio also affects drag reduction as it relates to fluid flow. This is the ratio between the density of the fluid and the density of air. Studies show that using a lower air density at a high gas injection rate reduces the drag substantially; this can be seen in Figure 14 were C_f is skin coefficient with microbubbles whilst C_o is skin coefficient without microbubbles. Q is the flow rate of the microbubbles and U and A are the velocity of the water and the area of the flat plate respectively (Goolcharan, (2016)).

$$Density\ Ratio, DR = \frac{\rho_{water}}{\rho_{gas}}$$

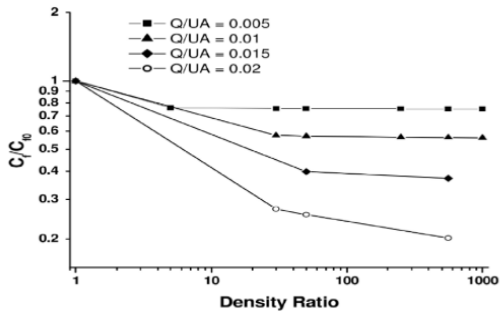

Figure 14: Graph Of Drag Reduction vs. Density Ratio (Goolcharan, 2016).

2.6 Compressibility

When considering minute bubbles, a straightforward one-fluid model would suffice to explain the dynamics of drag reduction, but this considers air as an incompressible phase. The equation of motion is the same as for a Newtonian fluid with renormalised properties.

In real life, the bubbles are constantly changing size and start to fluctuate. These fluctuations are due to:

- Distortion in shape due to forces on the bubbles
- Compressibility of the gas inside the bubble

It was demonstrated that the drag reduction by the bubbles is connected to the compressibility of the mixture.

Rigid bubbles enhance the drag reduction whilst bubbles that can vary in volume increase the efficacy of the drag reduction effect but not the drag reduction (Lo *et al.* (2006)).

A study on the inviscid stability of bubbly flow, bubble compressibility promotes the stability of the flow. Henceforth, the deformation and compressibility of the bubbly liquid is considered to attenuate the turbulence intensity and alter the turbulence structure (Kazuyasu *et al.* (2002)).

Van Den Berg *et al.* (2005) show in their work that drag reduction using MBDR is dependent on the effective flow compressibility and on the bubble deformability.

2.7 Numerical Simulations of Bubble Drag Reduction

When using numerical simulations bubbly dynamics are limited, this has led to studies that had some main parameters neglected. In Moriguchi *et al.* (2002) previous studies were reviewed were it was stated that the overall diameter did not affect drag reduction; it was assumed that the size of bubbles remains constant throughout the B.L. This means that bubble distribution, bubble coalescence, and break-up mechanism are neglected.

Ferrante *et al.* (2004) and Xu *et al.* (2002) used DNS to model a T.B.L. filled with rigid spherical bubbles with results indicating that drag reduction increases with the reduction of bubble size. Since the bubbles were modelled as rigid spherical bubbles the effect of compressibility was not included, which can alter results dramatically. On the other hand Lu *et al.* (2005) used deformable bubbles and discovered that drag reduction with MBDR using larger bubbles is related to the modification of energy-containing scales by larger bubbles.

Sindagi *et al.* (2019) uses a Volume of Fluid (VOF) approach to solve the Reynolds-averaged Navier-Stokes (RANS) equations with a Eulerian multiphase. The B.L. effect was designed using the all y+ wall treatment and realizable K-epsilon two-layer approach. The y+ value is a dimensionless parameter to characterise the near-wall distance of the first cell of a CFD mesh. The author managed to get good results when compared to experimental data with tests being done on a flat plate.

Kunz *et al.* (2007) modelled micro-bubble break-up and coalescence and validated the results against three sets of data: DNS modelling and two sets of experimental data. From this study, it was found that bubble coalescence and break-up played an important part in drag reduction.

Using a Large Eddy Simulation (LES) model would increase the accuracy, but it is not viable to use for such large and complicated simulations due to the time it would take. A solver called ReFRESCO has been used to model bubbly flow which solves unsteady multiphase incompressible flow (Terwisga, (2016)). Since the model takes the gas phase as incompressible the reliability of the simulations can be questioned. When air is being injected at a high hydrostatic force the air will be affected by the forces and compress to a smaller size as observed in a number of studies (Lo *et al.* (2006)) and (Kazuyasu *et al.* (2002)) and Van Den Berg *et al.* (2005)).

2.8 Scaling Law

A scaling law is an empirical relationship that describes the dependence of some physical or mathematical quantity on some other quantity, such that when one quantity is multiplied by a certain factor, the other quantity is multiplied by a power of that factor. In terms of engineering this can be used to scale results from a scale model to full size.

There currently exists no scaling law that can extrapolate results from a model and to full size and the equivalent injection rate. This is due to the complexity of numerous variables that affect ALS drag reduction, and the uncertainty of how the drag reduction is created, (Park *et al.* (2017)), (Qin *et al.* (2017)), (Hashim *et al.* (2015)) (Madavan *et al.* (1984)), and (Sanders *et al.* (2006)) .

The previous work of Elbing *et al.* (2013) and Elbing *et al.* (2008) on scaling for ALDR and BDR proved to give more insight on how the scaling law could be solved. The models for both ALDR and BDR collapsed due to varying flow speeds, surface conditions, surface tension as well as different design of ejectors.

Several data can be collected about BDR but as can be seen in Figure 15 but when comparing results with the injection ratio one can notice that the results do not follow one trend. What happens at 2 m/s can happen at 6 m/s and 11 m/s but not at 1 m/s, 10 m/s and 4 m/s. This does not come as a surprise given that the plate size, configuration, Re, injection method and flow speed are all different (Ceccio, 2010).

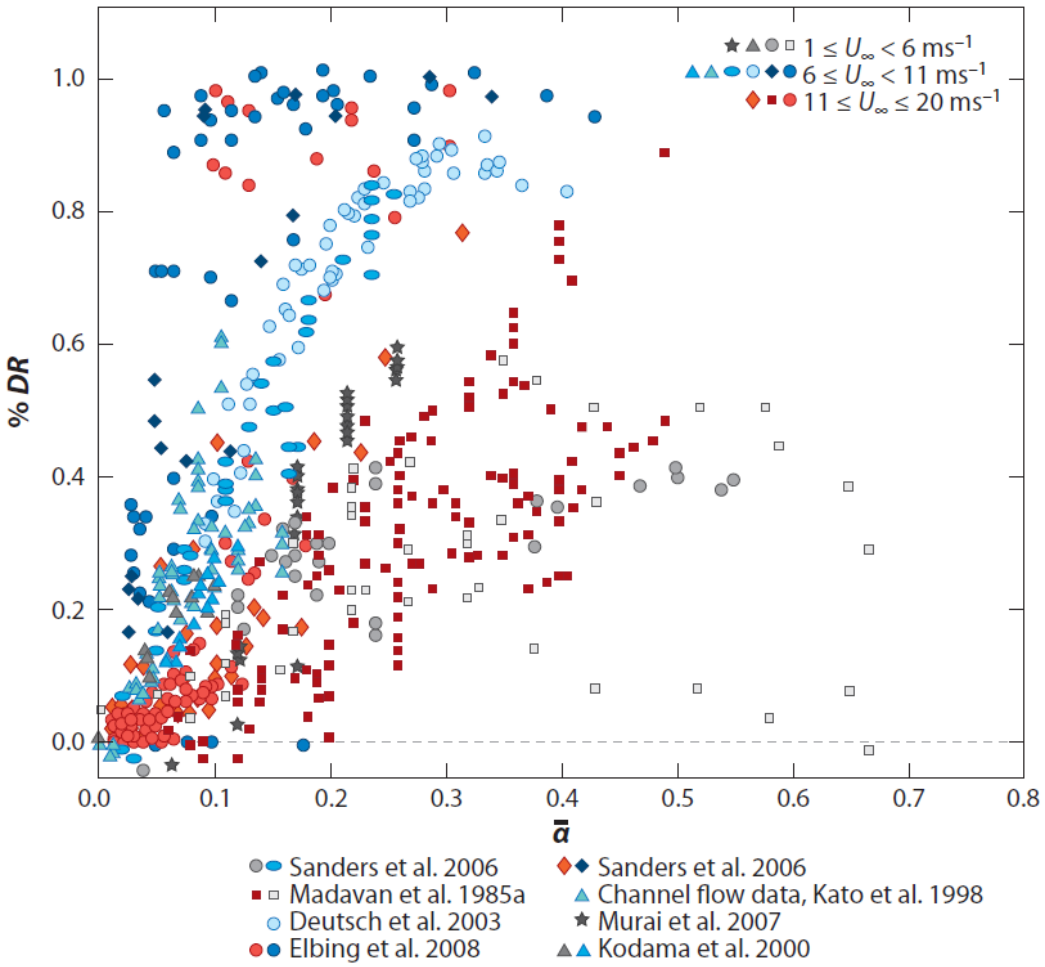

Figure 15: Plot with Different Experimental Data (Ceccio, 2010).

The D.R. is mainly due to the viscous force and as a result the Re is an important factor to keep in mind. The Fr is another factor that needs to be considered. When scaling up, satisfying one will still not be sufficient as the effect of the other factor cannot be estimated (Pavlov *et al.* (2020)).

Another factor to keep in mind is that whilst bubble size is thought to not play a large part in drag reduction their location within the turbulent B.L. does. When bubbles break

down into smaller bubbles the smaller bubbles will move away from the wall, thus reducing the volume fraction and going back to a fully turbulent flow. When the bubbles move away from the wall the length at which the drag reduction is totally dependent on how long the bubbles remain in the B.L. (Wendy *et al.* (2006)). Initial bubble seeding, density reduction, bubble-turbulence interactions as well as bubble-wall proximity are all important factors that are deemed important for drag reduction (Wendy *et al.* (2006)).Now, when injecting air into a small model versus a full-scale model the bubble size and bubble dynamics will change as well as the kinetic energy and wall shear which all play a part in the bubble splitting phenomenon and ejection from the B.L.

Investigating different experimental results shows that no method exists that normalises injection rate with drag reduction. This shows that the drag reduction effect is a function of more than air injection (Pavlov *et al.* (2020)).

It is generally understood that the deeper the draft the less efficient the drag reduction is, but no relationship has yet been developed. Therefore, it is recommended that model tests should be done to the largest capacity as possible and full-scale tests will give the most accurate result.

2.9 Case Studies

2.9.1 Till Deymann

A self-propelled barge was used for MBDR testing in the Netherlands. The Till Deymann as seen in Figure 16 has a length of 108.9 m, a breadth of 11.45 m, a depth of 5.15 m, and a 3.75 m loaded draft. Testing was done in calm water. This trial showed no difference in power needed to propel the vessel. A drag reduction of 2 % was achieved whilst the compressors needed 2.6 % power to work. Therefore, a net total -0.6 % was achieved. A drag reduction of only 2 % was thought to be due to the air bubbles not sticking to the hull.

Observations made were that the air injection was only at the bow. The research suggests that microbubble flow in an overpressure condition only works for a short distance (Foeth *et al.* (2009)).

Figure 16: Till Deymann Barge (Foeth et al. 2009)

2.9.2 MHI "Mals"

Mitsubishi Heavy Industries (MHI) invested many resources in Mitsubishi air lubrication systems (MALS) first installing their system on a vessel called Yamati in 2011. Whilst the Yamati uses air injection with a compressor they refer to air injection as "air blown off from the apertures on the bottom of the carrier turns into air bubbles by tearing off forces of the surrounding flow of sea water, running in the direction of the stern". This could mean that MHI could possibly have Kevin-Helmholtz instability to generate a steady bubble stream. This method could reduce the effect of overpressure leading to less power requirement. Testing on the Yamati gave net energy saving of around 8-12 %.

Later, MHI installed the system on a slender hull of the Ferry Naminoue. The vessel has a length of 145 m, a breadth of 24 m, and a fully loaded draft of 6.25 m. A 5 % net power reduction was achieved in seas of up to 3 m. It was also noted that the bubbles seemed to reduce the internal noise and vibration aiding in passenger comfort (Kawakita *et al.*(2015)).

Other companies have been very successful with MBDR with many reporting a reduction in noises in vibration as well as fouling growth. Data from 2018 shows that 23 vessels

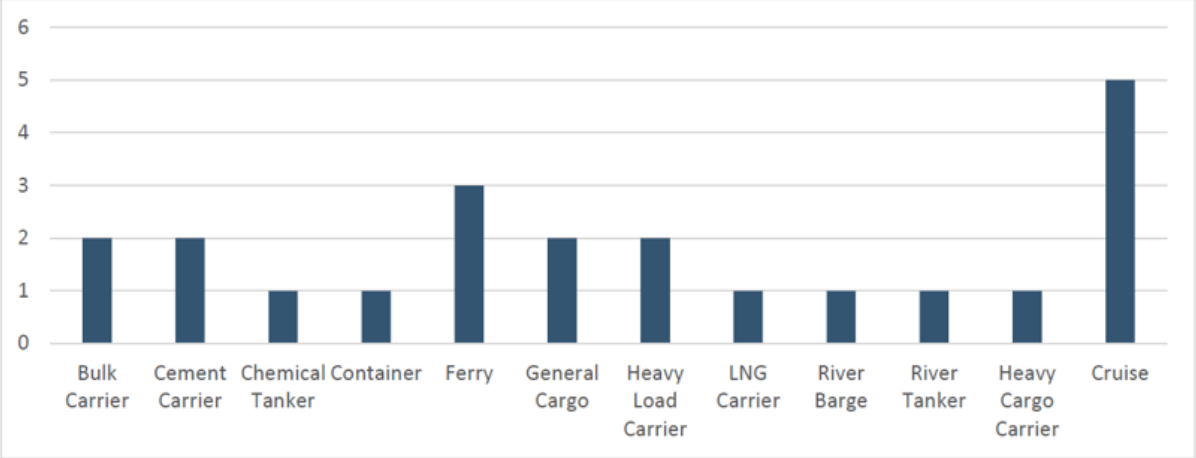

Figure 17:Vessels Using Air Layering (American Bureau of Shipping, 2019)

have installed air lubrication from a variety of different classifications as can be seen in Figure 17 (American Bureau of Shipping, 2019).

2.10 Limitations of Research

2.10.1 Uncertainty on How MDBR Works

From the literature available it can be seen that the drag reduction effect comes about by multiple mechanisms that work simultaneously, hence a proper mathematical scaling of BDR is yet to be achieved (Wendy *et al.* (2006)) and (Eggers *et al.* (2009)).

The physical properties of boundary layers that are filled with microbubbles and the resultant BDR have been investigated for years and are still only partially understood (Kunz *et al.* (2007)). The most widely accepted theory is that drag reduction is achieved due to the reduction of wetted surface area (Yao *et al.* (2011)). Keeping the void fraction constant will also give different results at different Re and pressure. The parameters will affect the bubble dynamics leading to either a drag reduction or drag increase (Jha *et al.* (2019)). Again, there is a lot of uncertainty as researchers have not underdone a ratio parametric testing were, a number of values are kept constant and changed to fully understand their behaviour and effect on ALS drag reduction.

There are several variables that are nonlinear and in fact there are several non-agreements between literature. Table 2 shows how all the variables affect drag

reduction in a bubbly flow, whilst Table 3 shows the mechanism-governing dimensionless parameters (Murai, 2014) and (Feng *et al.* (2020)).

Another factor to keep in mind is that when injecting a known bubble size, bubble dynamics have such large number of variables that once the bubble is injected its size will change immediately (Mohanarangam *et al.* (2009)) and (Tanaka *et al.* (2022)). Capturing the bubbles is also difficult in experimental work and highly expensive numerically therefore, it will be a case of injecting a known bubble size that will change immediately to an unknown bubble size.

Table 2: Table of Variables

Controlled Variables	
U	Liquid Flow Velocity
Q	Air Injection Rate
D_i	Distribution of Injectors
I_x	Injection Location
I_A	Injection Area
I_{AN}	Injection Angle
I_M	Injection Mode
d	Bubble Diameter
Boundary layer Characteristics	
δ	Boundary Layer Thickness
TKE	Turbulence Kinetic Energy
μ_t	Turbulent Viscosity
$\emptyset$	Air layer Thickness
Environmental Parameters	
P	Hydrostatic Pressure
g	Gravity
μ	Liquid Viscosity
ρ	Density Ratio
‰	Salinity
Ra	Surface Roughness of Plate

Table 3: Table of Dimensionless Parameters

Dimensionless Parameters	
Re	Reynolds Number
Fr	Froude Number
We	Weber Number
Ca	Capillary Number
Ma	Mach Number
$\propto$	Void Fraction

As can be seen in Figure 18, in some conditions of Re and α, a drag increase could happen (Jha *et al.* (2019)). Now this region will move for each case or application of MBDR. Therefore, better knowledge of how MBDR works and how it can be controlled is important.

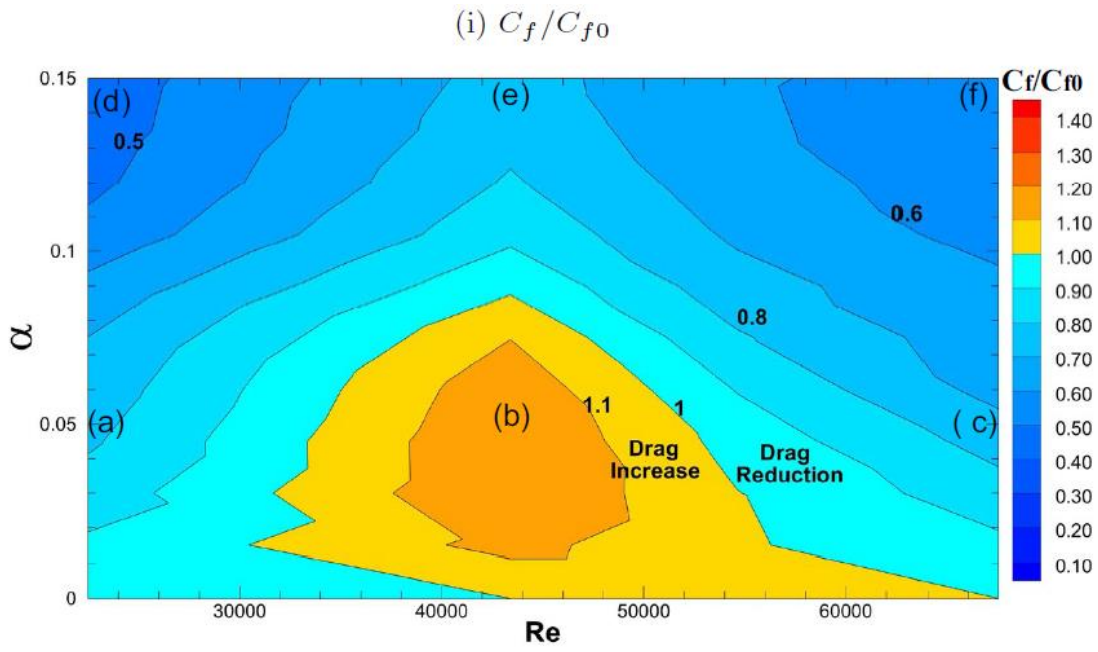

Figure 18: C_f/C_{f0} Comparison Across Different Re and Alpha (Jha et al. 2019)

2.10.2 Computational Uncertainties

Uncertainty in CFD refers to the lack of precision or accuracy in the results of CFD simulations. There are several sources of uncertainty in CFD, including the accuracy of the mathematical models used to describe the flow, the resolution of the computational mesh, and the quality of the boundary conditions used in the simulation. Additionally, uncertainty in the properties of the fluid being simulated such as viscosity and density, can also contribute to the overall uncertainty in the results. Reducing errors in CFD simulations is an active area of research, and techniques such as mesh refinement, sensitivity analysis, and uncertainty quantification are often used to improve the accuracy of CFD simulations.

When using a CFD program to design such mixtures and high Re, there exist some limitations which are inbuilt into the model. There is difficulty in modelling physical limitations such as the roughness of the hull. Adding to this, CFD is susceptible to the computational error that can propagate throughout the model and deviate from the original results, especially in models with two different flow materials and high velocities (Goolcharan, 2016).

(Brizzolara, 2014) concluded that the accuracy for CFD prediction is around 10 %. Mancini *et al.* (2017) found that resistance error can vary from between 4.5 and 9.5 % whilst Frisk *et al.* (2015) stated that resistance prediction is below 10 %.

Also, modelling a two-phase flow with bubbles is quite complex. The behaviour of large and small bubbles is totally different. The size will affect the buoyancy and lift force acting on them and their place within the B.L. With coalescence and break- up both bubble sizes will be present at the same time (Carrica *et al*. (1999)).

The current CFD models are also limited to what turbulence model can be used. Small scale testing can be done using DNS or LES but running a full-size model will be computational expensive and in some cases close to impossible with the current computer technology (Ferrante *et al.* (2004)). Therefore, this work will improve current ALS modelling methodology when using RANS.

Additionally, the lack of modelling compressibility when modelling ALS with two – phase flows in CFD research models have left a gap in research. Compressibility is a fundamental property of gas as it will change with hydrostatic depth. In normal instance researchers employ simplified models that assume air to be incompressible. However, disregarding compressibility has significant consequences, impacting mass flow rates and the injection rates within the entire system. When compressibility of air is not considered, mass flow rates fail to scale correctly, resulting in inaccurate ratios. Furthermore, when modelling compressibility, it accounts for the physics of air breaking up, compressing, and coalescence, increasing realism of the simulations. Once the addition of compressibility is factored in then a better representative of error due to injection of air can be understood.

2.10.3 Numerical Ventilation

This problem, although rarely discussed is one of the main sources of error when there is an acute entrance angle much like the air channels. Numerical Ventilation (NV) happens when the mesh is not fine enough such that the free surface interface is not captured adequately. When this happens air particles get caught in the first few cells of the B.L. nearest the wall and then get transported under the hull. If this occurs there will be a considerable effect on the outcome of the frictional resistance (Gray-Stephens *et al* . (2019)).

The shear stresses will also affect the resistance calculated as they will be computed to a lower value. Shear stress is calculated using velocity and viscosity. If a cell contains smearing of the two states due to NV the viscosity will be lower hence a wrong reading in friction (Gray-Stephens *et al* . (2019)).

2.11 Summary

This literature review covers the background literature on how air lubrication helps to reduce the drag of the ship. Different theories on how drag reduction can be achieved are explained in detail with the relevant experimental and numerical testing. Conflicting theories were also explained. Two case studies are also provided. It has been found that a reduction of 10 – 20 % in power with an almost similar reduction in pollution is possible (Terwisga, 2016). Emphasis was put on BDR since it is quite challenging to create an

active or passive air layer. The main mechanism of drag reduction due to bubbles and the problem of numerical ventilation was discussed in detail. The problems with numerical modelling were highlighted as well.

It can be clearly seen that in most work the air injection rate is changed with no respect to a ratio of air to water, this will alter the results and they cannot be used for any prediction of future data points.

The complexity of MBDR as well as the numerous parameters have made understanding as well as scaling MBDR exceedingly difficult. The effect of MBDR is undoubtedly incredibly positive from the drag reduction effect to the reduction in vibration and noises as well as fouling growth.

Whilst many companies have been successful in making it work to a great extent, more work is needed to fully understand this effect as well as to scale it up rationally. There is still a lack of commercial data and full-size testing is still lacking. Therefore, the closest one that can get to real-life testing is by using the largest-possible laboratory experimentation. This would lead to even more efficient systems to help tackle the problem of shipping emissions.

3 Methodology

3.1 Introduction

This chapter consists of two methodologies. The first methodology describes how the numerical modelling is set up and the testing done to ensure that the CFD model is robust enough to use for ALS modelling. This approach will also give a better understanding on how to properly model ALS systems using CFD. The second methodology tests different plate sizes to understand the relationship that exists between, draft, Fr, Re and scaling behaviour.

The second methodology test regime is divided into three parts. The first test is aimed to understand how depth effects drag reduction and for this, a same size plate is modelled at different depths with varying Fr and injection rates. During this test a study will also be done on different air injection rates to gain a better understanding to were, the optimal point is located at different depths. This will be the first time that such a test will be undertaken. The second test incorporates three different plate sizes at a constant depth with varying Fr numbers to investigate the effect of Re on a plate whilst. One of the reasons that this methodology was chosen is that there is very limited research done on the effect of Re and D.R (Wendy *et al.* (2006)). Lastly one of the plates was scaled up to full size so an understanding of the scaling effect on ALS, could be derived.

It is important to note that, to the authors best knowledge this is the first time that the effect of depth, compressibility, injection rate and injection rate compressibility and Re are modelled using CFD.

3.2 Numerical Modelling

All experimentation undertaken in this research was done using CFD. This was based on the "*The Specialist Committee on Energy Saving Methods"* (ITTC, 2021). In this work a survey was distributed amongst relevant organisations and the following suggestions were made:

- CFD analysis is believed to be more valuable than model scale ship tests
- The CFD analysis can be fully utilized to understand model-ship relationship

- Since the bubble size cannot be controlled in a similar way between model scale and full scale, it is difficult to predict the effect of air lubrication in full scale directly from model scale. So, the importance of feedback from full scale and/or a combination with two-phase flow CFD should be pointed out.

The program used was Siemens Star CCM+ 2021.1.1. Star-CCM+ is a commercial code developed by CD- Adapco. The Star-CCM+ software package offers several solutions for solving the Navier-Stokes equations. These include Reynolds Averaging Large Eddy Simulation (LES), Detached Eddy Simulation (DES), and inviscid potential flow. The work presented here utilizes the RANS approach. The simulations were run on Prospero which is a high performance computer ((ARI), 2021).

The use of CFD for fluid flow research is a method used by several fluid mechanics researchers with the number continually increasing. This method is not only cheaper to do but it offers a wider range of measurement readings and variations. The workflow for CFD can be seen in Figure 19.

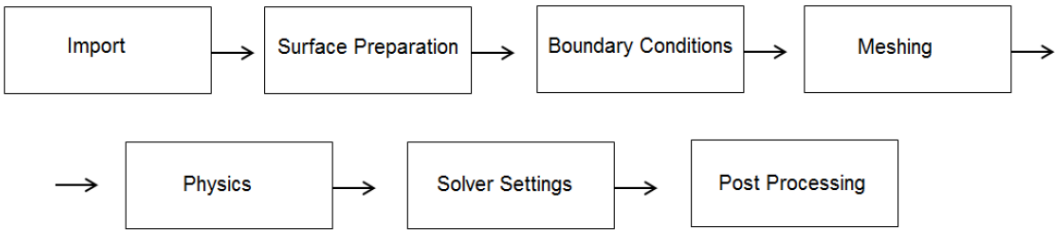

Figure 19: CFD Workflow

3.2.1 Numerical Set-up

A 3D, RANS with a volume of fluid (VOF) method was used to capture fluid motion (Faison, 2014) (Terwisga, 2016). Every CFD simulation is based on the governing equations of fluid dynamics which are continuity, energy and momentum. For an incompressible flow, continuity and momentum equations are sufficient but for compressible flows energy must be taken into account.

$$\rho\left(\frac{\partial}{\partial t}U + (U.\nabla)U + \nabla p - \delta\Delta U + \left(\eta + \frac{1}{3}\mu\right).U = G\right) \qquad (9)$$

$$\frac{\partial}{\partial t}\rho + \nabla.(\rho U) = 0 \tag{10}$$

$$\frac{\partial}{\partial t}E + \nabla.\big((E = p)U\big) = 0 \tag{11}$$

These three mathematical equations mean three things: that the energy is conserved, that the force equals the mass times acceleration, and that mass is conserved. Equations 9, 10 and 11 show the momentum, continuity and energy equation for Navier Stokes which has been modified for the effect of volume change in flow due to compressibility. Were U being velocity in all three directions since Newtons forces is applied in three dimensions, g is gravitational acceleration and P is pressure at any point in time t. The symbol ∇ represents the column vectors and the symbol Δ represents the Laplacian equations. The total internal energy of the fluid is modelled by E (Sochacki, 2013).

The VOF method is used in multiphase flow as a tracking and interface capturing method. VOF is a derivative of the surface integration of the RANS equation over a control volume. The motion of the two fluids is solved by computing a single set of momentum equations and calculating the volume fractions of each of the fluids throughout using additional transport equations. Using the VOF approach instead of Eulearian-Eulerian or Eulerian-Lagrangian will be able to track and analyse the flow better (Ebrahimi, 2012) and (Pineda-Pérez *et al.* (2018)) . Additionally, running a VOF model is less time intensive than a Eulearian-Eulerian or Eulerian-Lagrangian.

The VOF method simulates the air-liquid flow formed in an efficient manner. The addition of volume fraction of air and liquid will amount to one. From the volume

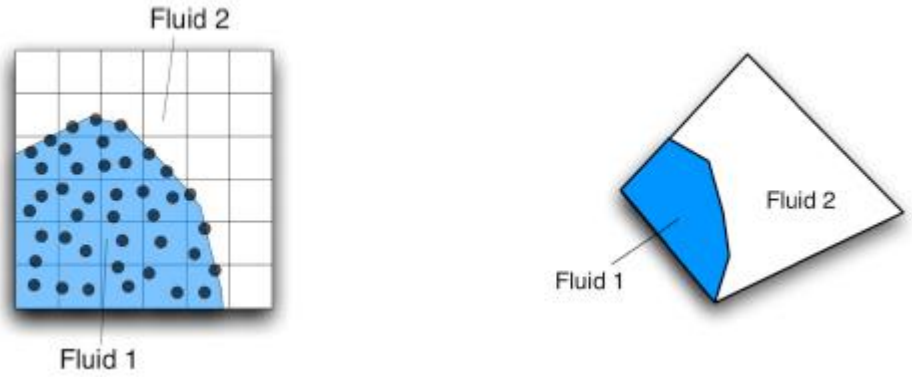

Figure 20: VOF Cell Discretization

fraction of air and water the parameters of the flow can be determined such as density, dynamic viscosity etc (Hao *et al.* (2019)). A method of solving this is to create a very fine mesh at the B.L. so as to obtain better discretization of the flow and the reduction of over estimation of air (Whelan, 2004). Once chosen a VOF model will introduce a new variable that defines the spatial distribution of both phases at any given time. This is called the volume fraction (Hao *et al.* 2019). VOF can be better understood using Figure 20 as the addition of unity as well as the importance of a fine mesh are displayed.

3.2.2 Boundary Study

In all CFD simulations, the selection of appropriate boundary conditions is vital for both the determination of an accurate solution and the prevention of unnecessary computational costs. To obtain a solution that is both accurate and uses the least amount of time a boundary parametric study was undertaken. From the work of Gray-Stephens *et al.* (2019) different types of boundary conditions could be used for the wall of the towing tank that resulted in an accurate solution but a faster simulation time.

The inlet and outlet of the boundary was set as velocity inlet and pressure outlet respectively. The following cases were modelling for the remaining walls. Figure 21 shows the set-up of the virtual towing tank. International Towing Tank Committee (ITTC) recommendations as seen in

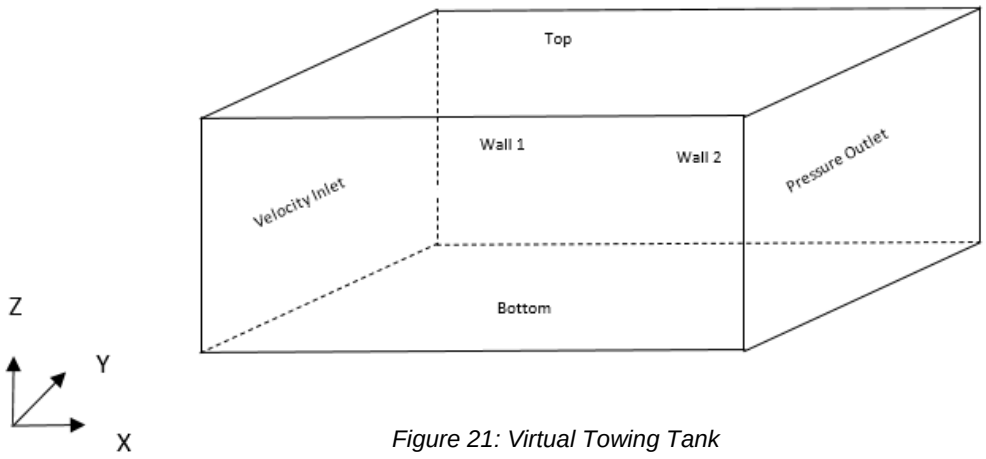

Figure 21: Virtual Towing Tank

Table 4 were considered for the size of the domain (ITTC, 2011).

Table 4: Table of Domain Size

	Domain Size	
	1st Point	*2nd Point*
X	$1 \times Lpp$	$Lpp + 1.4 \times Lpp$
Y	$1 \times Lpp$	$1 \times Lpp$
Z	$1 \times Lpp$	$1 \times Lpp$

The KCS model scale hull was used for this parametric study. The KCS hull was designed to provide data for both flow physics and CFD validation for a modern container ship with bulb bow and stern and it is (Simman, 2008) .

Table 5 shows the types of boundary conditions that were used with the equivalent number of cells, simulation time taken and accuracy (Angus Gray-Stephens *et al.*(2019)). The accuracy was calculated against the base line result of the KCS hull. Case number 3 was the baseline as given by Star CCM+.

Table 5: Table of Parametric Boundary Conditions Study

Boundary Condition Parametric Study				
Case No.	Boundary Conditions Used	Cell Count	Time Taken (s)	Error (%)
1	Wall for bottom and walls, velocity inlet for top	895,298	349,070	0.25
2	Symmetry plane used for top, bottom, and walls	852,000	316,270	0.61
3	Inlet for top and bottom, symmetry for walls	852,989	316,126	Baseline provided by Star CCM+
4	Slip wall used for bottom, walls, and velocity inlet for top	895,298	294,417	0.92
5	Velocity inlet or top, walls and bottom	852,000	296,844	0.47

Case 5 was 6.1 % faster whilst being accurate to be within less than 0.5 %, this also agreed with the literature (Angus Gray-Stephens *et al.*(2019)). The simulation was run until both the drag force result and the residuals had converged to an acceptable level based on ITTC (2011) recommendations. Therefore, case 5 was used for the remainder of this work.

3.2.3 Turbulence Modelling

There are four major classes of RANS turbulence models currently in Simcenter STAR-CCM+. This section presents broad guidelines as to the applicability of each of these.

Spalart-Allmaras models: is a simple on equation model that solves a modelled transport equation for the turbulent viscosity. The Spalart-Allmaras model is a good choice for applications in which the boundary layers are largely attached, and separation is mild if it occurs. Typical examples would be flow over a wing, fuselage, or other aerospace external-flow applications.

K-Epsilon models: is one of the most common turbulence models and it is a two-equation model, which means it includes two extra transport equations to represent the turbulent properties of the flow. The first transport variable is the turbulent kinetic energy (k) whilst the second transport variable is the turbulent dissipation (ε). It provides a good compromise between robustness, computational cost, and accuracy. This model is suited for industrial-type applications that contain complex recirculation, with or without heat transfer.

K-Omega models: is an improvement of the K-Epsilon mode, as the K- Epsilon model has some limitations in predicting turbulent flows that are near wall. It is a two transport equations solver that differ in the choice of the second transported turbulence variable. The performance differences are likely to be a result in a more accurate model especially when modelling near-wall flows and boundary layers. These models have seen most application in the aerospace industry. Therefore, they are recommended as an alternative to the Spalart-Allmaras models for similar types of applications.

Reynolds Stress Transport models (RST): are the most complex and computationally expensive models offered in Simcenter STAR-CCM+. They are recommended for

situations in which the turbulence is strongly anisotropic, such as the swirling flow in a cyclone separator.

RST models have the potential to predict complex flows more accurately than eddy viscosity models because the transport equations for the Reynolds Stresses naturally account for the effects of turbulence anisotropy, streamline curvature, swirl rotation and high strain rates.

A review of turbulence models of other studies, using CFD for planing hull and air injection simulations performance, was done. Planing hull research was investigated as with some stepped hulls, a passive air layer is created underneath the hull. It was found that many simulations use either a $k-\varepsilon$, or $k-\omega\ SST$ model (shear stress transport).

The SST model combines the k–ε and k–ω models with a blending function and creates the $k-\omega\ SST$ model. The low Reynolds number region in the vicinity of the wall is solved by the k–ω model and the far-away turbulent flow is simulated by the k–ε model. This approach provides much more feasible results in the near-wall region for the BDR problems since it eliminates errors from the empirical wall function since the $k-\varepsilon$ calculates the drag force based on assumption on the near wall equations (Ma *et al.* (2010)). Due to the instabilities from the bubbles in the viscous region this would result in inaccurate results. This can be noted in studies by Qin, (2017) and Chu *et al.* (2017) were they reported unrealistically high values of gas void fraction when using the $k-\varepsilon$ turbulence model.

Whilst both models have been shown to be comparable in terms of resistance prediction the $k-\omega\ SST$ is known to be superior at predicting separating flows and wake patterns. Work by Montazeri *et al.* (2019) noticed that SST model had the correct overall behaviour with respect to varying flow rates and air injection rates. Therefore , the $k-\omega\ SST$ was selected despite the fact that it is more computationally expensive (Gray-Stephens *et al.* (2019)), (Cucinotta *et al.* (2018)), (Banks *et al.* (2010)), Chu *et al.* ((2017)), (Mancini *et al.* (2018)), (Böhm *et al,* (2014)), (De Marco *et al.* (2017)), (Pineda-Pérez *et al.* (2018)) and (Avci *et al.*(2018)).

Equations 12 and 13 present the $k-\omega\ SST$ model were k is the turbulent kinetic energy, ω is the specific dissipation rate and μ_t is the turbulent viscosity. σ_k, σ_ω, C_1 , β and $\beta^*$are constants respectively.

$$\frac{\partial}{\partial t}(\rho k)+\frac{\partial}{\partial x_j}(\rho U_j k) = \mu_t\left(\frac{\partial U_i}{\partial x_j}+\frac{\partial U_j}{\partial x_i}\right)\frac{\partial U_i}{\partial x_j}-\beta^*\rho\omega k+\frac{\partial}{\partial x_j}\left(\left(\mu+\frac{\mu_t}{\sigma_k}\right)\frac{\partial k}{\partial x_j}\right) \quad (12)$$

$$\frac{\partial}{\partial t}(\rho\omega)+\frac{\partial}{\partial x_j}(\rho U_j \omega) = C_1\mu_t\frac{\omega}{k}\left(\frac{\partial U_i}{\partial x_j}+\frac{\partial U_j}{\partial x_i}\right)\frac{\partial U_i}{\partial x_j}-\beta\rho\omega^2+\frac{\partial}{\partial x_j}\left(\left(\mu+\frac{\mu_t}{\sigma_\omega}\right)\frac{\partial \omega}{\partial x_j}\right) \quad (13)$$

3.2.4 Compressibility

When modelling bubble dynamics compressibility was considered. This was done by modelling the gas model as an ideal gas. When considering compressible flow, the energy equation is added to the modelling as it is a fundamental equation to complete the system. Additionally, all collisions are elastic. When compressibility is not considered the air bubbles act as a solid sphere. This will remove any form of bubble dynamics when it comes to bubble break-up and coalescence. As mentioned in the previous chapter the density ratio also affects drag reduction. With deeper drafts the density of the air will increase, hence changing this factor as well.

Work done by Mohanarangam *et al.* (2009) also incorporates bubble dynamics which take into consideration break-up and coalesce have achieved promising results when compared to experimental testing.

Therefore, when considering the current lack knowledge of the effect of compressibility on DR, (Lo *et al.* (2006)), (Kazuyasu *et al.* (2002)) and (Van Den Berg *et al.* (2005)), choosing to include a compressibilty model would not only make the testing more realistic, but it will expand the knowledge in this area. It is also key to note that whilst the compressibility will add a more realistic approach to the simulation, it will also create another possible source of error that cannot be accounted for.

3.2.5 Wall Treatment

In fluids mechanics, the B.L. is described as a thin layer in which the velocity of the flow changes from zero to the free stream value. The thickness of this layer is defined as the normal distance from the wall till the velocity is 99 % of the free stream. This can be seen in Figure 22.

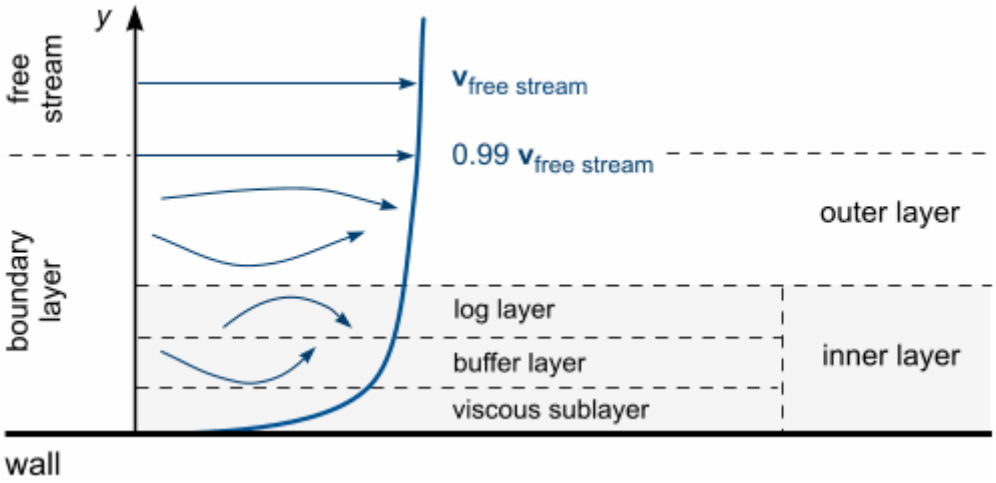

Figure 22: Boundary Layer (Larsson L et al. (2003))

As defined above the inner layer is divided into three sublayers: *Viscous Sublayer, Buffer layer and log layer*. From the literature provided previously, the air bubbles will mostly be in the viscous sublayer and buffer layer therefore, the proper discretization of the near wall viscous sublayer is needed because the microbubbles will change the wall shear stress in that region. Since bubbles are highly unpredictable the value of the wall shear stress cannot be estimated.

For a very discretized B.L. the minimum spacing of the prism layers from the wall needs to be calculated. This is based on the y+ value, which is a dimensionless parameter. The smaller the y+ the smaller the minimum spacing and the more discretized the B.L. will be. Therefore, a y+ of less than 1 was targeted as can be seen in Figure 23. This is called a low wall y+ treatment. The low wall y+ treatment measures the wall shear stress directly from the highly discretized viscous sub-layer whilst the high y+ wall treatment just goes off empirical results and statistics. This will create a well-defined B.L. which is needed for accurate readings (Weisheit *et al.* (2021)).

To calculate the initial cell size distance Equations 14 and 15 are used were Lpp is the length perpendicular and C_f is the coefficient of friction. This calculation is based on the International Towing Tank Committee recommended procedures (ITTC, 2011).

$$y = \frac{y^+}{Re\sqrt{\frac{C_f}{2}}} Lpp \tag{14}$$

$$C_f = \frac{0.075}{(\log_{10} Re\ - 2)^2} \tag{15}$$

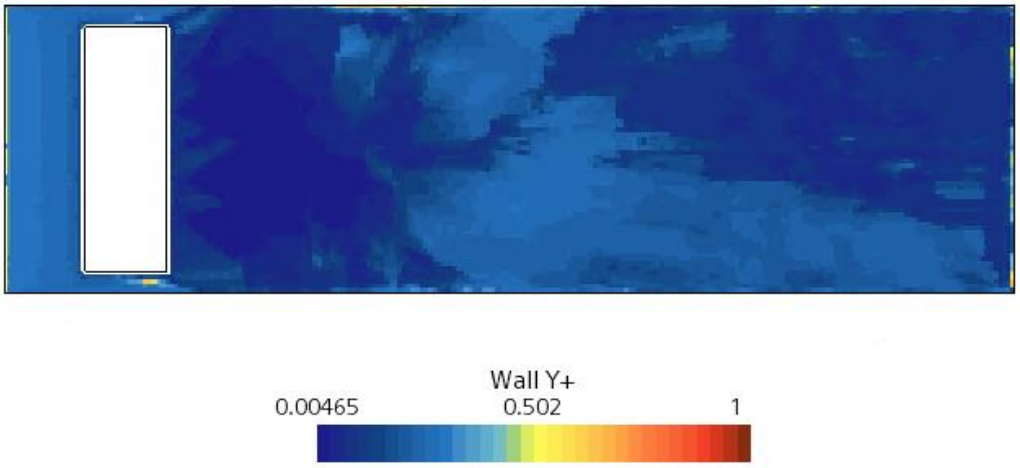

Figure 23: Low Wall Y+

3.2.6 Meshing

The accuracy and agreement of the numerical computation is strongly dependent on the type of meshing and its refinement. This in turn will affect the accuracy of the results. If a mesh is too fine, the accuracy of the simulation will be better, but it will be computationally heavy and take a lot of time to converge. On the other hand, if the mesh is too coarse, the simulation will run faster but it will give a result that will not be as accurate. Therefore, a grid refinement study was done.

Meshing was done using a trimmed hexahedral, prism layer and the automatic meshing function on Star-CCM+. The interface between air and water had a progressively refined mesh so it would not interfere with the plate and capture free surface movement. Based

on the very low wall y+ used, the near wall mesh was very fine as can be seen in the images. This was impervious for accurate bubble capture near the wall.

It can be seen in Figure 24 how the prism layers are modelled and how fine the mesh is at the wall. Figure 25 shows how the cell growth follows the ITTC regulations that every two cells grow into one. This is important to keep the mesh stable and uniform (ITTC, 2011).

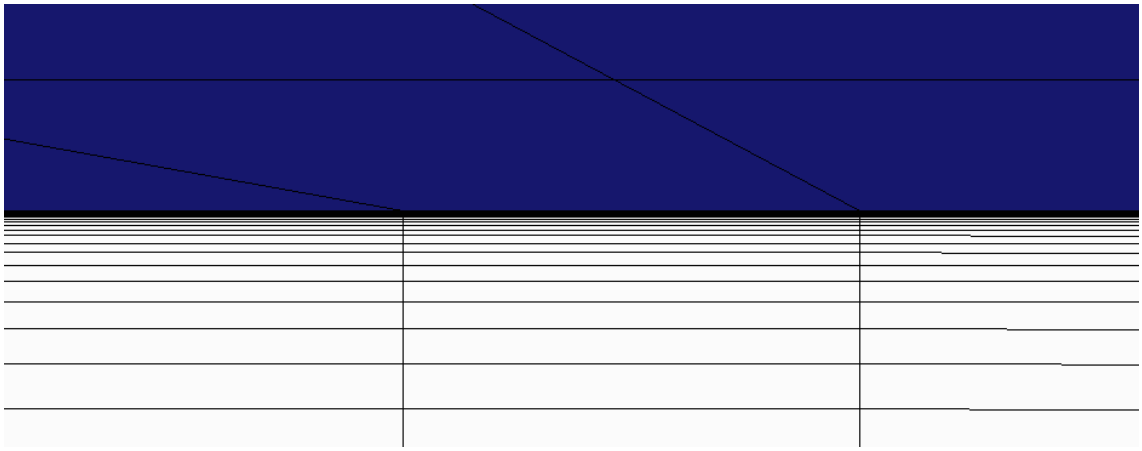

Figure 24: Prism Layer Growth at Wall

3.2.7 Prism Layer Mesher

This meshing technique is used to resolve the B.L. near the wall. The number of cells, number of prism layers, thickness of the cell and expansion rate are parameters that can be changed to create a smooth transition with the required y+. The Schlichting boundary thickness formula is used to determine the thickness of the turbulent B.L. as can be seen in Equation 16 were δ is the B.L. thickness and x is the length of the B.L (Siemens, 2019).

$$\delta = \frac{0.385\,x}{(Re_x)^2} \tag{16}$$

Equations 17 and 18 were used to determine the number of layers, n. These equations are based from the work of Siemens Star CCM + prism layer report(Siemens, 2019) The total thickness, t was calculated using Equation 16 , the initial wall spacing, a was calculated with Equation 15 and the stretch ratio r, was that of 1.3. The value of 1.3 was chosen as this gave the balance in terms of number of prism layers to simulation time.

The smaller the stretching ratio the higher the number of prism layers and the larger the simulation time

$$t = \frac{a(1 - r^n)}{(1 - r)} \tag{17}$$

$$n = log_r(1 - \frac{t(1 - r)}{a}) \tag{18}$$

Special attention was given for were the mesh went around the plate as this was the beginning of the boundary. The mesh was improved incrementally with two cells going into one based on (Siemens, 2019) recommendations, as can be seen in Figure 25.

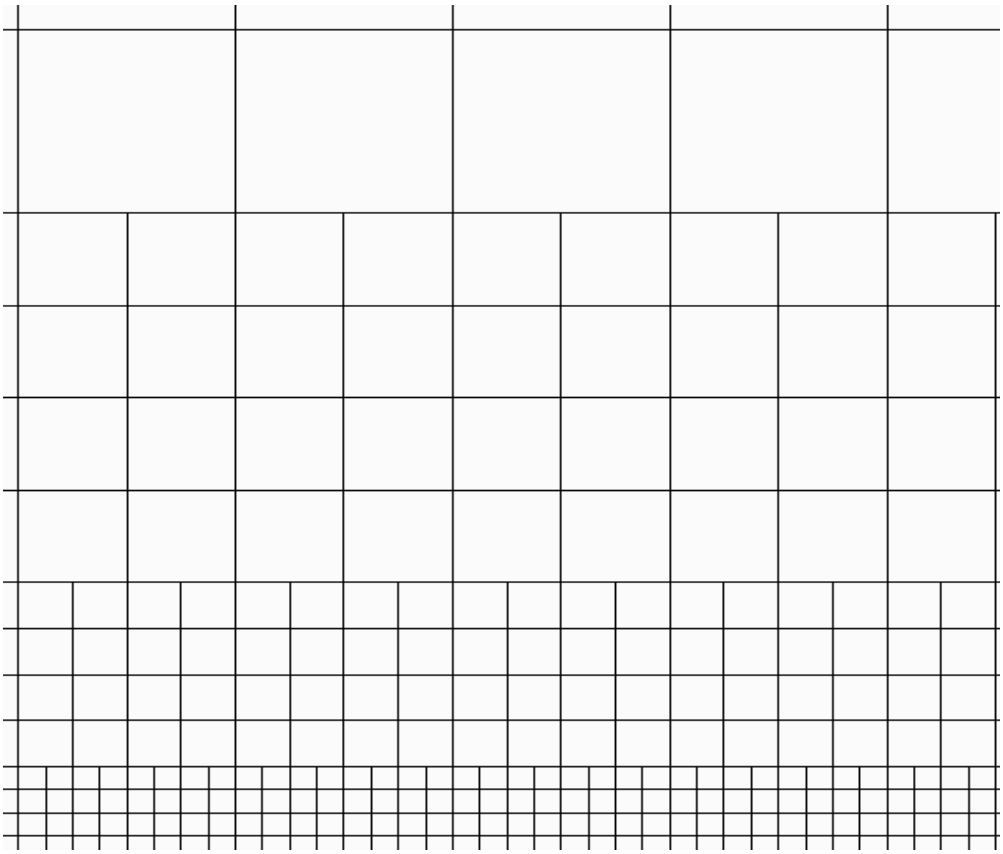

Figure 25: Cell Size Growth

3.2.7.1 Grid Refinement Study

Due to a strong interaction of the mean flow and turbulence, turbulence modelling needs a fine grid. To ensure this, a grid refinement study was done based on ITTC recommendations, increasing, and decreasing the base size by a multiple of $\sqrt{2}$ (ITTC, 2011).

The simulation was done on a flat plate that will be discussed in the next part of this thesis. Firstly, empirical equations were calculated using equation 1. CFD simulations were ran at three different base sizes. A coarse mesh with 1,049,784 cells, a medium mesh with 2,336,128 cells and a fine mesh with 4,477,126 cells. The results of these simulations can be seen in Figure 26, were the error from empirical equations is measured and a monotonic convergence is noted. A monotonic convergence, means that the solution is approaching a true solution(Stern *et al.* (1999). The medium mesh was chosen as the ideal base size for the meshing as it offered the best balance between simulation time and accuracy.

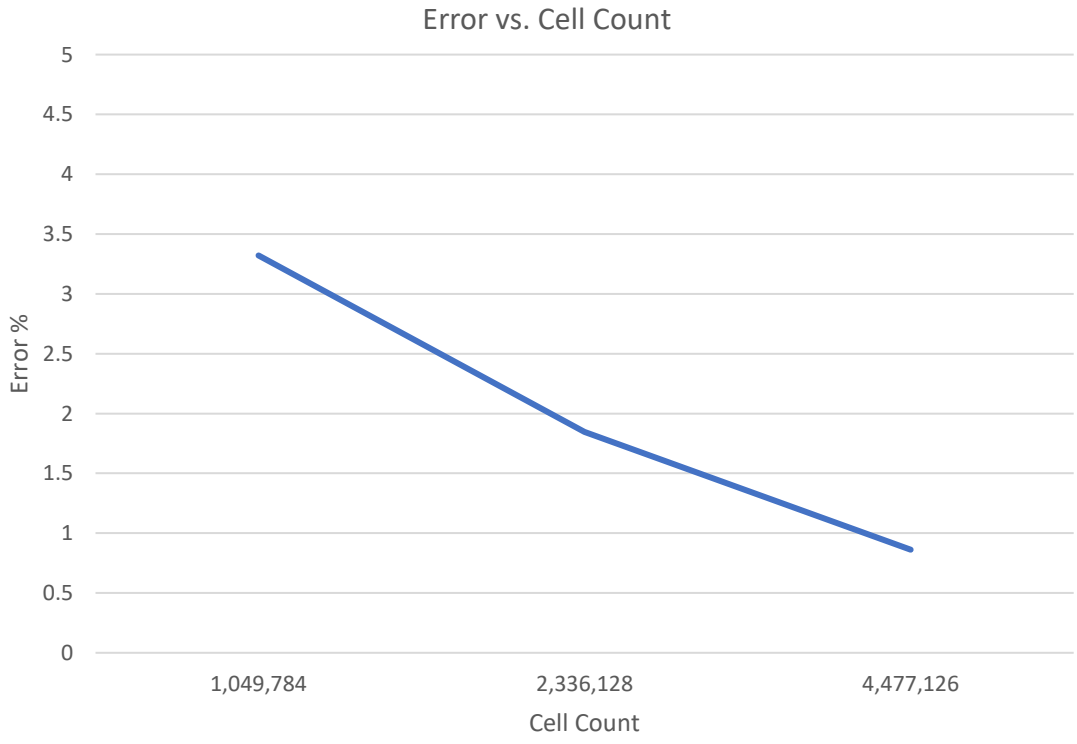

Figure 26: Grid Cell Refinement

3.2.7.1.1 Discretisation Uncertainty

Discretisation uncertainty occur from the representation of the governing flow equations and other physical models as algebraic expressions in a discrete domain of space and time. The discrete spatial domain is known as the grid or mesh. Discretisation uncertainty is of major concern because it is dependent on the quality of the grid. Work done by several researchers show that discretisation uncertainty is the largest source of uncertainty in CFD (Gel et al. (2013) and (Syamlal et al. (2017)). The level of discretization uncertainty is dependent on grid quality and any value under 5 per cent is the accepted level in CFD. (Roache, 1997),(Calavia, 2016) and (H K Versteeg, 2007)

The discretisation error is calculated as seen below:

$$\varepsilon = \left[1 - \frac{Coarse\ Mesh}{Exact\ Solution}\right], \left[1 - \frac{Medium\ Mesh}{Exact\ Solution}\right], \left[1 - \frac{Fine\ Mesh}{Exact\ Solution}\right]$$

This resulted in the following as can be seen below in Table 6.

Table 6: Table of Discretisation Error

Discretisation Error	
Coarse	4.37
Medium	2.91
Fine	1.94

For all the mesh types, the discretisation error was at an acceptable level, but since the medium mesh was chosen the error level was well within the acceptable level.

3.2.8 Time Step

For the time step on the flat plate the initial equation given by ITTC (2011) was that of:

$$\Delta t = 0.005 \sim 0.01\ L/U$$

ITTC (2011) recommends that for turbulent flow the following should be used:

$$\Delta t = 0.001 \sim 0.0025\ L/U$$

Were L being length and U is the flow velocity. This is recommended for models were the turbulence is high. Also, to avoid NV it is advised to make the time step as small as

feasibly possible (ITTC, 2011). Therefore, to ensure that NV was avoided the smallest value of 0.001 was used.

3.3 Scaling Plate Methodology

3.3.1 Ideology

To start understanding the scaling effect of air lubrication and its effect on drag reduction, several tests were planned. It must be understood that when scaling up from a scale model both the hydrostatic pressure and the Re number change and these are known to hinder the drag reduction effect, but a direct relationship does not exist (Sanders *et al.* (2006)), (Mäkiharju *et al.* (2013)) and (Sanada *et al.* (2009)). Therefore, the scaling study must be divided into two parts:

i) Effect due to hydrostatic pressure.
ii) Effect due to Re scaling.

The effect of hydrostatic pressure would be tested, as seen in Figure 27. The Re effect would be tested as in Figure 28. Once the results are obtained, a third testing campaign must be undertaken were the plate is both scaled with depth and Re at the same time to understand how and when these two effects are combined how the changes as can be seen in Figure 30. Figure 29 is the plate as designed with the air injection outlet in grey.

The plate with a size of 5 m length and 1.42 m width was designed with a slot in the bottom of the plate to inject air. The size of the initial plate was calculated based on what typical plate sizes could be tested in towing tanks and cavitation tunnels. The air was injected using the Mass Flow Inlet boundary condition. When using the mass flow inlet boundary condition, a specified mass flows across the boundary, and the static pressure at the boundary is extrapolated from the domain's interior. The plate and slot were designed from ideas from industry (SilverStream, 2019) and (MHI, 2012)

For this testing, different injection rates of α will be used. The different injection rates will then be investigated and scaled up to the different plate sizes.

Five Fr were chosen and can be seen in Table 7. The range of Fr chosen was to incorporate ships speeds that are thought of as medium and fast, as most studies are done at lower speeds. This way a better understanding of ALS could be gathered.

Table 7: Table of Froude Numbers

Fr
0.28
0.31
0.35
0.38
0.42

Figure 27: Same Plate Size Testing

Figure 28: Increasing Re Testing

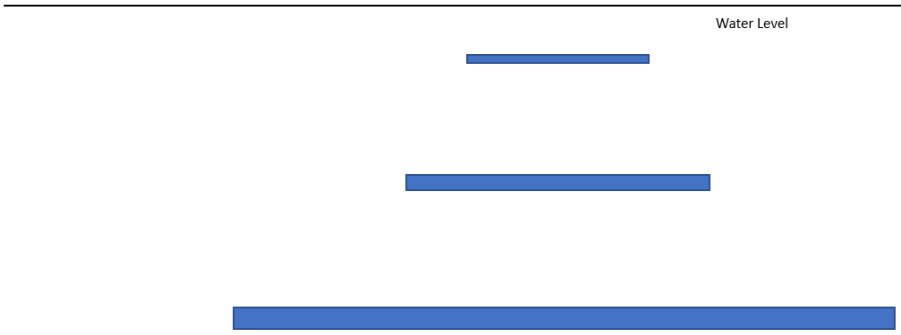

Figure 30: Scaling Up Testing

Figure 29: Small Plate with Air Outlet in Grey

3.3.2 Small Plate Set- Up

The plate sizes were based on sizes that would replicate both real life scaling in cavitation tunnels HSVA (1990) and a size that would make numerical simulations run without taking too long and can be seen in Table 8.

Table 8: Small Plate Details

Small	
Length (m)	*5*
Width (m)	*1.42*
Area (m^2)	*7.1*
Injector Length (m)	*0.401*
Injector Width (m)	*1.204*
Injector Area (m^2)	*0.482*

Five depths at intervals of 1.5 m were used for the simulation as can be seen in Table 9. The 6.5 m depth was chosen as half of the global fleet has a draught of 6 m or less (Oeffner *et al.* (2020)).

Table 9: Table of Depths

Depth (m)
0.5
2
3.5
5
6.5

3.3.3 Re Plate Set- Up

Three plate sizes were chosen with increasing Re to understand how an increasingly turbulent Re effects the drag reduction as can be seen in Table 10. The Re testing was done at 0.5 m depth for two reasons. The first was to reduce the towing tank size and simulation time and the second one was to remove the effect of hydrostatic pressure as much as possible.

The Re sizes were chosen on the bases that in practical applications of ALS the Re is in the order of Re $x10^8$ and Re $x10^9$. Also, work is done up to Re $x10^8$ it is to the best of the authors knowledge that no large-scale numerical testing at Re $x10^9$ has been done.

Also, in previous tests done in literature the ejector size and shape are changed affecting the end results (Elbing *et al.* (2013)). Therefore, the ejector size and shape were kept constant as in Table 8 . The width of the plate was also kept constant as the injection ratio alpha is dependent on the width as can be seen in Equation 26.

To the authors best knowledge this will be the first work that investigated the effect of Re and modelling compressibility at the same time. Therefore, this work will give a better understanding of what behaviours and ALS system might deliver at high RE, those equal to full size vessels. Additionally, it must be kept in mind that when scaling models for normal resistance results, from towing tank to full scale a Froude scaling is

undertaken. Therefore, it is important to understand what effect Reynolds scaling has on the total D.R. effect.

Table 10: Table for Re Testing

Fr	Plate Length (m)	Re
0.42	7	$2.74x10^7$
0.42	32	$2.68x10^8$
0.42	88	$1.22x10^9$

3.3.4 Scaling Plates Set-Up

The final plate set-up was that of scaling up the plate from small to full size as can be seen in Table 11. The initial depth for the small plate is 0.5 m whilst for the large plate the depth is 6.5 m, therefore the scaling ratio is 13, whilst the scaling ratio for the medium plate is 1.85 as can be seen

Table 12. In previous work, the scaling up of both the MFR and the injection area has not been done previously (Ceccio, 2010).

Table 11: Table of Plate Sizes

Plate Sizes			
	Small	Medium	Large
Length (m)	*5*	*35*	*65*
Width (m)	*1.42*	*9.94*	*18.46*
Area (m^2)	*7.10*	*347.90*	*1,199.9*
Injector Length (m)	*0.40*	*2.81*	*5.21*
Injector Width (m)	*1.20*	*8.43*	*15.65*
Injector Area (m^2)	*0.48*	*23.66*	*85.59*

Table 12: Scaling Depths and Ratio

	Scaling Depths and Ratio		
	Small	Medium	Large
Depth (m)	*0.5*	*3.5*	*6.5*
Scaling Ratio (λ)	*13*	*1.85*	

3.3.5 Injection Rates

Sayyaadi *et al.* (2013) and Latorre (1997)'s research shows that an optimal air injection co-efficient alpha α of between 0.4 and 0.6 would result in the largest drag reduction. The injection rate Alpha was calculated using Equations 19 -26.

$$\alpha = \frac{Q_a}{Q_w} \tag{19}$$

- Q_a is the injected air flow rate.
- Q_w is the water flow rate within the B.L.

The water flow rate in the B.L. can be calculated using the turbulent boundary theory (H.Schlichting, 1968)

$$Q_w = U_f \times (\delta - \delta^*) \times b \tag{20}$$

were b is the width of the plate, Uf is the flow velocity out of the B.L. and U is the fluid velocity in the B.L., δ is the B.L. thickness, y is the distance from the wall and δ^* is displacement thickness calculated as below:

$$\delta^* = \int_0^{\delta} \left(1 - \frac{U}{U_f}\right) dy \tag{21}$$

$$\delta^* = 0.125 \times \delta \tag{22}$$

A seventh power velocity distribution is assumed for the velocity distribution across the B.L.

$$\frac{U}{U_f} = \left(\frac{y}{\delta}\right)^{\frac{1}{7}} \tag{23}$$

The thickness of the turbulent B.L. thickness is calculated using:

$$\delta = \frac{0.3 \times x}{RE_x^{0.2}} \tag{24}$$

Using Equations 22 and 23 to solve Equation 21 the water flow rate can be calculated as:

$$Q_w = 0.3238 \times U_f \times b \times x \times Re_x^{-0.2} \tag{25}$$

Simplifying the equation gives us:

$$Q_w = 0.293 \times L^{0.8} \times V^{0.8} \times \vartheta^{0.2} \times w \tag{26}$$

were, L is the length, V is the velocity of water, w is the width, and ϑ is the kinematic viscosity of the fluid. Therefore, alpha is dependent on the plate's length, width and the velocity of water flowing around the plate. Once Q_w was calculated, Q_a can than be calculated depending on the alpha choosen.

The alpha values of 0.1, 0.4, 0.5, 0.6 and 0.9 were chosen for the same size plate. The extremities were chosen to confirm that the physics of the model and bubble dynamics were modelled accurately as it is expected that these two results will not be optimal. For the Re and scaling up testing the alpha values of 0.4, 0.5 and 0.6 were chosen, this decision was done based on the amount of computational time needed.

3.4 Corrected Mass Flow Rate

Since compressibility is considered, the density of air will change with hydrostatic pressure. This change in density as seen in Table 13 will affect the MFR. Since the MFR is dependent on density as can be seen in Equation 27 the mass flow rate was calculated with the relevant density for every depth. This ensured that the injection rates remained constant even when changing the position of the plate.

Table 13: Table of Changing Density with Depth

Depth (m)	Density (kg/m^3)
0.5	*1.192*
2	*1.372*
3.5	*1.562*
5	*1.725*
6.5	*1.915*

$$MFR = A \times \rho \times V \tag{27}$$

3.5 Conclusion

In this chapter the methodology of this research was described. The numerical methodology was described and all the relevant ITTC regulations were followed. Boundary wall condition testing was done to find the fastest and most economical CFD set-up. The general CFD set-up was explained in terms of ITTC regulations, the addition of compressibility and the type of meshing used. In the second part of this chapter the scaling methodology was described. This involved the plate sizes used for the three types of testing which are: i) same plate size different depth testing, and ii) Re testing and scaling up testing. The injection rates calculation was described as well as the correction for the mass flow rate to overcome the effect of compressibility.

4 Results and Discussion

4.1 Introduction

This chapter will go through the results for all three campaigns of testing. First the testing started with a plate of the same size tested at different depths. This was done to study the effect of hydrostatic pressure on the drag reduction effect. The second testing was three consecutively larger plates with a respective higher Re number, to study the effect of Re on drag reduction. The third set of tests uses three plates of different sizes and at different drafts This will be used to understand what happens when a plate is scaled up both in hydrostatic pressure and in Re.

4.2 Initial Flat Plate No Air Comparison

The first step was to set the baseline of the flat plate without any air. This was compared to empirical equations, to verify the accuracy of the CFD model. The coefficient of friction was calculated using the empirical Equation 28 which is the equation for the co-efficient of friction over a turbulent flat plate (Cimbala, 2014)

$$C_f = \frac{0.027}{Re^{\frac{1}{7}}} \tag{28}$$

The coefficient of friction was then used to calculate the drag force using Equation 29.

$$D = C_f \times 0.5 \times \rho \times U^2 \times W.S.A \tag{29}$$

Where C_f is the co-efficient of friction, $W.S.A$ is the wetted surface area, ρ is the density of the fluid, U is the velocity of the fluid.

Table 14 shows the calculated data compared to the CFD data. It can be noted in Table 14, Figure 31, and Figure 32 that the error is minimal. Figure 32 displays that the error is constant all throughout various Fr numbers. It can be noted that the error is low for CFD, but this is expected as the simulation is not very complex with just a single phase of water passing over the plate. This testing shows that the CFD set-up is robust and very accurate.

Table 14: Table Comparing Calculated Drag vs. CFD Drag

Fr	Calculated Drag (N)	CFD (N)	Error (%)
0.28	*35.20*	*34.80*	*1.14*
0.31	*44.14*	*43.70*	*1.00*
0.35	*54*	*53.18*	*1.52*
0.38	*64.77*	*63.86*	*1.40*
0.42	*76.43*	*75.53*	*1.18*

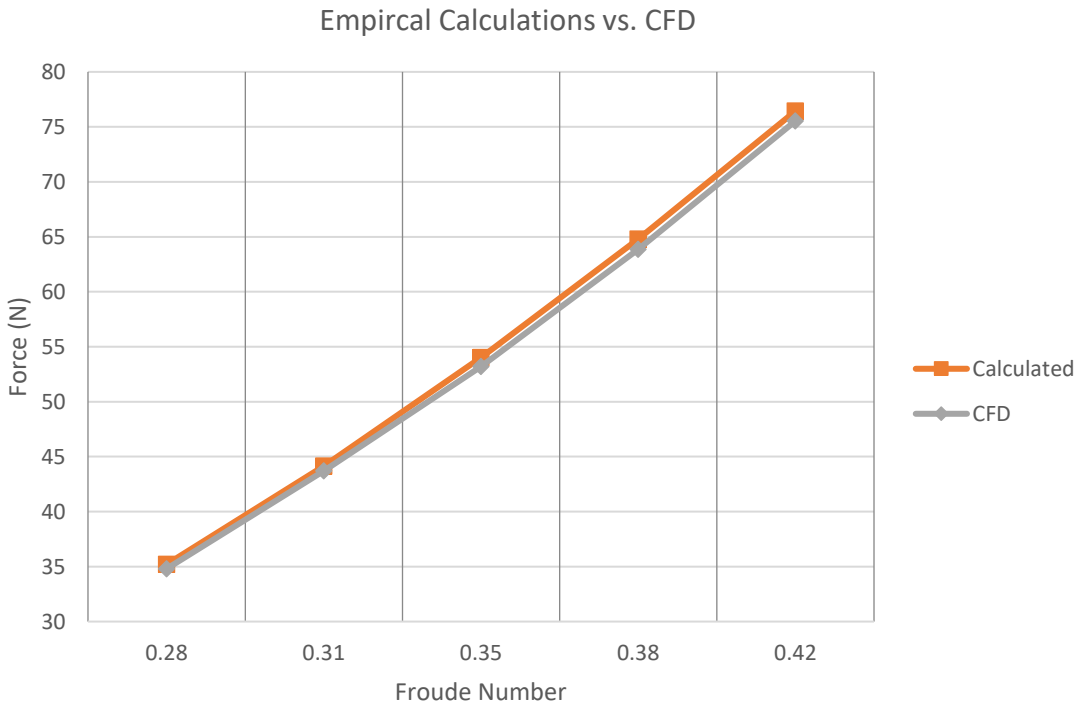

Figure 31:Graph of Empirical Calculation vs. CFD

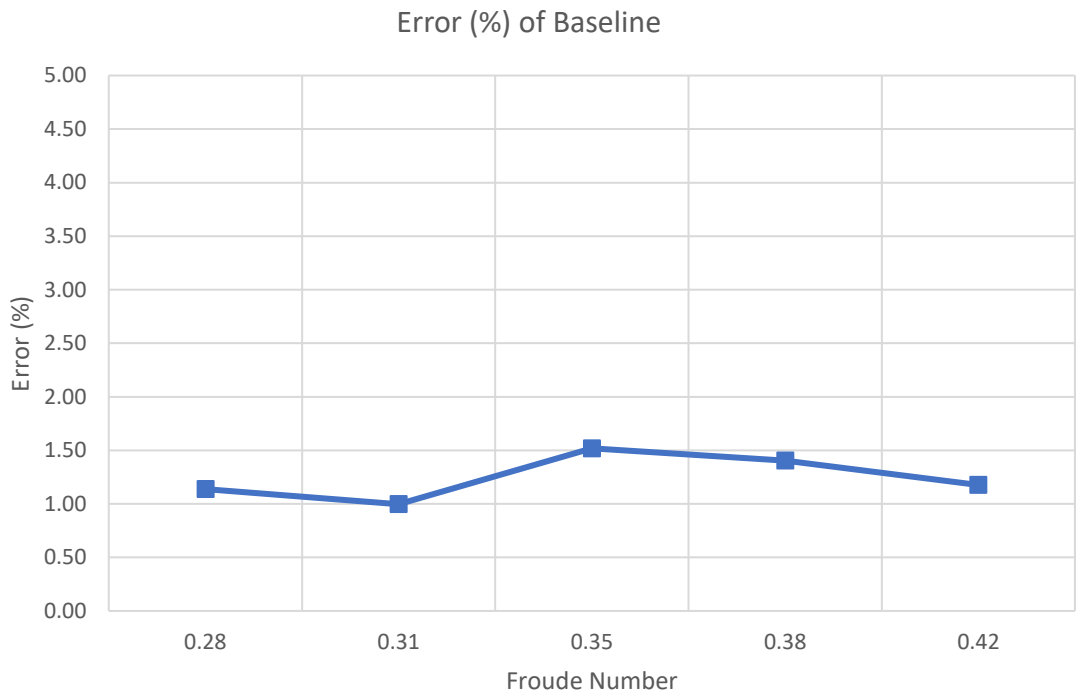

Figure 32: Graph of Error of Base Line Results

4.3 Statistical Analysis

A statistical analysis of the data that was obtained via CFD was undergone to gain a better understanding of the behaviour of ALS with respect to different parameters. The two statistical analyses done where the correlation coefficient r and the coefficient of determination R-squared. These two factors were chosen as they give a clear understanding of relationships and trends between data.

4.3.1 Correlation Coefficient r

The correlation coefficient is a statistical measure of the strength of the linear relationship between two variables. The values of this correlation can range from -1 to 1. A coefficient of -1 describes an inverse correlation were one value is rising and the other is decreasing, whilst a coefficient of 1 shows a positive correlation with both values rising. If the coefficient is 0 then there is no linear relationship. This is sometimes called the Pearson correlation coefficient, and it is used to determine patterns in data. Table 15 shows the strength of the coefficient.

Table 15: Pearson Correlation Value

Pearson Correlation Value	Strength
0-0.1	No Correlation
0.1-0.3	Little Correlation
0.3-0.5	Medium Correlation
0.5-0.7	High Correlation
0.7-1	Very High Correlation

4.3.2 Coefficient of Determination R- Squared

R- squared is a statistical measure that represents the percentage of the variance for a dependent variable that is explained by an independent variable or variables in a regression model. It ranges from 0 to 1, with 0 meaning there is no dependence on the variable and 1 is perfect fit. It is a tool used for prediction of further points of data and it is used to identify the strength of the model. It indicates how much variation of a dependent variable is explained by the independent variables.

4.4 Same Plate Scaling

In this section, the data from the testing of injection ratios α 0.1, 0.4, 0.5, 0.6 and 0.9 will be compared and evaluated. The five different injection ratios were chosen based on the work of Sayyaadi and Nematollahi (2013) and Latorre (1997), this would also act as a validation for the CFD model if there is agreement.

4.4.1 Mass Flow Rates Used

In Figure 33 the MFR of α 0.9 is plotted against the depths of testing. The effect of compressibility of air can be noticed. The deeper the plate, the greater the density of air hence the greater the MFR, even though the ratio of injection remains the same.

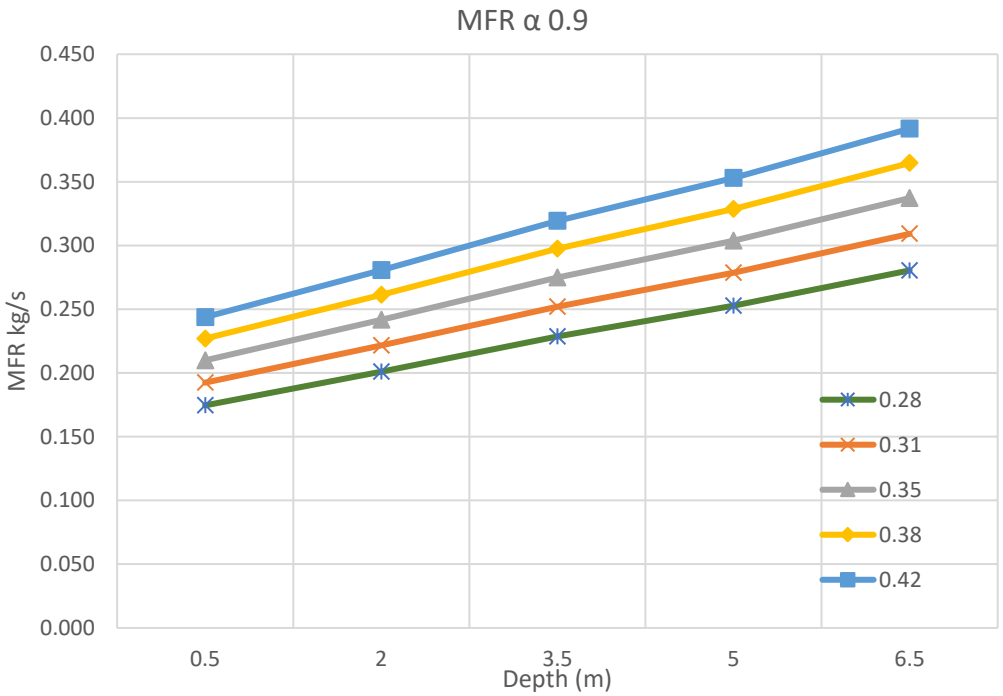

Figure 33: MFR of α 0.9

Table 53 - Table 57 in Appendix B show the total mass flow rates used for the testing.

4.4.2 Drag Reduction Results

Figure 34 depicts the drag reduction effects against different depths for all the results for individual mixing ratios of alpha across all five Froude's number from 0.28 to 0.42. It can be immediately noticed that the deeper the plate was positioned, the efficiency of the ALS reduced. Therefore, an initial understanding of hydrostatic pressure could be observed. For all the mixing ratios except 0.1 the highest drag reduction achieved was by the highest Fr. For most results, the Fr results stack on the top of each other neatly with the highest Fr resulting in the largest D.R. While research suggests that ALS is more efficient at lower speed, these results show otherwise, in such experiments the air injection rate is kept constant whilst changing the velocity, altering the injection ratio. Work done by Zhao *et al.* (2022) also resulted in the same findings with the highest Fr having the best D.R. but in this case the mixing ratio was also not kept constant.

When the plate is at a larger hydrostatic pressure the bubbles will become smaller and smaller and will eject faster outside of the T.B.L, therefore with a higher velocity and

more air in the T.B.L. , more air will remain in the T.B.L. It is hypothesised that when air is being sucked out of the T.B.L. , a swirling motion and vortices are created that increase the turbulence hence increasing the D.R. This was also observed by Jha *et al.* (2019).

Table 16 and Table 17 are the correlation and R-squared value of comparing the drag reduction at a Fr for all depths. It can be noticed that both values are very close to one for all the data points. This signifies that there exists a linear relationship between the drag reduction effect and the hydrostatic pressure at those Fr and mixing ratios. The relation is an inverse one due to the negative value of the correlation number. This means that as the depth or hydrostatic pressure goes up the drag reduction effect decreases. With such a high value of the R-squared value the data point can be used to predict the drag reduction at more depths for individual Fr and different injection rates.

Looking at Table 18 one can notice that the average peak drag reduction was achieved at 0.4-0.6 alpha and the higher injection rate of 0.9 did not create the best drag reduction effect. This can be seen in both the mean and the highest D.R. recorded per alpha. This is in line with what literature has provided. The median is also very close to the mean, indicating that the data is normally distributed. It is interesting to note that the negative drag reduction seems to have a stop at forty-five % across all tests. It is thought that for a high injection ratio the bubbles will exist the boundary layer immediately and leave a smaller ratio of air in the B.L., the exiting of the bubbles will also increase the turbulence (Gao *et al.* (2023)).

The optimal injection rate behaviour is the same as the work of Sayyaadi *et al.* (2013) and Latorre (1997) were they state that the optimal injection rate lies between 0.4 and 0.6 as can be seen in Figure 35. Figure 35 can also be compared with Figure 36 . This was the first point in validating the CFD model and that it could replicate the physical behaviour that was monitored in experimental data. Also, these results show that the optimal injection rate is valid for different hydrostatic depths, whilst in literature testing was done at one hydrostatic point. This means that this range can be applied to different types of ships, with varying operating conditions.

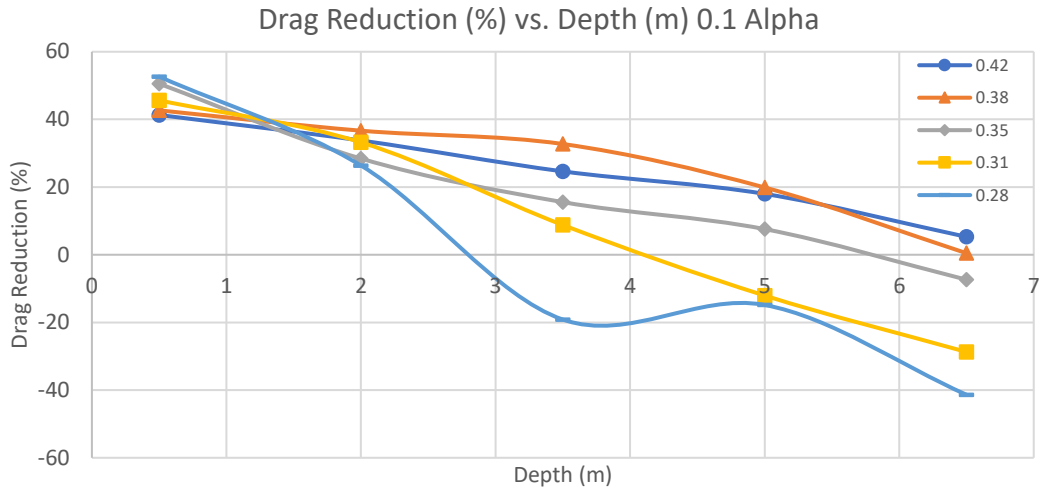
Drag Reduction (%) vs. Depth (m) 0.1 Alpha
Drag Reduction (%)
Depth (m)
60
40
20
0
-20
-40
-60
0
1
2
3
4
5
6
7
0.42
0.38
0.35
0.31
0.28

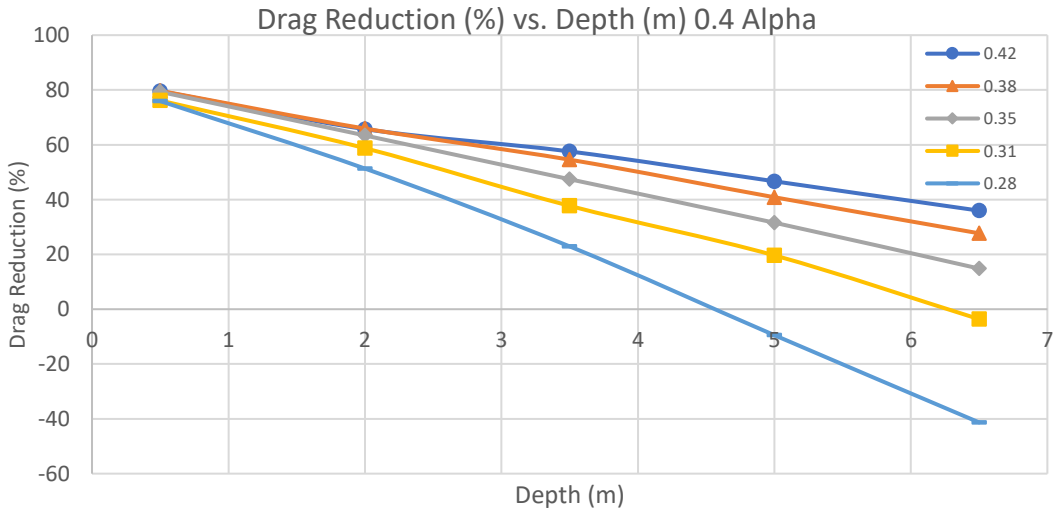
Drag Reduction (%) vs. Depth (m) 0.4 Alpha
Drag Reduction (%)
Depth (m)
100
80
60
40
20
0
-20
-40
-60
0
1
2
3
4
5
6
7
0.42
0.38
0.35
0.31
0.28

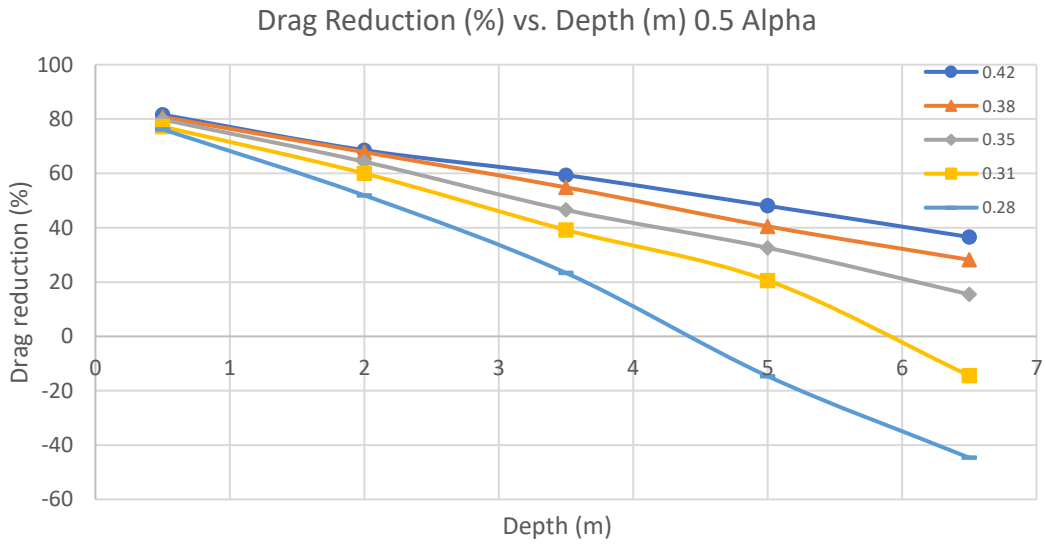
Drag Reduction (%) vs. Depth (m) 0.5 Alpha
Drag reduction (%)
Depth (m)
100
80
60
40
20
0
-20
-40
-60
0
1
2
3
4
5
6
7
0.42
0.38
0.35
0.31
0.28

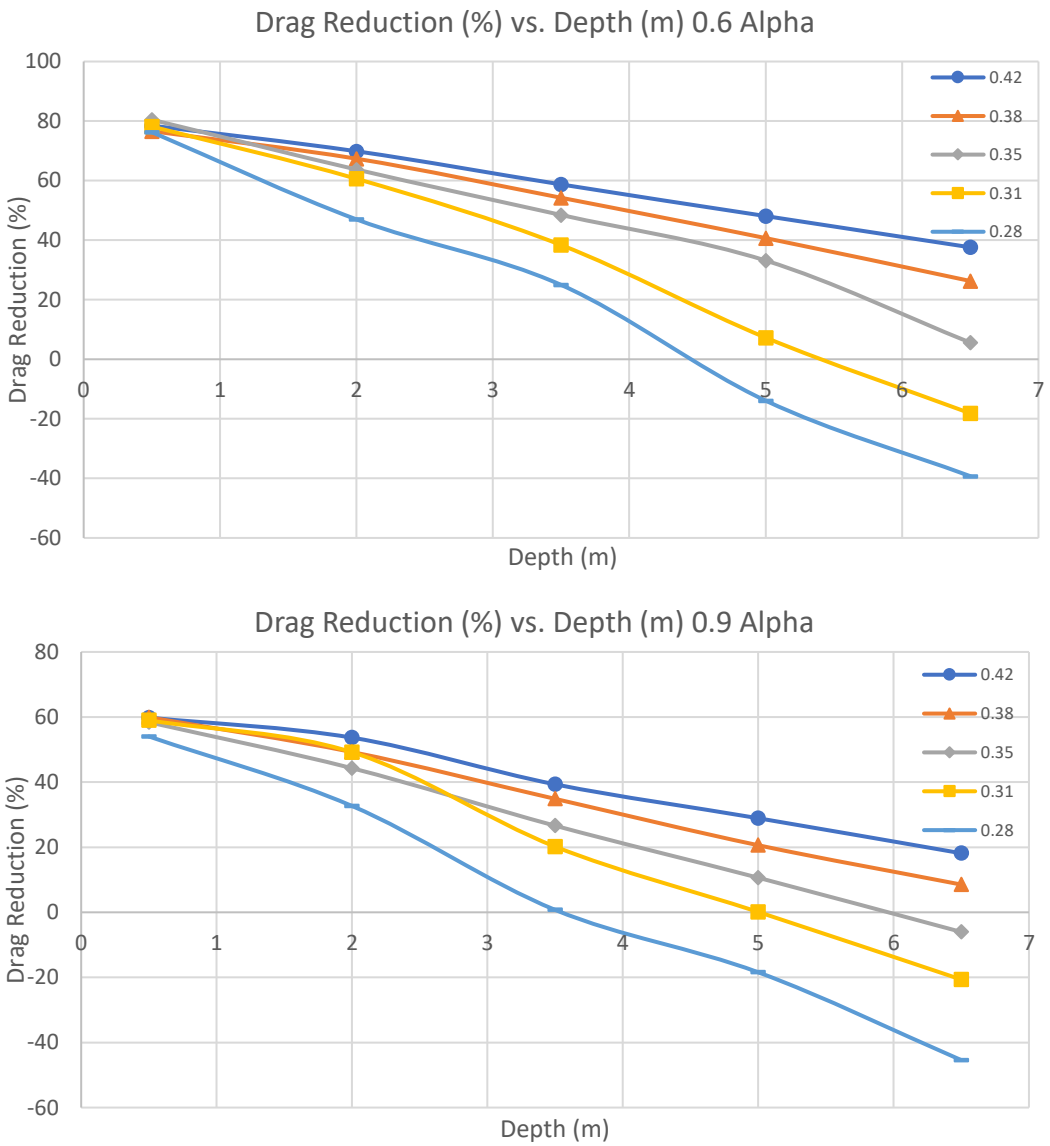

Figure 34: Graphs of Drag Reduction vs. Depth of Individual Alpha's

Table 16: Table of Correlation of Data

	Correlation				
Depth (m)	0.1	0.4	0.5	0.6	0.9
0.5	*-0.955*	*-0.998*	*-0.997*	*-0.997*	*-0.998*
2	*-0.996*	*-0.999*	*-0.990*	*-0.995*	*-0.992*
3.5	*-0.986*	*-1.000*	*-1.000*	*-0.992*	*-1.000*
5	*-0.954*	*-1.000*	*-1.000*	*-0.997*	*-0.999*
6	*-0.994*	*-0.997*	*-0.999*	*-0.999*	*-0.995*

Table 17: Table of R Squared Values of Data

	R-Squared Value				
Depth (m)	0.1	0.4	0.5	0.6	0.9
0.5	*0.912*	*0.997*	*0.994*	*0.994*	*0.995*
2	*0.992*	*0.998*	*0.979*	*0.990*	*0.985*
3.5	*0.972*	*1.000*	*0.999*	*0.984*	*0.999*
5	*0.910*	*0.999*	*1.000*	*0.994*	*0.998*
6	*0.989*	*0.995*	*0.998*	*0.998*	*0.990*

Table 18:Summary of Data from Same Plate Testing

	Mean %	Median %	Highest D.R. %	Lowest D.R. %
0.1	16.03	19.89	52.64	-41.36
0.4	43.15	47.43	79.69	-41.30
0.5	43.18	48.06	81.58	-44.66
0.6	42.03	48.09	80.46	-39.2
0.9	25.54	28.91	59.92	-45.42

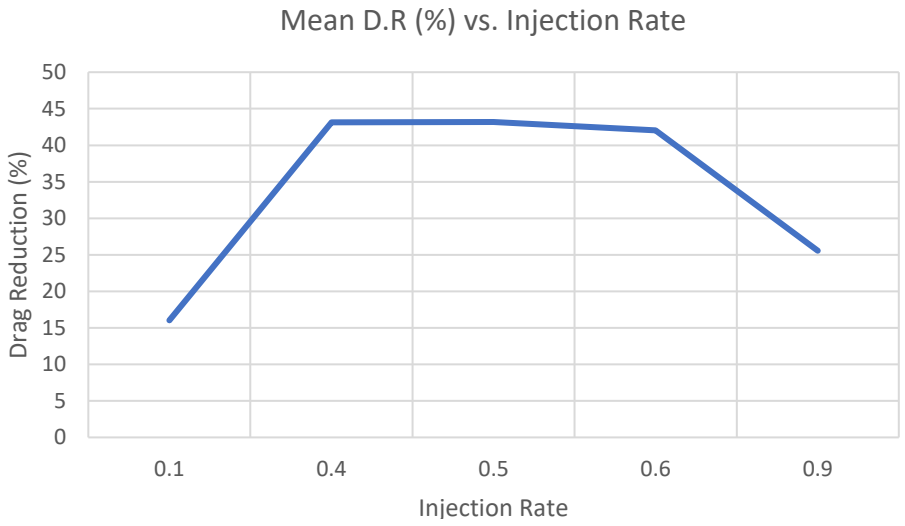

Figure 35: Mean D.R. of Different Injection Rates

All the numerical data can be seen in Table 58 to Table 62 in Appendix B.

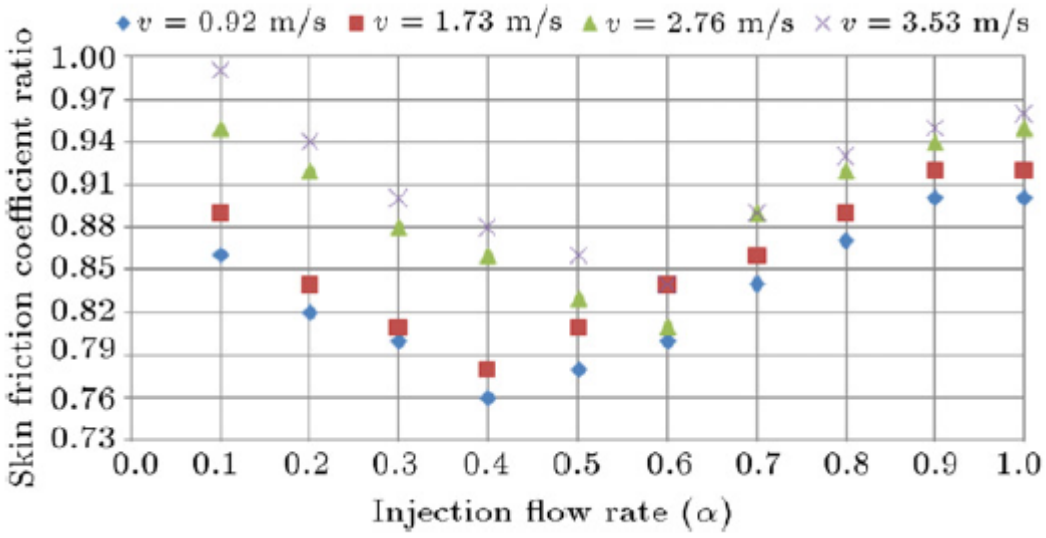

Figure 36:Optimal Injection Rate Study (Sayyaadi et al. 2013)

4.4.2.1 Comparing Data of D.R. vs. Froude Number

In this section the data is compared at the same depths at different Fr numbers across all depths. Figure 37 shows the graphs of drag reduction at different depths vs different Fr with the trendline plotted through the data points since the R-Squared value was so high.

It can be noted that in all the data points the highest drag reduction came for the injection rate of 0.4-0.6, further increasing the confidence in the CFD model in terms of the agreement with literature (Sayyaadi *et al.* (2013)) and Latorre (1997).

Even though the figures have a trend line going through them that has been extended to predict a higher Fr, this result will never be accurate because as the Fr of the vessels increases the relationship between viscous drag, pressure drag and wave making drag changes. MBDR only affects the viscous drag part of the vessel. Therefore, this graph would only be suitable for ships that operate within a velocity that is viscous drag dependent. In the literature it is said that the highest drag reduction is achieved at a lower velocity (Yao *et al. (*2011)), (Sayyaadi *et al.* (2013)), (Tsai *et al.* (2011)), (Kodama *et al.* (2000)) and (Sindagi *et al.* (2019)), but these tests were conducted without the effect of hydrostatic pressure on the drag reduction effect. Also, the testing was done

without an injection ratio. Injection rates were tested at different velocities, this means that the alpha of every test was varied and could not be compared.

The higher velocities also mean that there is more turbulence build-up on the plate and bubbles have to break down more eddies and structures, but depth has no effect on turbulence. As a result, when the plate goes deeper and at a higher velocity the bubbles must overcome the effect of hydrostatic pressure and the effect of increased turbulence. Having more air in the B.L., due to higher velocity, hinders the turbulence production and there will be more bubble splitting which will reduce turbulence (Stephani *et al.* (2006)),(Hussan *et al. (*2008)) and (Jiménez *et al.* (1999)).The effect of bubble in turbulence break-up is still not fully understood but a better understanding of the scale-up between increase of turbulence due to increase of velocity and turbulence break-up due to air injection, is needed. A possibility of modelling the plates using DNS and LES would possibly give more insight, but to run a similar plate size would be extremely computational expensive rendering almost impossible with current computer power.

Another observation is that at deeper drafts and lower velocity, the drag reduction effects keep reducing up to a point where it even starts to increase drag. Whilst there is no literature to explain this effect, the reasons for it could be multiple such as:

- Less splitting of the bubbles, hence less turbulence breakdown, since they will be smaller due to compressibility.
- Since the bubble diameter will be smaller, they are pushed and ejected from the T.B.L. more quickly.
- Since the density of air is increasing, the density ratio is also increasing. Studies by (Skudarnov *et al.* (2005)) and (Goolcharan, 2016) state that for the optimal drag reduction, a lower density air proves the highest drag reduction.
- Since the air density increases, the bubbles could act as a turbulence enhancer instead of the bubbles breaking down the turbulence.
- When the bubbles are ripped out they create a swirling motion which increase the drag on the plate

With the above mentioned they can act as B.L. modified in which the B.L. is modified in an unfavourable position.

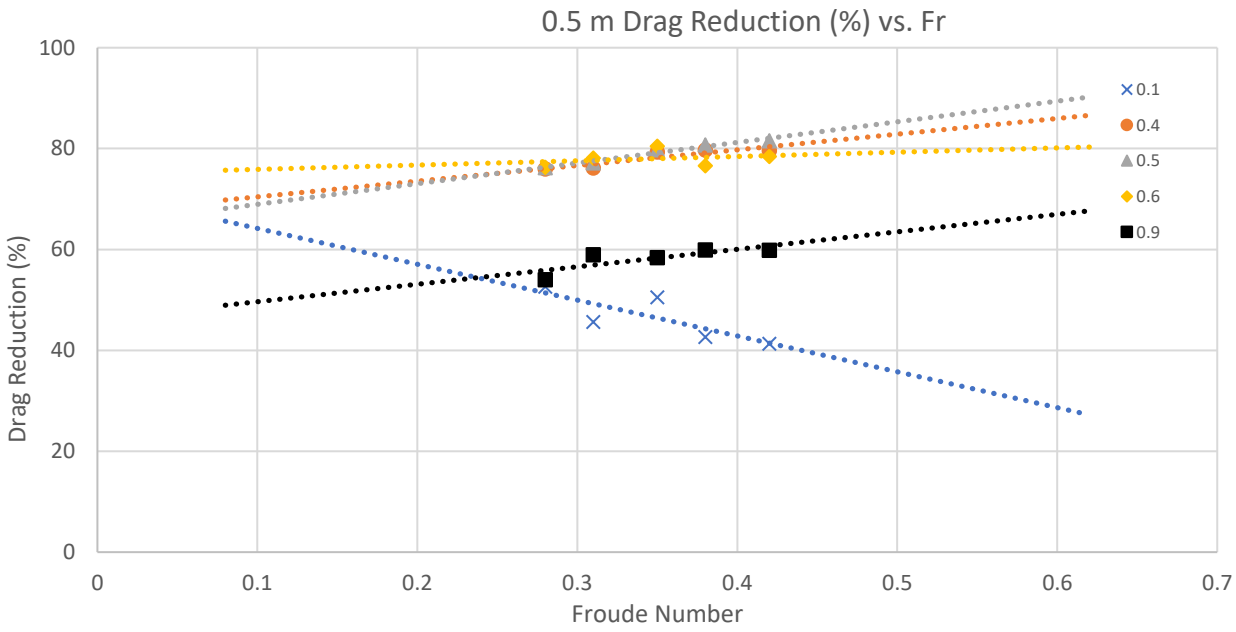
0.5 m Drag Reduction (%) vs. Fr
Drag Reduction (%)
Froude Number
0.1
0.4
0.5
0.6
0.9

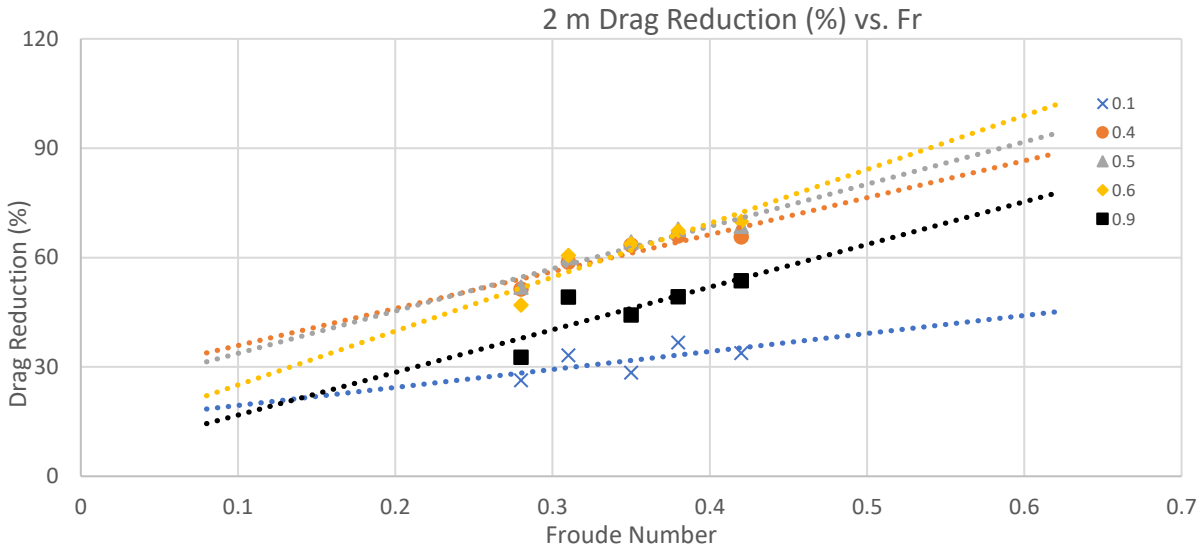
2 m Drag Reduction (%) vs. Fr
Drag Reduction (%)
Froude Number
0.1
0.4
0.5
0.6
0.9

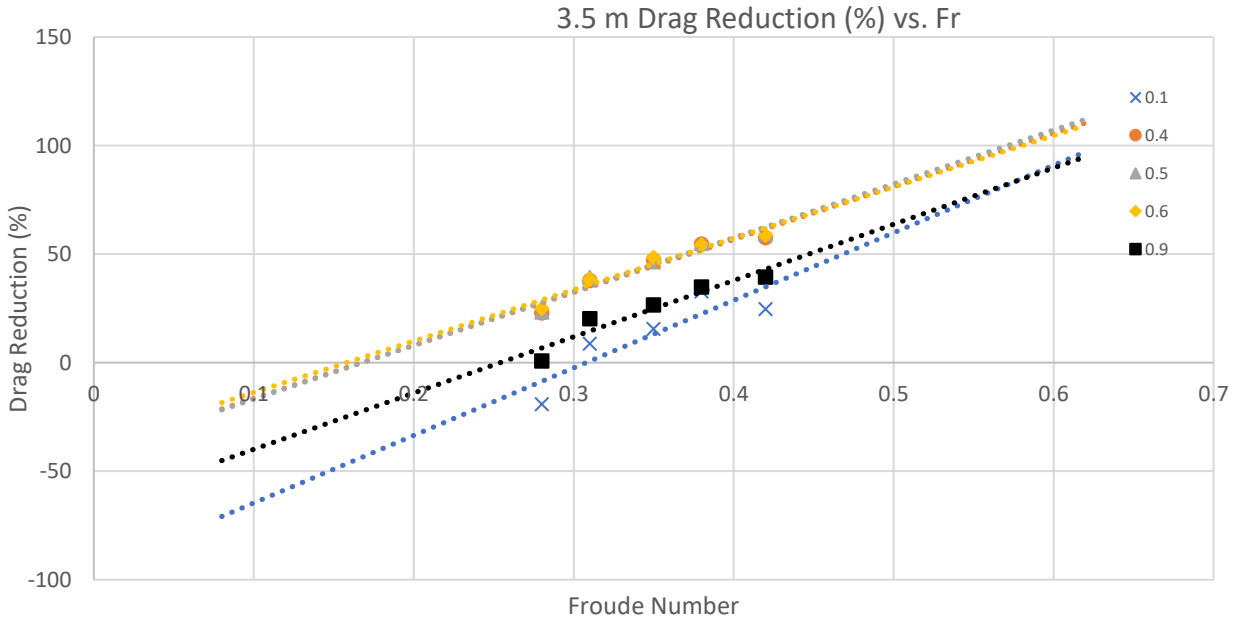
3.5 m Drag Reduction (%) vs. Fr
Drag Reduction (%)
Froude Number
0.1
0.4
0.5
0.6
0.9

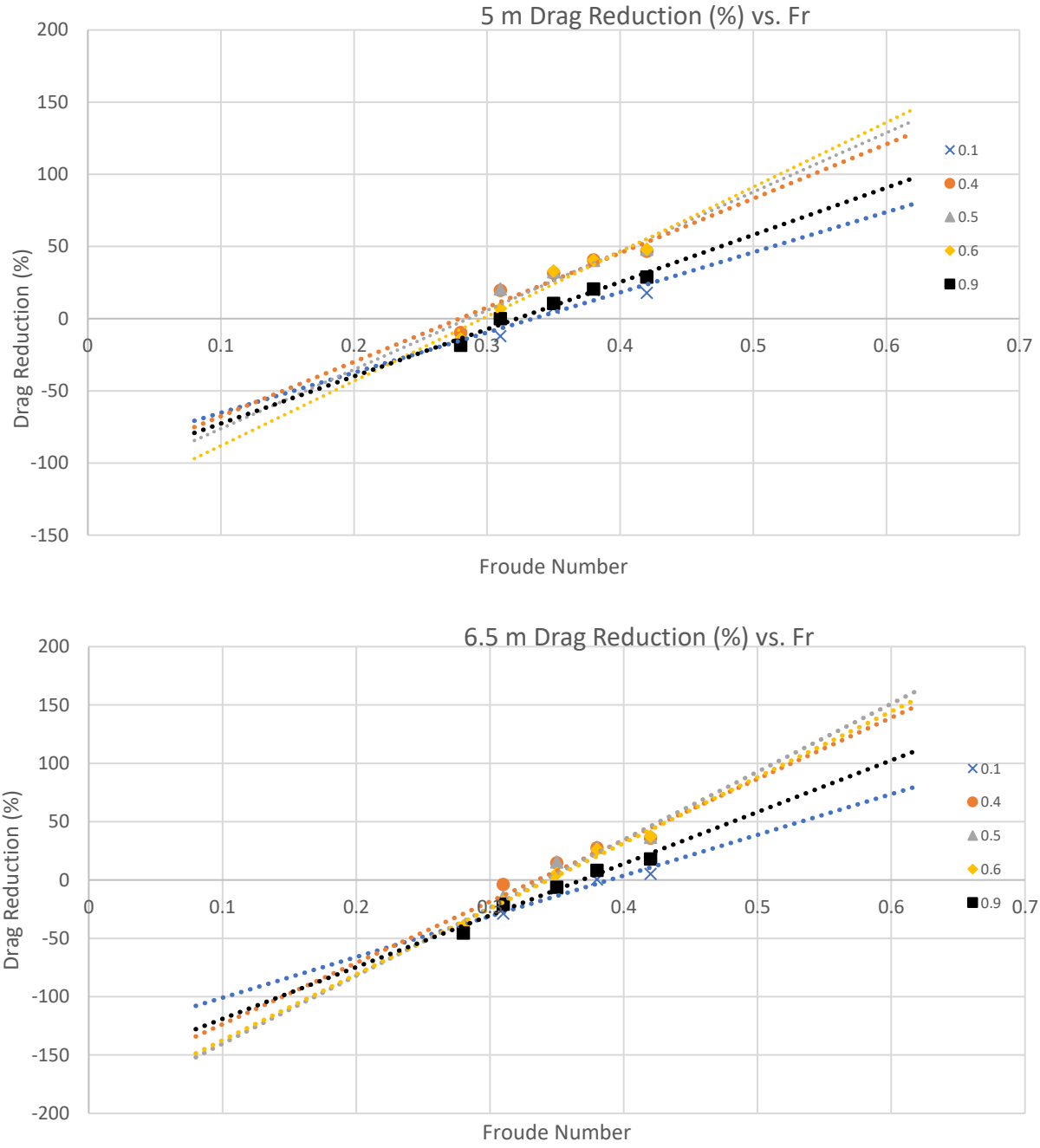

Figure 37: Graphs of D.R. at Different Depths vs. Froude Number

4.4.2.2 Comparing Data of D.R. vs. Depth

In this section the D.R. results were compared at the same Fr number across the depths for every Fr number. In Figure 38 the data is plotted with trendlines going through the data points. The x axis is extended up to 8.5 m and an accurate result could be predicted from the graphs plotted. The linear drop of drag reduction vs depth can immediately be noticed. This is verified by the statistical analysis done in Table 16 and Table 17 were the correlation value is over 95 % for all data points. Since the R-squared value is also close to one the data can be used as a predictive model for deeper drafts. Since the viscous effect of drag will remain the same irrespective of depth the trend lines can be used a predictive model for every Fr number plotted.

The mixing ratios 0.4 – 0.6 can be noticed to have the best drag reduction across all Fr numbers and across all depths as well. An interesting note to this is that the higher the Fr number goes the bigger the gap between 0.1,0.9 and 0.4-0.6. While there is no current explanation for this, it is thought that as the Fr increases, the turbulence will increase as well. Now for the 0.1 alpha there is not enough air to overcome this increase of turbulence so the air bubbles will be ejected from the T.B.L. immediately. For the 0.9 alpha, the oversaturation of the air acts as turbulence builds up therefore increasing the drag across certain points.

When the hydrostatic pressure increases the bubble size will change and become smaller. As the bubble become smaller their behaviour with the T.B.L. changes and this will change the D.R. effect. Another variable, that changes is the density ratio. Literature on the effect of density ratio is only limited to (Skudarnov *et al.* (2005) and (Goolcharan, 2016) currently. In their work they discovered that as the density ratio goes down the drag reduction effect decreases. With compressibility factored into the simulations the density ratio is constantly decreasing with increasing depth. Therefore, the reduction in drag reduction effect in this testing at depth could be a result of the increased density ratio. More research must be undertaken to separate the density effect from the effect of hydrostatic pressure.

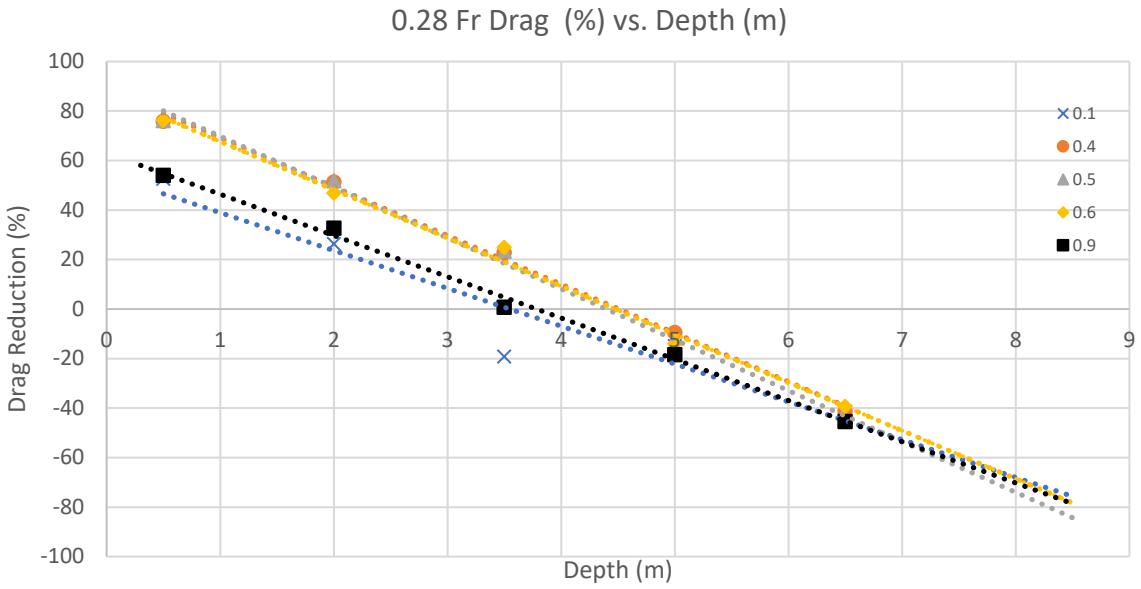
0.28 Fr Drag (%) vs. Depth (m)
Drag Reduction (%)
Depth (m)
0.1
0.4
0.5
0.6
0.9

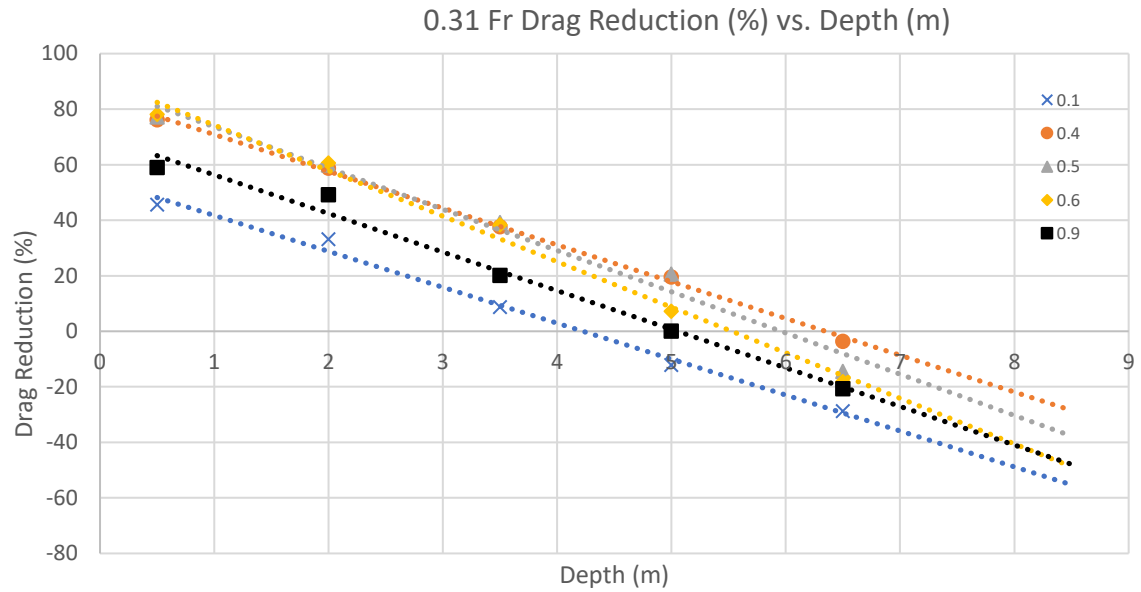
0.31 Fr Drag Reduction (%) vs. Depth (m)
Drag Reduction (%)
Depth (m)
0.1
0.4
0.5
0.6
0.9

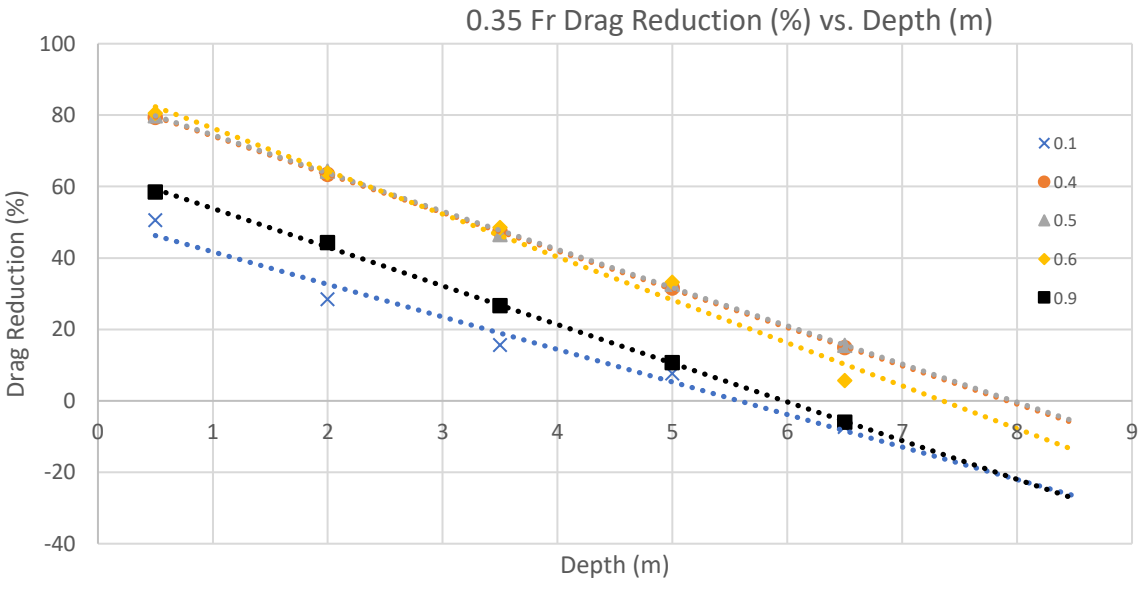
0.35 Fr Drag Reduction (%) vs. Depth (m)
Drag Reduction (%)
Depth (m)
0.1
0.4
0.5
0.6
0.9

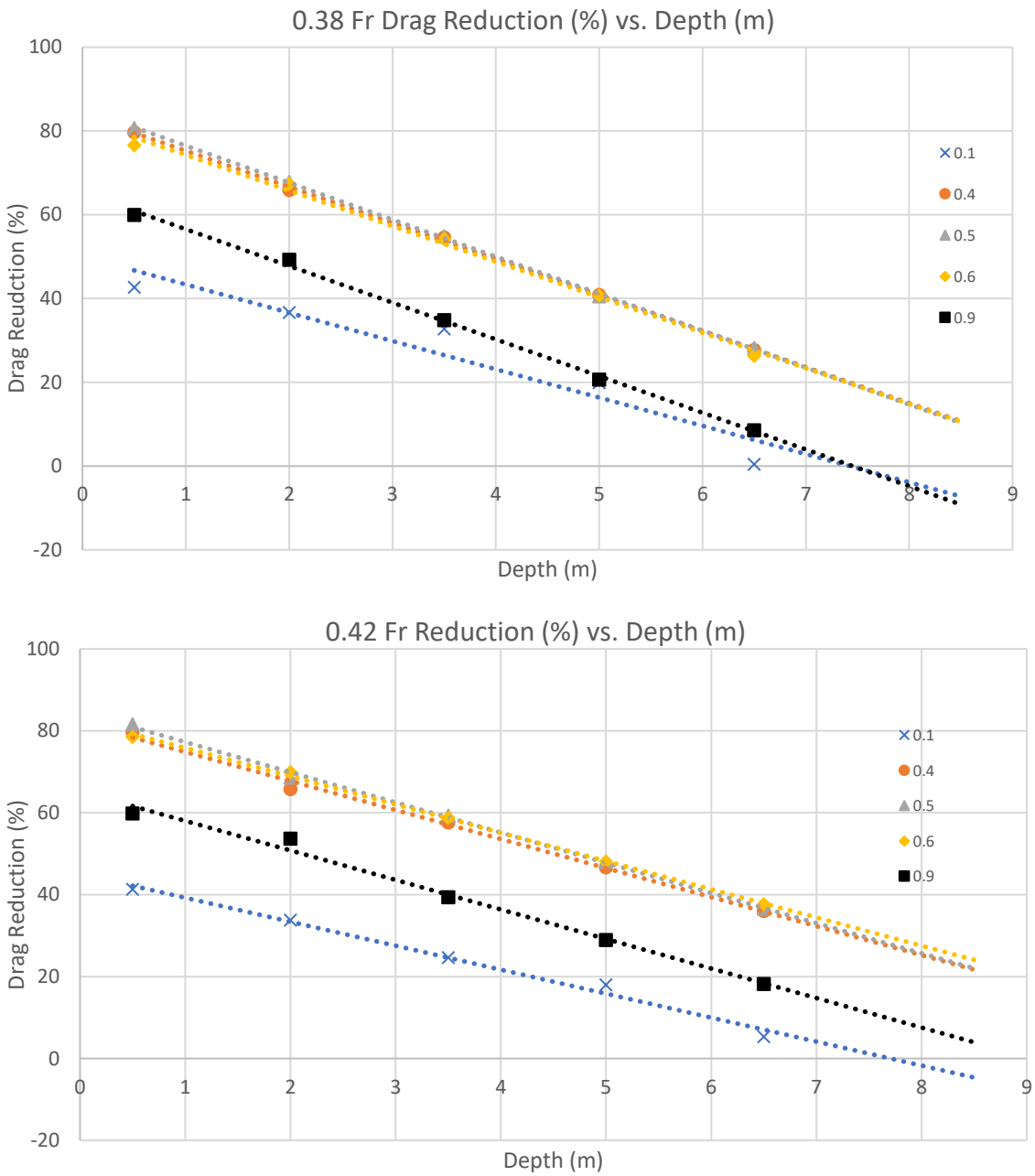

Figure 38: Comparing D.R. vs. Froude Number at Different Depths

Table 19:Table of Density Ratio

Depth (m)	Density of Air (kg/m^3)	Density Ratio
0.5	1.192	0.00120
2	1.373	0.00138
3.5	1.562	0.00157
5	1.726	0.00173
6.5	1.916	0.00192

4.4.3 Non-Dimensional Analysis

Non-dimensional analysis is used to reduce complex physical problems to a simpler form. It reduces the degrees of freedom of a problem to be used as a scaling law. It is mostly used to investigate new phenomena for which the boundary conditions and equation are not fully understood. To do this the Buckingham π theorem is used.

The theorem states that:

If there are n variables in a problem and these variables contain M primary dimensions (for example M – mass, L - Length, T - Time) the equation relating all the variables will have (n-m) dimensionless groups.

The final equation obtained will be in the form of:

$$\pi_1 = f(\pi_2, \pi_3 \dots \dots \pi_{n-m}) \tag{30}$$

The π terms are independent of each other, and they are not formed by the multiplication of each other. The steps for undergoing a dimensional analysis are as follows:

1. Select relevant variables (n)
2. Write the functional relationship
3. Select repeating variables
    i) Dependent variables are not selected
    ii) Variables should contain all M dimensions (M, L, T)

iii) Dimensionless variables are not selected as repeating

4. The number of $\pi - parameters$ are $n - m$
5. The groups are written by combining the repeating variables with each of the remaining variable and the equations is solved
6. The functional relationship is written

4.4.3.1 Numerical Working

The initial relevant variables are chosen as can be seen in Equation 31.

$$F = f(\rho, \mu, V, \dot{m}, H, L) \tag{31}$$

Table 20 shows the variables chosen and their respective unit. It is important to note that bubble size was omitted from this process. Using a RANS solver makes it very difficult to measure such. Therefore, this dimensional analysis will only be a partial analysis.

Table 20: Table of Variables

Variable	Variable Name	Unit
V	Velocity	$\frac{L}{T}$
ρ	Density of Water	M/L^3
μ	Viscosity	$\frac{M}{LT}$
$\dot{m}$	Mass Flow Rate	$\frac{M}{T}$
H	Hydrostatic Pressure	$\frac{M}{LT^2}$
L	Length of Plate	L
$F_{reduction}$	Reduction in Force	$\frac{ML}{T^2}$

Selecting the n variables gives us

$$n = 7$$

$$m = 3$$

Therefore, $n - m$ = 4

With the equation function being as seen in Equation 32

$$\pi_1 = f(\pi_2 \pi_3 \pi_4) \tag{32}$$

Writing the π terms give us Equations 33 to 36

$$\pi_1 = V^a \rho^b L^c F \tag{33}$$

$$\pi_2 = V^a \rho^b L^c m \tag{34}$$

$$\pi_3 = V^a \rho^b L^c \mu \tag{35}$$

$$\pi_4 = V^a \rho^b L^c H \tag{36}$$

4.4.3.2 Solving for π_1 – Reduction in Force

$$\pi_1 = \left[\frac{L}{T}\right]^a \left[\frac{M}{L^3}\right]^b [L]^c \frac{ML}{T^2} \tag{37}$$

$$\pi_1 = L^{a-3b+c+1} \times T^{-a-2} \times M^{b+1} \tag{38}$$

Equating coefficients of M, L and T and solving results in Equation 39

$a - 3b + c - 1 = o$	$c = -2$	(39)
$-\mathrm{a} - 2 = 0$	$a = -2$	
$b + 1 = 0$	$b = -1$	

Substituting the values in Equations 37 – 39 results in π_1

$$\pi_1 = \frac{F}{V^2 \rho L^2} \tag{40}$$

4.4.3.3 Solving for π_2 – Mass Flow Rate

$$\pi_2 = \left[\frac{L}{T}\right]^a \left[\frac{M}{L^3}\right]^b [L]^c \frac{M}{T} \tag{41}$$

$$\pi_2 = L^{a-3b+c} \times T^{-a-1} \times M^{b+1} \tag{42}$$

Equating coefficients of M, L and T and solving for Equation 43

$a - 3b + c = o$	$c = -2$	(43)
$-\mathrm{a} - 1 = 0$	$a = -1$	
$b + 1 = 0$	$b = -1$	

Substituting the values in Equations 41 to 43 results in π_2

$$\pi_2 = \frac{\dot{m}}{V\rho L^2} \tag{44}$$

4.4.3.4 Solving for π_3 - Viscosity

$$\pi_3 = \left[\frac{L}{T}\right]^a \left[\frac{M}{L^3}\right]^b [L]^c \frac{M}{LT} \tag{45}$$

$$\pi_3 = L^{a-3b+c+1} \times T^{-a-1} \times M^{b+1} \tag{46}$$

Equating coefficients of M, L and T and solving for Equation 47

$a - 3b + c - 1 = o$	$c = -1$	(47)
$-\mathrm{a} - 1 = 0$	$a = -1$	
$b + 1 = 0$	$b = -1$	

Substituting the values in Equations 45 -47 results in π_3

$$\pi_3 = \frac{\mu}{V\rho L} \tag{48}$$

Equation 49 is the upside-down version of Reynolds Number. Since it is dimensionless the values can be flipped for Equation 49.

$$\pi_{3'} = \frac{V\rho L}{\mu} \tag{49}$$

This further strengthens and confirms the hypothesis that to understand the scaling effect, the effect of hydrostatic pressure and Reynolds Number should be separated.

4.4.3.5 Solving for π_4 – Hydrostatic Pressure

$$\pi_4 = \left[\frac{L}{T}\right]^a \left[\frac{M}{L^3}\right]^b [L]^c \frac{M}{LT^2} \tag{50}$$

$$\pi_4 = L^{a-3b+c-1} \times T^{-a-2} \times M^{b+1} \tag{51}$$

Equating coefficients of M, L and T and solving for Equation 52

$a - 3b + c - 1 = o$	$c = -1$	(52)
$-\mathrm{a} - 2 = 0$	$a = -1$	
$b + 1 = 0$	$b = -1$	

Substituting the values in Equations 49 to 52 results in π_4

$$\pi_4 = \frac{H}{V^2\rho L} \tag{53}$$

4.4.3.6 Final Function

The initial equation in Equation 20 can be written as Equation 54

$$\frac{F}{V^2\rho L^2} = f\left(\frac{m\cdot}{V\rho L^2} \times \frac{V\rho L}{\mu} \times \frac{H}{V^2\rho L}\right) \tag{54}$$

Further simplifying Equation 54 results in Equation 55

$$F = [(V \times L \times \mu) \times (m\cdot \times V) \times (H \times L)] \tag{55}$$

Unfortunately solving Equation 55 gives an incorrect value. This is because several parameters that could not be calculated using a RANS CFD model were excluded such as the effect of TKE, bubble size, full Eddie effects etc. Equation 42 for π_2 was of interest to the author as the MFR equation considers the velocity of the vessel and the density of air which represents the hydrostatic pressure. Therefore, Equation 42 was investigated further.

4.4.3.7 Investigation of π_2

Since the equation of MFR encapsulated several of its ALS variables (hydrostatic pressure and velocity) in its initial Equation 17, the drag reduction of all mixing ratio was plotted against the coefficient of equation 44, excluding negative results, in Figure 39. Equation 44, π_2 was labelled as Sigma. It can be noticed immediately that even though the graphs are not a perfect straight line the R-squared value is still acceptable as can be seen in Table 21.

The correlation can be seen in Table 22 and the values are very close to -1 indicating a strong linear relationship. Therefore, a level of predictability could be reached. Since the equation is not finalised the individual mixing ratios could not be adjusted to create one line, but instead every mixing ratio had its own trend. Another point that can be highlighted is that the higher the mixing ratio the less the R-Squared value. This could be because the higher the injection rate, the higher the turbulence or another value that cannot be encapsulated with the mass flow rate equation as mentioned previously.

The highlight of Figure 39, is that even though further work is needed to include every variable that affects drag reduction when using MBDR, the current equation still manages to create a good predictive mode and, irrespective of the depth of the plate, when normalised, the data falls on a single line.

This would suggest that a full-size plate could be modelled at different depths and a similar graph could be plotted and this could be used for all operating drafts of a ship.

The data for Figure 39 can be seen in Table 63 - Table 67 in Appendix B.

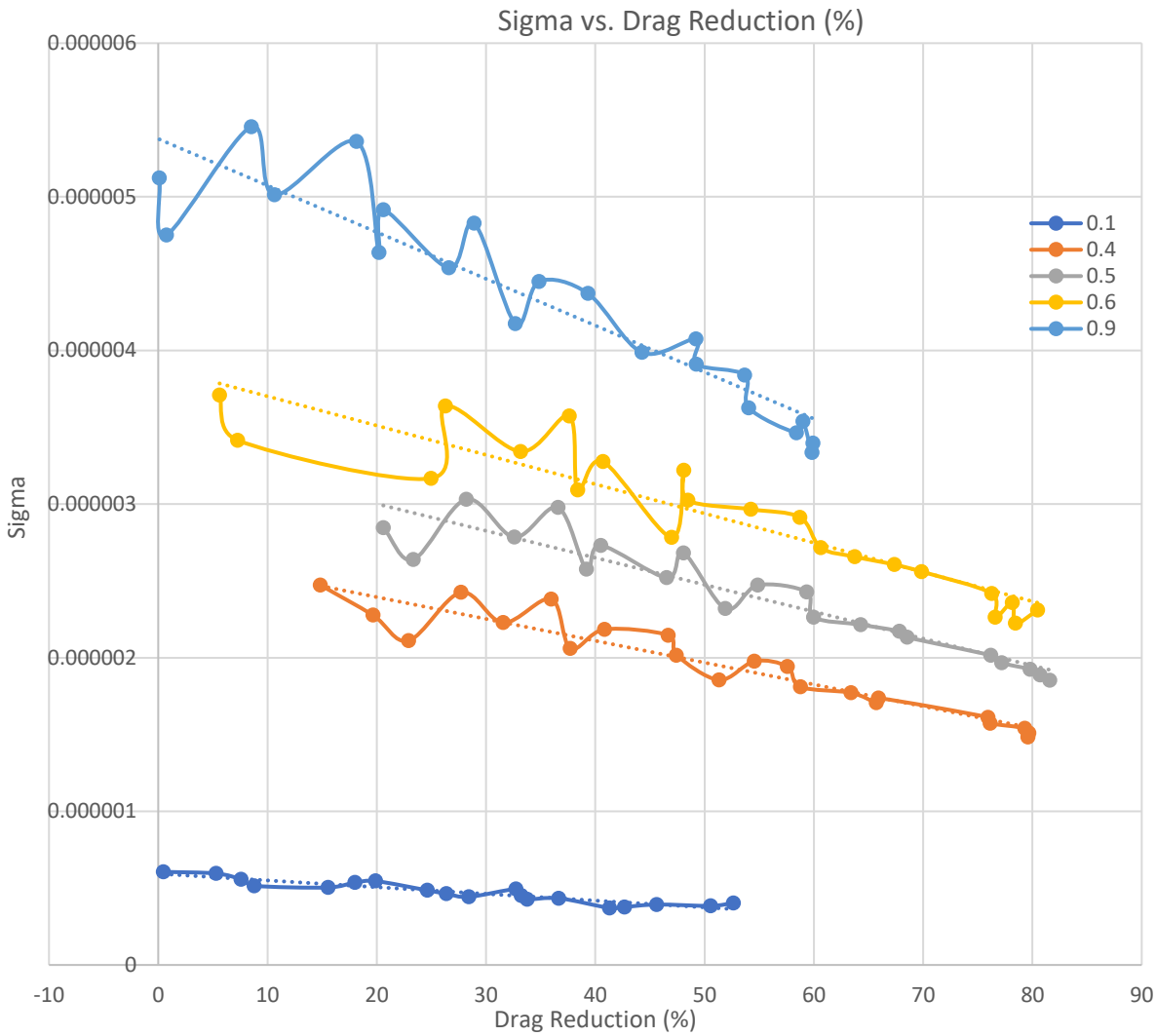

Figure 39: Graph of Sigma vs. Drag Reduction

Table 21: Table of R-Squared Value for Sigma

Alpha	R-Squared Value
0.9	*0.86*
0.6	*0.86*
0.5	*0.89*
0.4	*0.9*
0.1	*0.87*

Table 22: Table for Correlation Value for Sigma

Alpha	Correlation
0.9	*-0.926*
0.6	*-0.926*
0.5	*-0.950*
0.4	*-0.949*
0.1	*-0.933*

4.5 Re Testing

In this section the results of three increasing Re numbers will be compared. The mixing ratios of 0.4 – 0.6 were chosen. In the previous section the results of these mixing ratios proved to be the optimal, therefore it was decided that more focus should be put into these three mixing ratios. This will give a better understanding of the optimal injection point.

4.5.1 Grid Refinement Study

A grid refinement study as can be seen in Figure 40 was performed using three base sizes and the error was calculated by using the in Equation 29. A base size of 0.274 was chosen as it gave the least amount of difference when compared to empirical equations whilst taking an appropriate simulation time.

Figure 41 shows the graph of the calculated drag force on the plate data vs. the data of the CFD using no air injection. The errors of this graph can be seen in Table 23. The error is acceptable for the chosen set-up and the testing proceeded with this set-up.

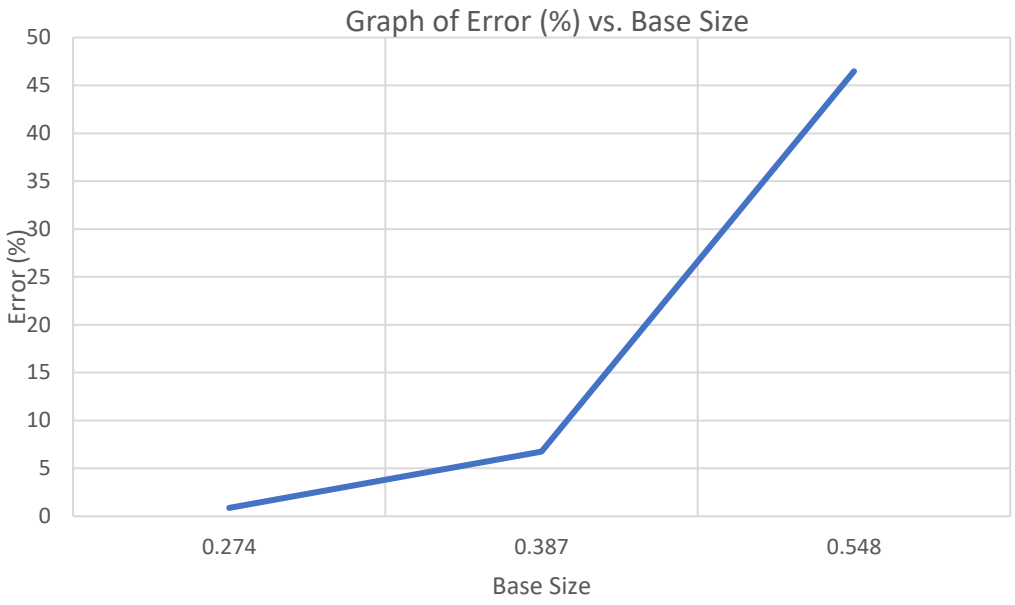

Figure 40: Grid Refinement Study for Re Testing

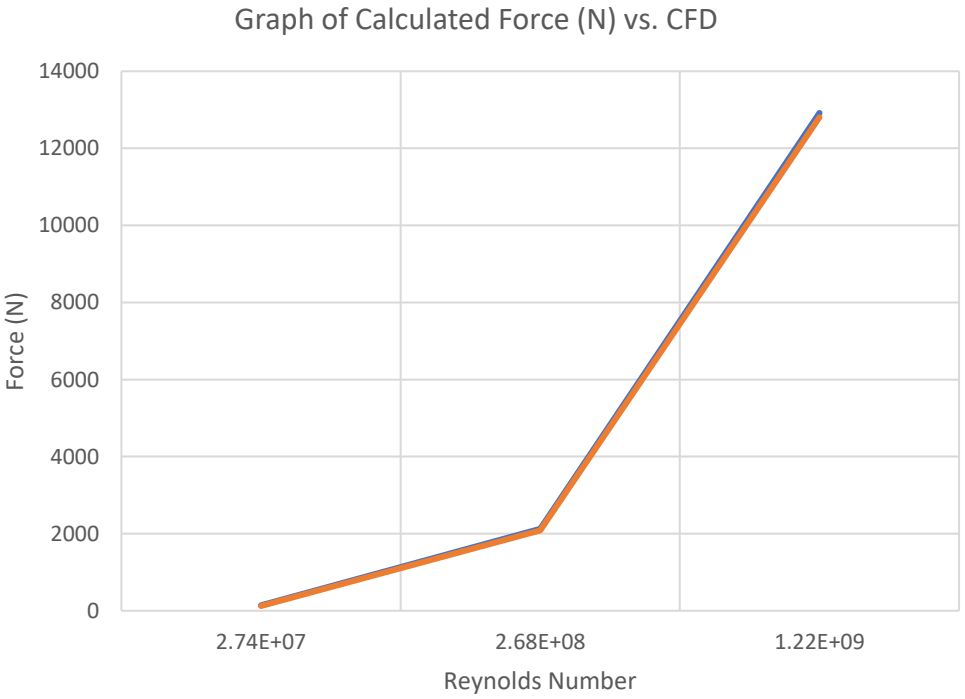

Figure 41: Graph of Calculated Force on Plate vs. CFD Force for Reynolds Testing

Table 23: Table of Error for Re Testing

Re	Calculated Drag (N)	CFD (N)	Error %
$2.74x10^7$	*140.38*	*124*	*11.67*
$2.68x10^8$	*2,123.14*	*2,086*	*1.75*
$1.22x10^9$	*12,918.49*	*12,806*	*0.87*

4.5.2 Mass Flow Rate

Figure 42 shows the MFR used for the Re testing with varying mixing ratios (0.4 to 0.6). Table 68 in Appendix B shows all the data points for the MFR.

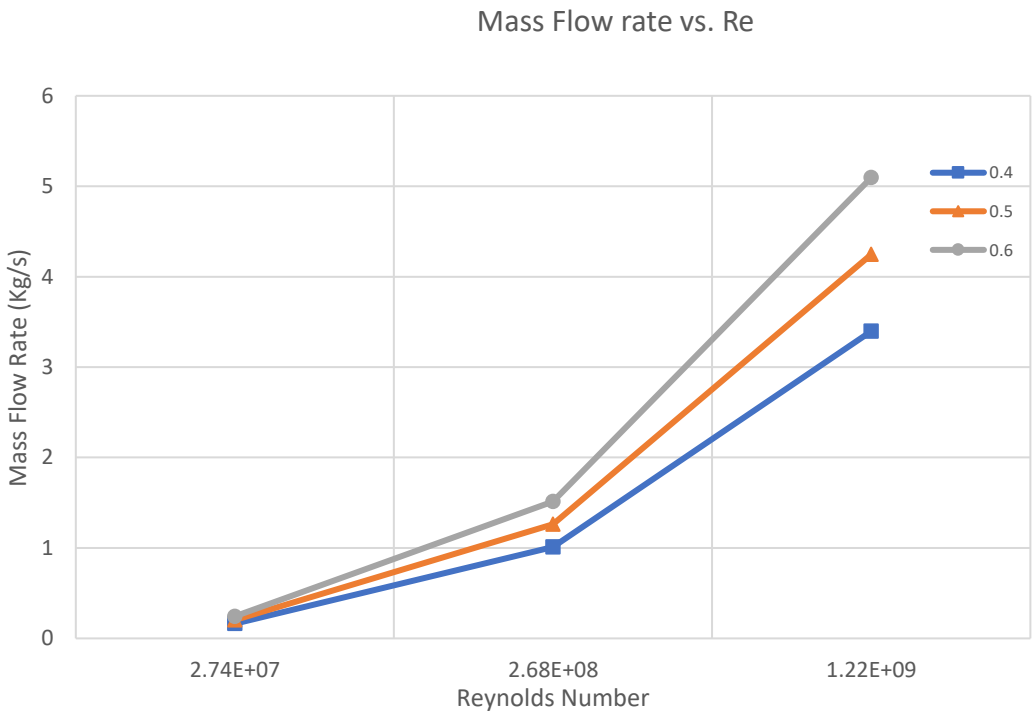

Figure 42: Mass Flow Rates used for Reynolds Testing

4.5.3 Results for Reynolds Number Testing

In Table 24 and Figure 43 the results of the Reynolds number testing can be seen. Table 25 shows the statistical analysis for the results. In Figure 43, it can be noticed that the initial drag reduction result for all alpha, at the lower Re number of *2.74E+07,* has the

highest value. As the Re number increases the effect of drag reduction decreases, this agrees with the works of Sanada *et al.* (2009) and Legendre *et al.* (*2*003) . The mixing ratio of 0.4 alpha has the highest reduction of efficiency, with a drop of 17.95 %. This suggests that for a vessel operating across a series of Re a large mixing ratio would have a better overall D.R. The range of the results can be seen in Table 26.

In Table 25 we can see that the Correlation and the R-squared values decrease with increasing alpha. This suggests that as Re increases more variables start effecting the D.R. effect. Also, as the Re increase the effect of compressibility will increase as the bubbles will break up faster. Whilst there is no one definite answer several reasons have been highlighted in literature such as:

- Sanada *et al.* (2009) observed that the bubble trajectory and its place within the T.B.L. is strongly dependent on the Re. If the bubble escapes the T.B.L. earlier the drag reduction effect will reduce drastically.
- Legendre *et al.* (*2*003) used DNS to model two solid spheres to study their relative motion and direction. It was concluded that direction and motion changed in accordance with the Re. This could lead to bubbles existing the T.B.L. earlier.
- The higher the Re, the higher the turbulence shearing effect and bubble breaking; therefore, bubble escaping will increase. This can result in a problem of persistence down stream of injection (Pavlov *et al.* (2020)).
- Hara *et al.* (2011) states that at high Re, the turbulent stress has greater importance on drag than viscous stress, therefore most of the drag reduction effect will come from the breaking down of these turbulence stresses.

As a final comment the reduction in the effect of drag reduction can also be confirmed with the dimensional analysis done in the previous section with Equation 41.

Table 24: Table of Re Testing Results

Drag Reduction %			
Re	0.4	0.5	0.6
1.22E+09	*78.18*	*87.19*	*83.69*
2.68E+08	*91.49*	*91.46*	*85.25*
2.74E+07	*96.13*	*97.03*	*97.20*

Table 25: Table of Statistical Analysis of Re Testing

Statistical Analysis		
Alpha	Correlation	R-Squared
0.4	*-0.998*	*0.996*
0.5	*-0.918*	*0.843*
0.6	*-0.732*	*0.536*

Table 26:Table of Range for Re Testing

Range		
0.4	0.5	0.6
17.94	9.84	13.51

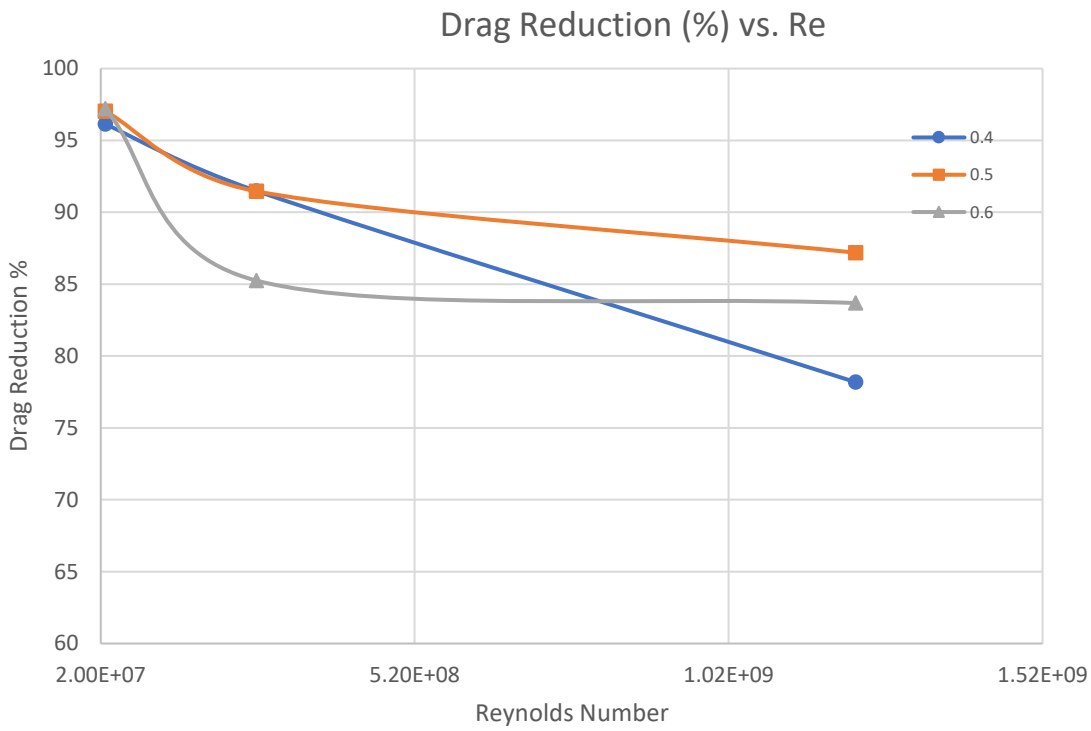

Figure 43: Graph of Drag Reduction vs. Reynolds Number for Re Testing

4.6 Scaling Up Plate

In this section the plates were scaled up to full size. Two different plate sizes were used, a full size one for λ = 1 and a medium size plate for a λ = 1.86. It was discovered that if the base size value for the CFD simulations was scaled up with the same scaling factor the base size would be relevant to the new scale. Table 27 Table 27 shows how the base sizes were scaled up whilst Table 28 shows the Re number.

Table 27: Table of Scaling Base Size

	Small	**Medium**	**Large**
Base Size	0.022	0.154	0.286
Scaling Ratio (λ)	13	1.86	1

Table 28: Table of Re for Scaling Testing

Reynolds Number	
Medium Plate	Large Plate
1.27E+07	*5.09E+08*
1.14E+07	*5.75E+08*
1.35E+07	*6.40E+08*
1.23E+07	*7.06E+08*
1.12E+07	*7.72E+08*

The plate's initial drag force was calculated by using Equation 1. The data obtained from CFD over the flat plate was then compared against this data as can be seen in Table 29, Table 30 and Figure 44. The error was of an acceptable level for both plates, so that the base sizes shown in Table 27 were used for the testing.

Table 29: Table of Validation for Medium Size Plate

Medium Size Plate			
Fr	Calculated Drag (N)	CFD (N)	Error (%)
0.28	7,957.38	7,523.00	5.46
0.31	9,977.27	9,456.00	5.22
0.35	12,206.06	11,727.00	3.92
0.38	14,640.54	14,043.00	4.08
0.42	17,277.84	16,713.00	3.27

Table 30: Table of Validation for Large Size Plate

Full Size plate			
Fr	Calculated Drag (N)	CFD (N)	Error (%)
0.28	44,637.16	44,398.00	0.54
0.31	55,967.75	55,962.00	0.01
0.35	68,470.22	68,013.14	0.67
0.38	82,126.49	81,729.56	0.48
0.42	96,920.50	96,790.64	0.13

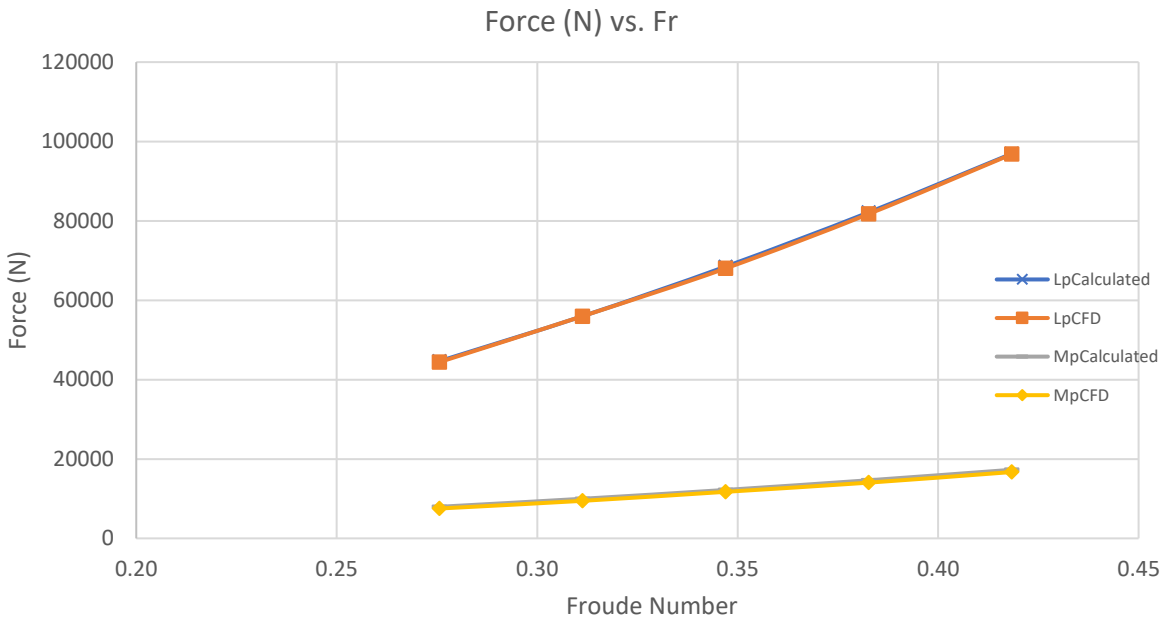

Figure 44: Graph of Calculated Force on the Flat Plate vs. CFD result

4.6.1 Scaling up Testing Results

Table 31,Table 32 and Table 33 shows the results for the scaling up testing. Table 34, Table 35 and Table 36 show the statistical analysis of the data. Table 37 and Table 38 show the percentage error whilst Figure 45 gives a graphical view of the data.

The range of error for the large plate is from -13.46 % to -0.6 % whilst for the medium plate the range of error is -15.92 % and 6.49 % error. Error was calculated against from drag reductions first small plate at 0.5 m. This is an acceptable level as a single-phase CFD resistance simulation has an acceptable error of 10 % (Frisk *et al.* (2015)). This strengthens the argument that when extrapolating to full size, both the MFR and the injection area must be scaled up.

The pattern in Figure 45 shows a trend that as the Fr increase the error decreases. This is an interesting phenomenon as with an increase of Fr there is an increase in Re. This behaviour is unexplainable yet.

On first sight the result for alpha 0.6 for the medium plate does not follow the trends of the other results. It should be noted that for the medium plate the 0.6, 0.5 and 0.4 alpha stack on top of each other in a similar pattern. Therefore, it can be thought that

the behaviour of the 0.6 alpha is not an irregularity but a behaviour of the system at that point.

It is not understood if the CFD simulation for the small plate underestimates the D.R. effect or the medium and larger plates overestimate the D.R. effect. This behaviour cannot be fully explained without delving deeper into air-water interaction and capturing the turbulence scales.

It can be noted in Table 34, Table 35 and Table 36 that the higher the injection rate the lower the R-squared value. It is important to note that for the R-Squared value calculation only two variables are used, the drag reduction value and the Fr. Whilst for the same plate size the R- squared value was very high for the scaling up or small plate results these values are less for the large plate.

This falls in line with the hypothesis that turbulence plays a more important part as the injection rate and velocity increases. Also, for the plate the Re number also increases, hence increasing the turbulence with the T.B.L. This also explains why Equation 54 created using the Pi – Buckingham method has several variables. The following are explanations for the error in the scaling results:

- Bubble Size: whilst some researchers argue that the bubble size is not an important factor others argue that it is. The bubble size will affect the turbulence build-up and turbulence vortices. When scaling up the plate, the bubble will change in size and the bubble diameter is a function of the shear force acting on the bubble and flow velocity (Moriguchi *et al.* (2002)), (Kawamura *et al.* (2002)) and (Elbing *et al.* (2008)).
- Bubble Coalescence and Splitting: The bubbles can both coalescence and split within the T.B.L. This will affect persistence downstream of the injector. Scaling up the plate will alter this behaviour as the turbulence will increase with higher Re and flow velocity (Perret *et al.* (2015)). As the bubbles break apart, the diameter decreases, making the bubbles smaller. As the bubbles get smaller, they are pushed away from the wall due to buoyancy effects. This leads to recovery of T.B.L. As smaller bubbles escape from the T.B.L., away from the point of injection, only larger bubbles remain, resulting in a decrease in void fraction

and bubble concentration. The higher the Re, the higher the turbulent shear effect and bubble collapse; therefore, the bubble leakage will increase and as the bubble escape they will create swirls and vortices (Pavlov *et al.* (2020)) and (Kawamura *et al.* (2003)). This will also affect turbulence breakdown and turbulence energy scales (Ferrante *et al* (2004)) and (H.Miyata, 2001).

- Bubble Trajectory: Since both the Re and flow velocity will change, the trajectory of the bubble within the T.B.L. will also change. Sanada *et al.* (2009) studied the trajectory of bubbles within the T.B.L. and he observed that there was a strong correlation with Re. This was later proven by Legendre *et al.* (2003) who modelled two solid spheres using DNS to study their relative motion and orientation. It is concluded that orientation and motion are changed according to Re.
- Density Ratio: The density ratio will change with depth. Even though in this previous work the effect of hydrostatic depth was studied, and a predictive model was created the density ratio effect could not be separated from the effect of hydrostatic pressure.
- Limitations of CFD: whilst a robust CFD model was built that managed to capture the swirling motion of the air escaping to the side and the error was within an acceptable level, using a more accurate turbulence model would replicate real life results better.

Table 31: Table of Small Plate 0.5 m Depth Results

Small Plate 0.5 m Depth (%)			
	Alpha		
Fr	0.4	0.5	0.6
0.28	75.95	76.19	76.28
0.31	76.15	77.19	78.16
0.35	79.31	79.80	80.46
0.38	79.69	80.72	76.60
0.42	79.59	81.58	78.46

Table 32: Table of Medium Plate 3.5 m Depth Results

Medium Plate 3.5 m Depth (%)			
	Alpha		
Fr	0.4	0.5	0.6
0.28	88.04	84.36	76.49
0.31	84.36	81.88	77.40
0.35	85.78	81.81	75.24
0.38	86.77	85.45	82.95
0.42	87.54	85.97	86.38

Table 33: Table of Large Plate 6.5 m Depth Results

Large Plate 6.5 m Depth (%)			
	Alpha		
Fr	0.4	0.5	0.6
0.28	81.87	85.95	85.53
0.31	82.58	81.82	83.24
0.35	82.36	85.30	86.71
0.38	81.74	84.44	86.88
0.42	80.07	82.52	86.06

Table 34: Statistical Analysis for the Small Plate

Small Plate 0.5 m Depth		
Fr	Correlation	R- Squared Value
0.4	0.895	0.800
0.5	0.979	0.958
0.6	0.265	0.070

Table 35: Statistical Analysis for the Medium Plate

Medium Plate 3.5 m Depth		
Fr	Correlation	R- Squared Value
0.4	0.153	0.023
0.5	0.548	0.300
0.6	0.841	0.708

Table 36: Statistical Analysis for the Large Plate

Large Plate 6.5 m Depth		
Fr	Correlation	R- Squared Value
0.4	-0.710	0.504
0.5	-0.377	0.142
0.6	0.506	0.256

Table 37: Table of Medium Plate Percentage Error

Medium Plate Percentage Error (%)			
Fr	0.4	0.5	0.6
0.28	-15.92	-10.72	-0.27
0.31	-10.79	-6.07	0.96
0.35	-8.15	-2.53	6.49
0.38	-8.89	-5.86	-8.28
0.42	-9.98	-5.38	-10.09

Table 38: Table of Large Plate Percentage Error

Large Plate Percentage Error (%)			
Fr	0.4	0.5	0.6
0.28	-7.80	-12.80	-12.12
0.31	-8.46	-6.00	-6.50
0.35	-3.84	-6.89	-7.76
0.38	-2.58	-4.61	-13.42
0.42	-0.60	-1.15	-9.67

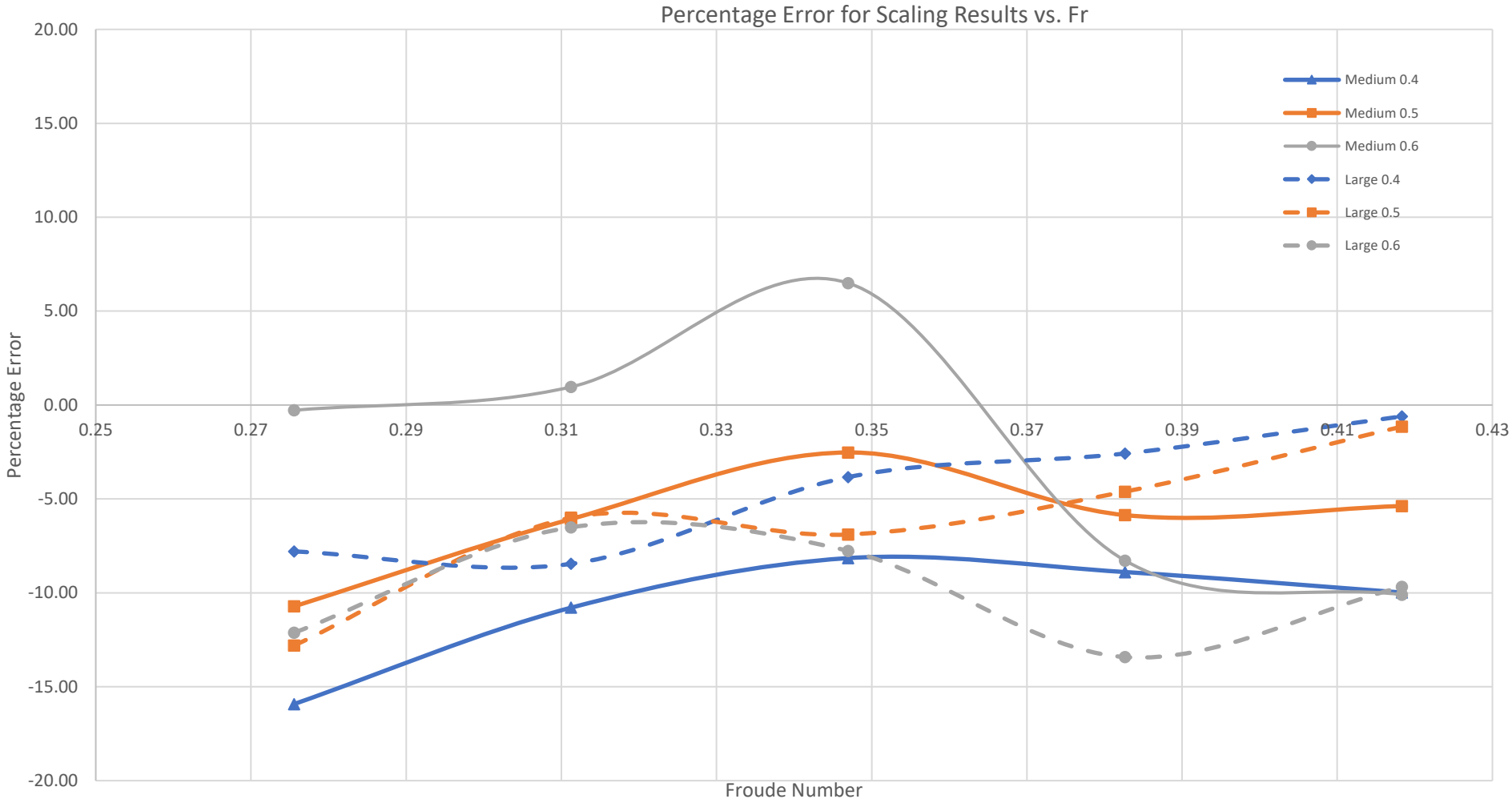

Figure 45: Graph of Error of Scaling up Results for the Medium and Large plate

4.6.2 Validation against Literature

In the absence of any experimental testing and data, several research studies are reviewed and compared in this section against the behaviour of the developed CFD model and results versus the behaviour of experimental data from other researchers.

4.6.2.1 Bubble Oscillations

Experimental laboratory work done by Qin *et al.* (2017) shows oscillation in D.R. due to bubble motion and behaviour. In the first part of Figure 46 air is injected at point 0 on the x-axis, which is the injection point. Then further away from the injection point the air layers break down into bubbles. This can be seen in Figure 47 part IV as these results is oscillating due to the motions of the bubbles forces of drag, lift, and force in the T.B.L.

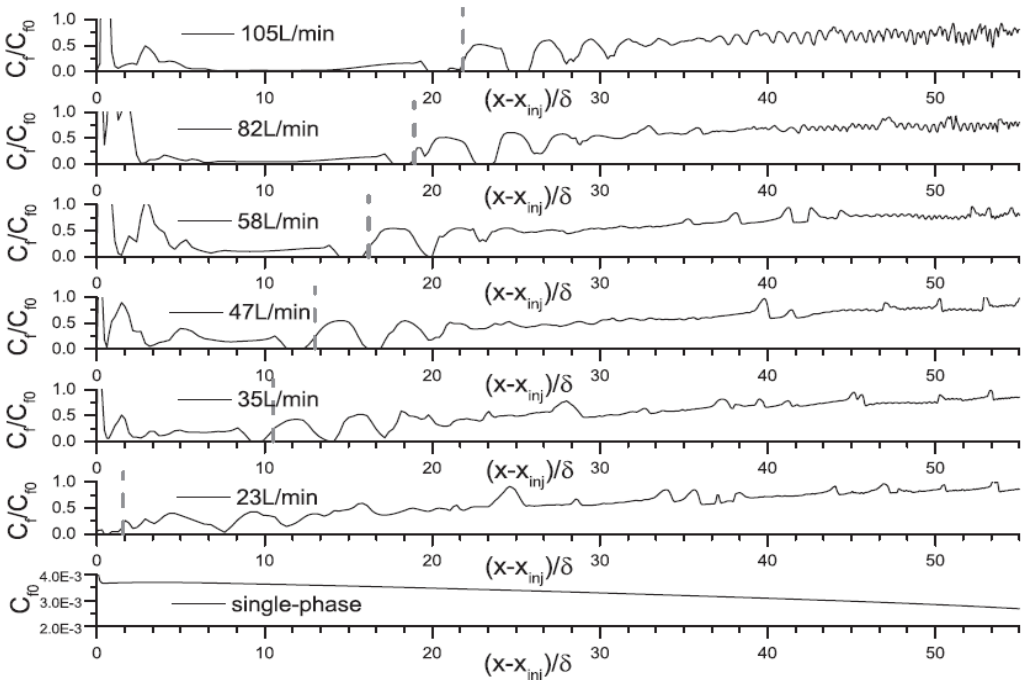

Figure 46: D.R. Across the Length of a Flat Plate (Qin et al. 2017).

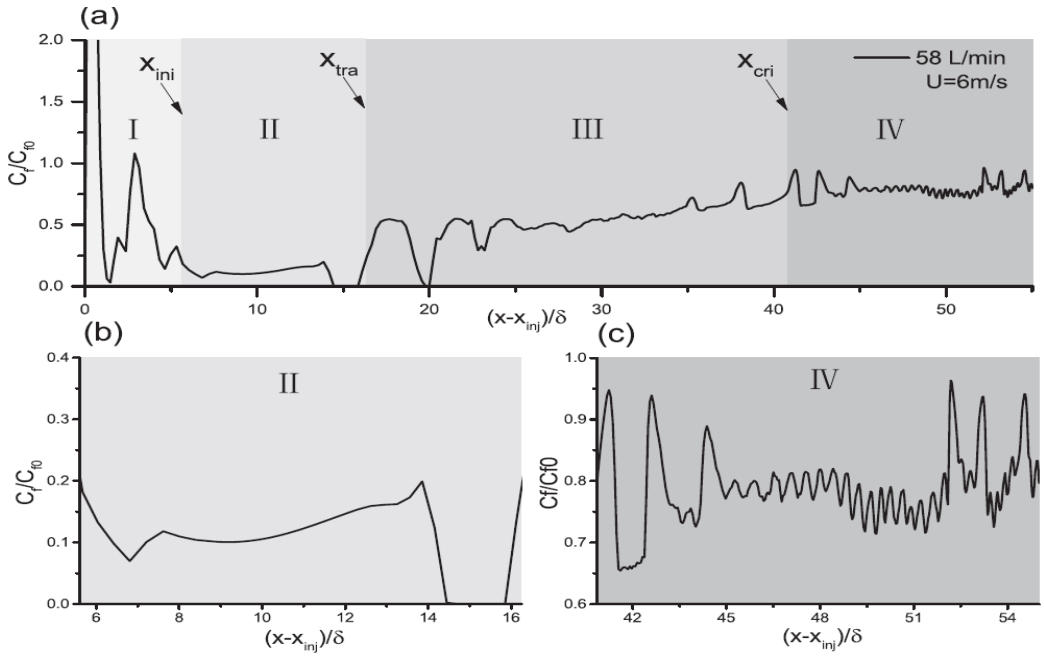

Figure 47: Close - Up of the Bubble Oscillations Effect on D.R. (Qin et al. *2017).*

This effect was also noticed in this research as can be seen in Figure 48. The oscillating behaviour was noted across all testing regimes. Whilst numerical oscillations do occur, they do not occur at the same frequency and range as below in Figure 48 . Hence the behaviour of these oscillations are due to the air bubbles moving around in the T.B.L An average of the last hundred seconds was taken as a reading. Whilst no validation was done using tank testing and experimental data in this study, comparing results and behavioural patterns with experimental data acted as a validation. This gives confidence in the CFD model as it managed to capture such a tricky behaviour that was captured in experimental laboratory testing.

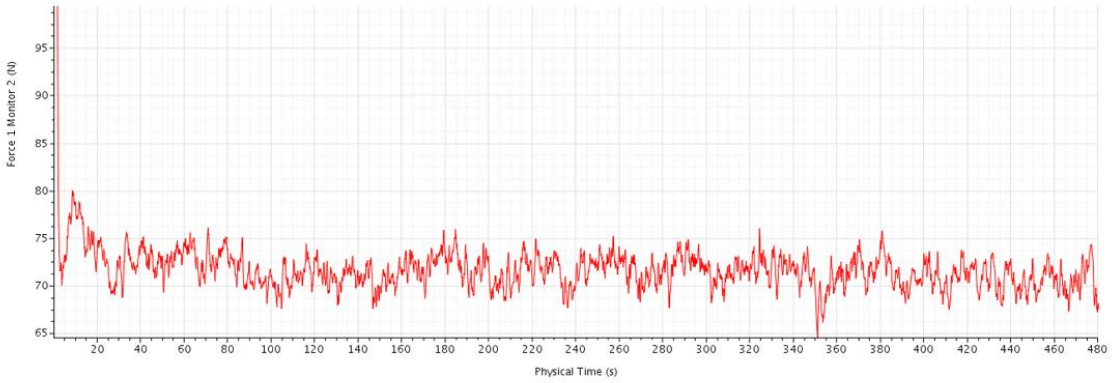

Figure 48: D.R. Across Modelled Plate with Oscillations

4.6.2.2 *Air Capture and Behaviour in the Boundary Layer*

Figure 50 is an example of how air moved around the plate, it can be noted that the air dispersed more and more away from the injection point. It is also noted that wherever the air does not have a VOF of 1 then this is a bubble.

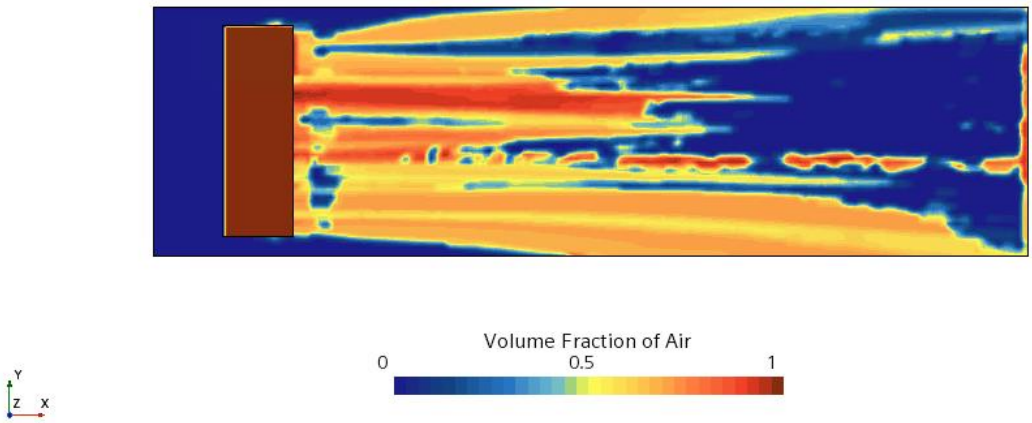

Figure 50: Air on Bottom of a Plate

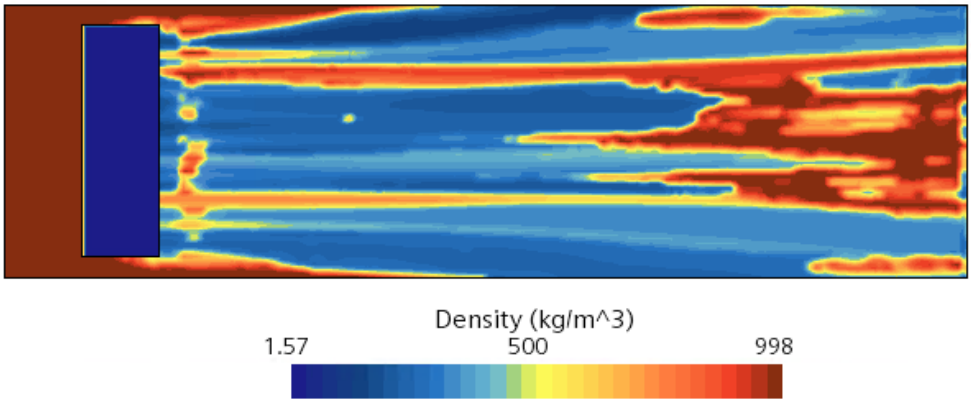

Figure 49: Density Across a Flat Plate

Figure 49 shows the density across the flat plate, as in Figure 50. Again, the mixture of air and water can be noticed as bubbles whilst the dark blue and dark red is purely air or water.

The behaviour of the bubble dispersion also replicates the behaviour of experimental works done Zhao *et al.* (2022) by as can be seen in Figure 51. The bubbles here have a haphazard movement and there is not a full carpet, but instead a random dispersion, this was also observed in this thesis . Zhao *et al.* (2022) states that this is a function of

the velocity inside the T.B.L. The replication of the bubbly flow behaviour is also another validation for the CFD model.

It can be noted that in Figure 52 the bubbles do not touch the flat plate, as mentioned in the literature previously and as can be seen in Figure 10 and Figure 9. This was noted across all models in same plate testing, Re, testing and scaling up testing. This further confirms the robustness of the CFD model and its ability to replicate the behaviour of air water interaction behaviour from experimental results.

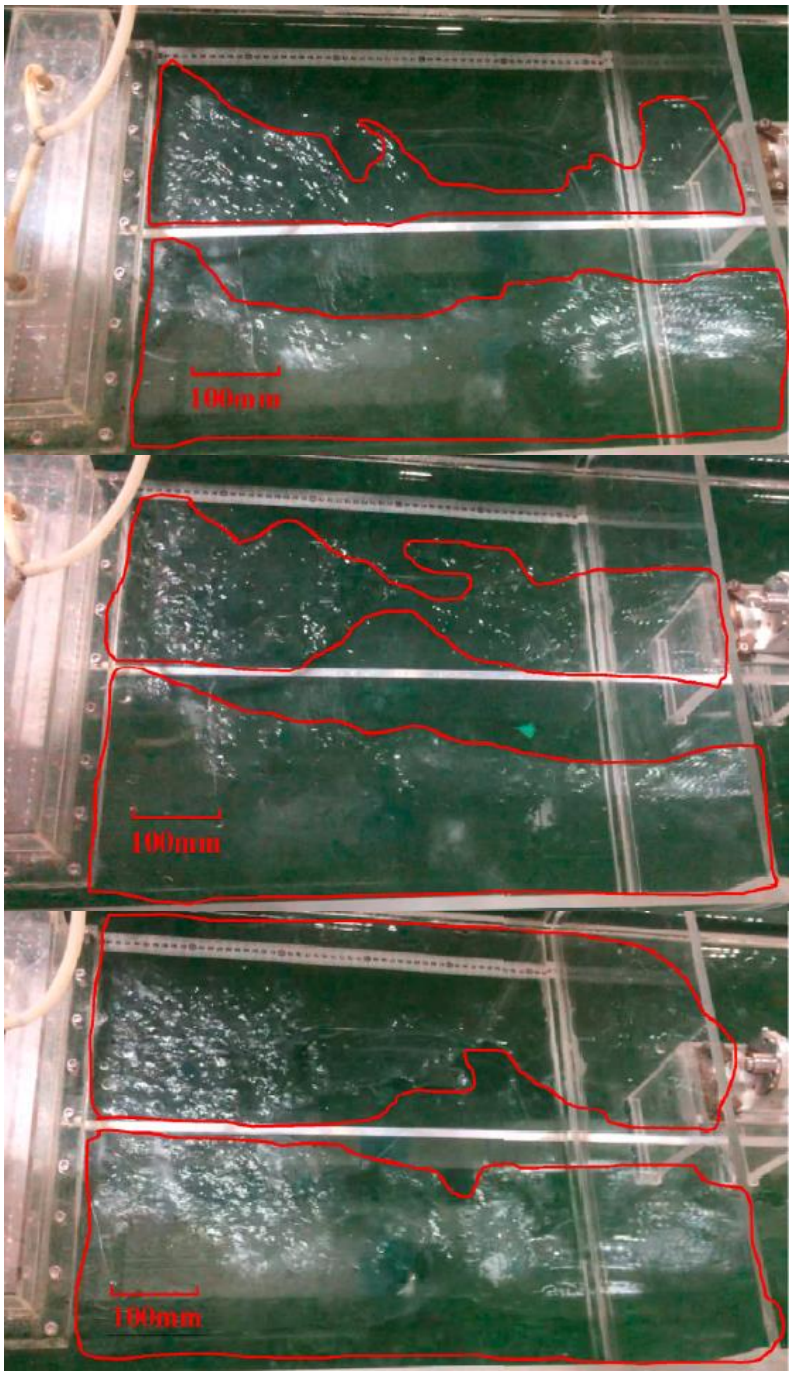

Figure 51: Air Behaviour in Experimental Work (Zhao et al. *2022)*

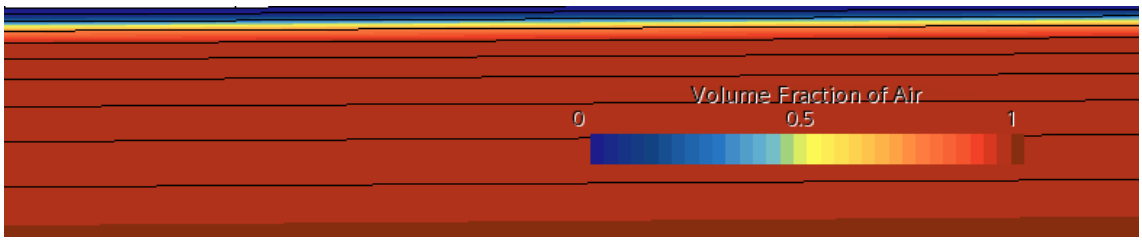

Figure 52: Liquid Layer at the Wall of the Plate Replicated by CFD

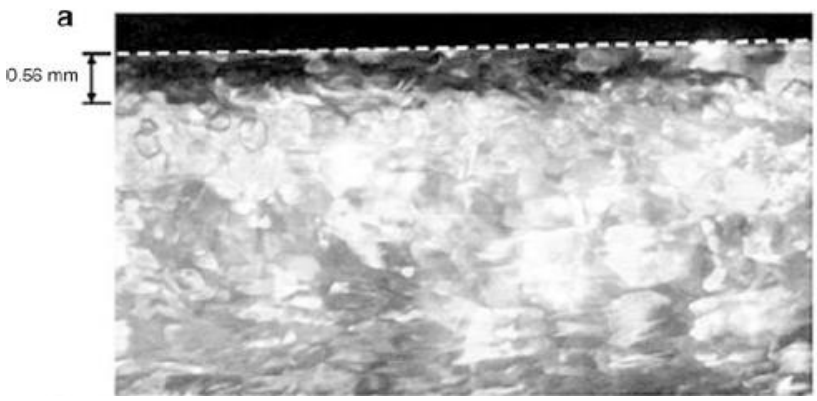

Figure 53: Observing the Liquid Layer (Elbing et al. 2008)

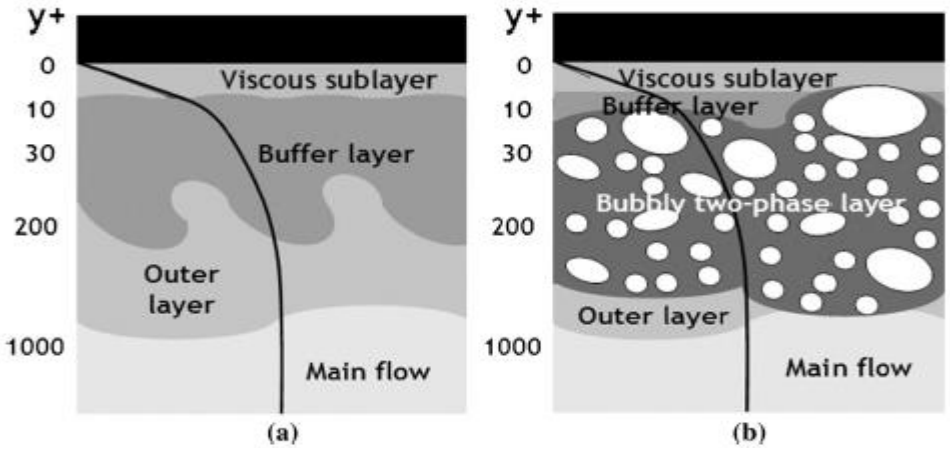

Figure 54: Boundary Layer with and Without Air Injection (Elbing et al. 2008)

In Figure 55 and Figure 56, the swirling motion of air escaping the B.L. was captured, which is also known as a mushroom cap. This mushroom cap shape is formed when a rising fluid, in this case air, encounters turbulent eddies. The turbulent eddies cause the

air plume to spread out and mix, which creates the mushroom cap shape. The shape is dependent on speed, direction, and properties of the fluid (Kumar *et al.* (2021)). It can be noted in Figure 55 that for the same injection rate, but a smaller Fr number, hence less turbulence the mushroom cap, is less defined. This could also be due to the fact the higher the turbulence the more air is sucked out of the T.B.L. (Pavlov *et al.* (2020)). This further strengthens the argument that turbulence plays a large part in drag reduction when injecting air.

It is understood that at the edge of a free edge in a stream, vortices will be created, hence the mushroom shape captured. This motion was captured due to having a refined mesh and a correct CFD set-up. This phenomenon was also captured for lower injection rates as can be seen in Figure 57.

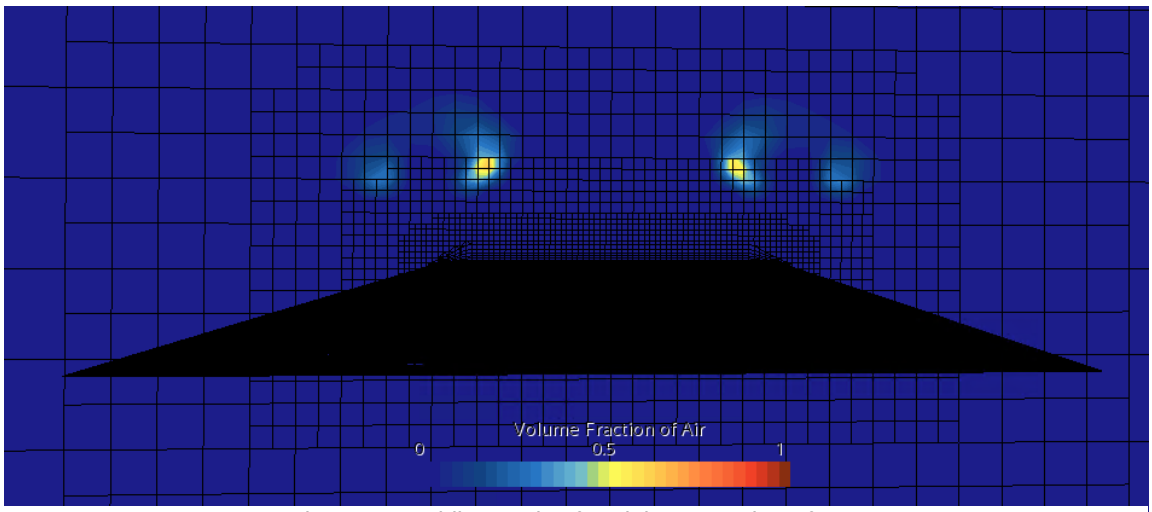

Figure 55: Swirling Motion for Alpha 0.9 and Fr of 0.31

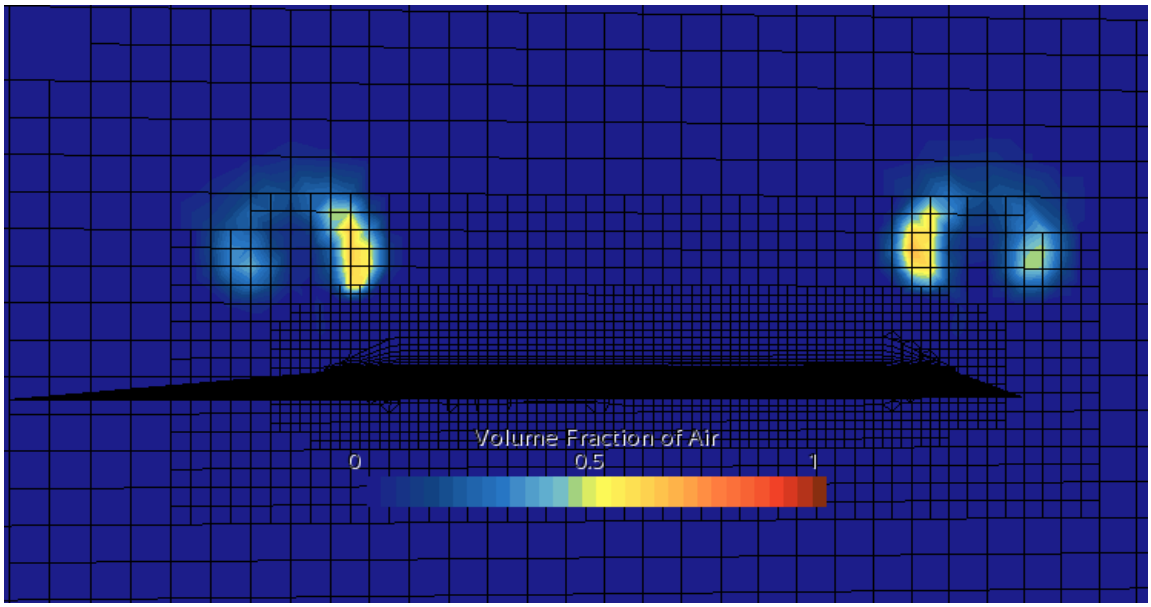

Figure 56: Swirling Motion for Alpha 0.9 and Fr of 0.42

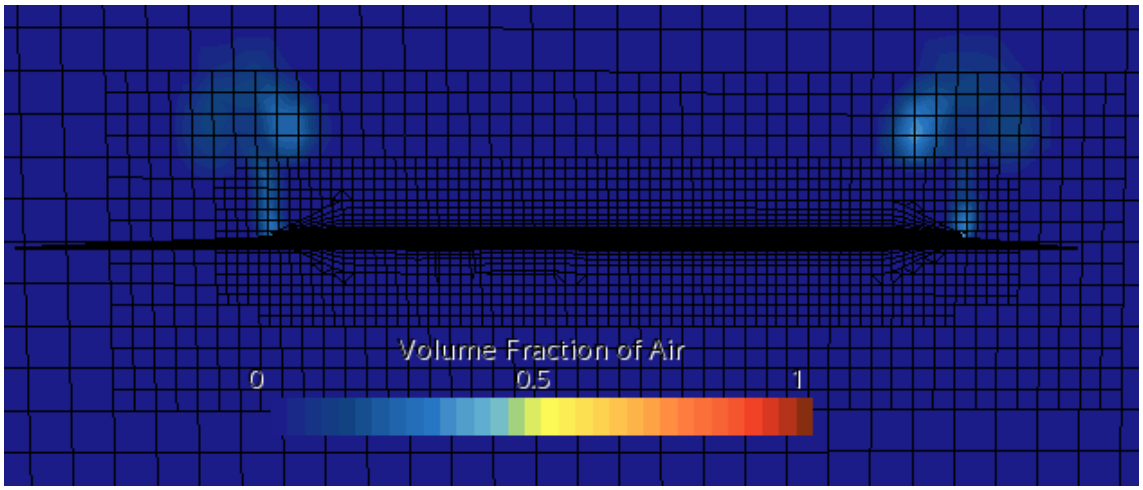

Figure 57: Swirling Motion for Alpha 0.4 and Fr of 0.42

4.7 Conclusion

The main objective in this chapter was to undertake several simulations to understand how the scaling up drag reduction from air lubrication systems could be done using CFD, analyse these results and deduce a mathematical equation that can be used for predicting drag results.

- Same plate testing was done at a maximum depth of 6.5 m as half of the global fleet has a draught of less than 6. It was observed that hydrostatic pressure affected the final drag reduction result significantly. This was only possible by including compressibility into the CFD model. Research on compressibility on drag reduction is only limited with only three studies being available at the time of writing (Lo *et al.* (2006)), (Kazuyasu *et al.* (2002) and(Van Den Berg *et al.* (2005)).
- The mixing ratios of 0.4 – 0.6 offer the best D.R. result across all hydrostatic depths.
- It was noticed that the there is an almost linear relationship with depth when keeping all other variables, such as Re, constant. This methodology could be used to model a plate at full size at 0.5m depth and its drag reduction at different operating drafts of a ship. This would save computational time drastically.

- A mathematical model that could be used to predict the reduction across different depths, injection rates and velocities was developed using the Pi-Buckingham theorem

$$F = [(V * L * \mu) * (m^{\cdot} * V) * (H * L)].$$

- The decision to separate the Reynolds number from hydrostatic pressure was confirmed with the use of the equation developed. Results from the Re testing showed that the higher the Re the less the D.R. effect.
- Using the MFR non-dimensionless value versus drag reduction for same size plate testing resulted in a good agreement with an R squared value > 0.86 and an r value > -0.926. This strengthened the argument that there exists an almost linear relation between drag reduction and hydrostatic pressure, but the variance comes from turbulence within the T.B.L. coming from different injection rates.
- Re testing up to $\mathrm{Re}\ x10^9$ was done with the inclusion of compressibility. It was concluded that an increase in Re decreases the drag reduction effect.
- The importance of a well-defined mesh was highlighted with the capture of the mushroom cap effect and a very low wall y+.
- A scaling test was done, the agreement was more than 84 %. The difference is believed to for to several reasons such as increase in turbulence, difference in bubble size and an increase in Re number. When introducing a change in these variables the relationship is not linear.
- It was noted that when scaling up modes, both the MFR and the injection area should be scaled up. It is also thought that when scaling up it would be better to scale up the mixing ratio instead of the bubble size.
- This non-linearity is believed to come from turbulence production and difference in bubble dynamics from model to full size. The effect of turbulence production and its effect on the T.B.L. was noted by the mushroom cap effect.
- The robustness of the CFD model was validated by comparing the behaviour of the bubbles against the literature from (Elbing *et al.* (2008)), (Qin *et al.* (2017)), (Adrian, 2007) and (Zong *et al.* (2022)).

4.7.1 Limitation of This Research

- Although vast progress has been made in the last 20 years to capture MBDR there are still many assumptions in the development of mathematical or numerical models that represent processes. As a result, the validation of these numerical models developed is still necessary (Sindagi *et al.* (2020)).
- In computational fluid dynamics (CFD), it is impossible to numerically simulate turbulence without discretizing the flow-field as far as the Kolmogorov microscales, which can be done by DNS. Most research on DNS is done on low Re numbers, which is not relevant to marine simulations. Because DNS simulations are exorbitantly expensive due to memory, computational and storage overheads, turbulence models are used to simulate the effects of turbulence.
- No experimental testing was done, so a full validation of the methodology and CFD model developed could not be done.
- Whilst research is done on smaller plates or numerically it is difficult to compare this work with any technologies in the current market as their air release differ with some relying on external factors such as the K-H instabilities phenomenon.

5 Conclusion

This study aimed to give a better understanding of air lubrication systems. This was done by optimizing the injection rates, studying the effect of hydrostatic pressure, the effect of Re and finally scaling up the models. Before this study, research on scaling methods was very limited and it was agreed that no scaling law exists (Park *et al.* (2017)) and (Qin *et al.* (2017)). CFD was used to understand this relationship and this decision was in agreement with the comments of "*The Specialist Committee on Energy Saving Methods"* (ITTC, 2021).

Only a partial validation of this work was undertaken given that an experimental test has not yet been performed. Nonetheless, some patterns and results were compared to experimental data and there was a good agreement.

Whilst a good agreement was achieved when scaling up the plate from model size to full size, a full understanding of ALS drag reduction is still not understood. Therefore, the following are several research ideas and theories on what physical factors affect bubble drag reduction:

- A study on the void fraction of volume of fluid. Research shows that an optimum injection rate exists. Once past this point, excessive microbubble injection destroys the favourable turbulent B.L. leading to a loss of the drag reduction effect.
- Reducing the density of gas injected increases the drag reduction.
- Turbulence suppression from the bubbles inside the T.B.L.
- Reynold's Stress breakdown due to bubbles
- Effect of compressibility and deformation of the bubble on the flow
- Bubble-bubble interaction and bubble splitting affect the eddy distribution and properties
- Bubble size, shape, and relative position of bubbles from the wall.

5.1 Findings and Contribution to Knowledge

With the knowledge created during this research, an ALS provider can use this methodology to scale up their tests from towing tanks or cavitation tunnels and give a

more accurate prediction to ship owners before they can invest in that particular technology. This will lead the ship owner to have more confidence in the predicted results and it can also be sued to structure a better contract that is based on performance guarantee.

5.1.1 CFD Practice

To obtain accurate and reliable results a robust CFD model had to be developed. The following are findings and comments developed throughout this research project:

- The importance of compressibility modelling was understood due the effect of hydrostatic pressure was observed, and a linear relationship between drag reduction effect decrease and hydrostatic depth was developed.
- Correcting the mass flow rate due to compressibility showed to be a correct method when scaling up flow rates w.r.t depth This was made possible by including compressibility into the CFD model.
- The importance of a well-defined mesh with a very low wall y+ was highlighted with the capture of the mushroom cap effect, bubble behaviour on the plate and the bubble location in the T.B.L.
- A small timestep was used as recommended by ITTC in turbulent flows, this made the simulation converge.
- A study was done on the most efficient boundary conditions to reduce simulation time. The result, using the inlet condition for all boundaries, made the simulation faster.
- The $k-\omega\ SST$ model was found to be the best turbulence model as it has superior capabilities for separating flows and air injection.
- Testing of different high Re with a compressibility was the first numerical testing of its kind for ALS.
- It was noticed that scaling the base size with the same scaling factor of the model gave an accurate base size.
- A CFD technique that can be used as a scaling law procedure.

Through this CFD practice two objectives were achieved that of:

1. Creating a CFD scaling technique

2. Developing knowledge on how to model ALS with CFD and capturing different behaviours.

5.1.2 Computational Results

Although ALS is not fully understood from this research the following findings have been discovered.

- An ideal injection rate was determined, whilst this behaved like in literature it was discovered that this mixing ratio could be applied to different hydrostatic pressure, different velocities and still give optimal results. It is recommended that for ALS a mixing ratio between 0.4 – 0.6 alpha to be used for all operating conditions.
- It can be recommended that when designing ALS the mixing ratio is more important than bubble sizing as bubbles have to many variables. This also indicates that there is a relationship between boundary layer thickness of water and thickness of air injected.
- An almost linear relationship between hydrostatic pressure and loss of drag reduction effect was observed in the same size plate testing. This observation could be used to model a plate at full size at 0.5m depth and its drag reduction at different operating drafts of a ship. This would save computational time drastically.
- A mathematical model that could be used to predict the drag reduction across different depths, injection rates and velocities was developed using the Pi-Buckingham theorem. Whilst this equation is not fully accurate as some other terms are missing it is a good starting point. This equation led to a development of a non-dimensionless parameter sigma which encapsulated the MFR.
- When plotting sigma against DR an accurate, almost linear prediction model for any depth and Fr was plotted with an R squared value > 0.86 and an r value > -0.926.
- The decision to separate the Reynolds number from hydrostatic pressure was confirmed with the use of the equation developed. Results from the Re testing showed that the higher the Re the less the D.R. effect.

- Re testing at Re $x10^9$ was done with the addition of compressibility which is thought to be the first of its kind. With this simulation a better understanding of how high Re and compressibility effect D.R across different injection rates.
- It was noticed that when increasing the Re using a higher alpha would give a more stable drag reduction over all.
- A scaling test was done, the agreement was more than 84 %. The difference is believed to be for several reasons such as increase in turbulence, difference in bubble size and an increase in Re number. When introducing a change in these variables the relationship is not linear.
- When scaling up models both the MFR and the injection area should be scaled up.
- This non-linearity is believed to come from turbulence production and difference in bubble dynamics from model to full size. The effect of turbulence production and its effect on the T.B.L. was noted by the mushroom cap effect.
- The robustness of the CFD model was validated by comparing the behaviour of the model against the literature from (Elbing *et al.* (2008)), (Qin *et al.* (2017)), (Adrian, 2007), (Madavan *et al.* (1984)), (Zong *et al.* (2022)) and (Hussan *et al.* (2008)).

Throughout this CFD practice the following objectives were achieved that of:

1. To understand how hydrostatic depth and operating conditions effects the drag reduction effect of ALS
2. To create a mathematical and scaling technique
3. To create a predictive model
4. To give insight on how scaling practices should be done
5. To develop knowledge on how to model ALS with CFD and capturing different behaviours

Therefore, this thesis has achieved the aims set out in the beginning.

5.2 Future Work

Despite the in-depth study of this research this area of is still under-explored due to several factors. CFD testing is very expensive as well as tow tank and cavitation tunnel

testing. Whilst industry players are involved in research and design (R&D), their main goal is fulfilling orders or increasing efficiency by a few percentage points and employing these findings quickly. Nonetheless the researcher has highlighted several suggestions and research ideas that could be used to further understand, develop, and optimise ALS systems.

- Replicate the methodology in a laboratory set-up to validate and verify all data.
- Expand the testing regime to include more Fr, depths, surface roughness and injection rates. This will then feed into the current data to create a correction factor.
- Expand the testing to include data on density, wall shear and VOF persistence downstream.
- Full extrapolation on KCS/ JBC tankers.
- Undertake calm and rough weather simulations.
- Use different multiphase models such as Eularian-Eularian and include the population balance model.
- Deeper statistical analysis of more variables.
- Examine the viscous effect of drag reduction by understanding the density and dynamic viscosity reduction.
- Use compressor and power curves to understand the added energy needed at different injection rates.
- Validate and expand the dimensional analysis to include more variables such that the scaling law will be fully understood.
- Develop a mathematical method that includes other ship factors such as form factor.
- Expand the mathematical model to include the Rayleigh-Plesset equation to monitor size of bubble with respect to time.
- Add field functions to Star-CCM+ to measure the bubble diameter (Kinzel *et al.* (2017)) . This would give a better understanding of persistence of drag reduction and bubble breakdown.
- Undergo a span-wise study on the D.R. effect.
- Undergo a density ratio study at different depths to determine any correlation that exists.

- Understand the acoustic effect of ALS for the benefit of noise reduction
- A study on using replenishment as a tool to keep the D.R. downstream constant
- Study the relationship of boundary layer thickness to injection rate and how this could scale up

References

(ARI), A.P.R.I. (2021) *Prospero*. Available at: https://www.astro.ljmu.ac.uk/prospero/docs/prospero/welcome/.

Adrian, R.J. (2007) 'Hairpin vortex organization in wall turbulencea', *Physics of Fluids*, 19(4). doi:10.1063/1.2717527.

American Bureau of Shipping (2019) 'Air Lubrication Technology', pp. 1–15.

Angus Gray-Stephens, Tahsin Tezdogan, S. day (2019) 'STRATEGIES TO MINIMISE NUMERICAL VENTILATION IN CFD SIMULATIONS OF HIGH-SPEED PLANING HULLS', in *ASME 2019 38th International Conference on Ocean, Offshore and Arctic Engineering*, pp. 1–10.

Avci, A.G. and Barlas, B. (2018) 'An experimental and numerical study of a high speed planing craft with full-scale validation', *Journal of Marine Science and Technology (Taiwan)*, 26(5), pp. 617–628. doi:10.6119/JMST.201810_26(5).0001.

Banks, J., Phillips, A.B. and Turnock, S.R. (2010) 'Free surface CFD prediction of components of Ship Resistance for KCS', in *13th Numerical Towing Tank Symposium*. Duisberg Germany.

Van Den Berg, T.H. *et al.* (2005) 'Drag reduction in bubbly Taylor-Couette turbulence', *Physical Review Letters*, 94(4), pp. 4–7. doi:10.1103/PhysRevLett.94.044501.

Böhm, C. and Graf, K. (2014) 'Advancements in free surface RANSE simulations for sailing yacht applications', *Ocean Engineering*, 90, pp. 11–20. doi:10.1016/j.oceaneng.2014.06.038.

Brizzolara, S. and F.S. (2014) 'ACCURACY OF CFD CODES IN THE PREDICTION OF PLANING SURFACES HYDRODYAMIC CHARACTERISTICS', (June 2007).

Calavia, J.R. (2016) 'Discretization Error Estimation and Mesh Optimization for Plasma Edge Transport Simulations of Nuclear Fusion Tokamaks'. Available at: http://oa.upm.es/44743/.

Carrica, P.M. *et al.* (1999) 'A polydisperse model for bubbly two-phase flow around a surface ship', *International Journal of Multiphase Flow*, 25(2), pp. 257–305.

doi:10.1016/S0301-9322(98)00047-0.

Ceccio, S.L. (2010) 'Friction drag reduction of external flows with bubble and gas injection', *Annual Review of Fluid Mechanics*, 42, pp. 183–203. doi:10.1146/annurev-fluid-121108-145504.

Ceccio, S.L. and Mäkiharju, S.A. (2012) *Air Lubrication Drag reduction on Great Lakes Ships Final Report*.

Ceccio, S.L., Perlin, M. and Elbing, B.R. (2010) 'A cost-benefit analysis for air layer drag reduction', *International Conference on Ship Drag Reduction*, (May), pp. 20–21.

Cimbala, Y.C.J. (2014) *Fluid Mechanics: Fundamentals and Applications*.

Cucinotta, F. *et al.* (2018) 'Numerical and experimental investigation of a planing Air Cavity Ship and its air layer evolution', *Ocean Engineering*, 152(January), pp. 130–144. doi:10.1016/j.oceaneng.2018.01.071.

Deutsch, S, Moeny, M. Fontainer, A.P. (2003) 'Microbubble drag reduction in rough walled turbulent boundary layers', in *ASME-JSME Fed*, pp. 1–9.

DNV (2021) *The webinar presenters on EEXI*.

DNV (2022) *CII- Carbon Intensity Indicator*. Available at: https://www.dnv.com/maritime/insights/topics/CII-carbon-intensity-indicator/implementation.html.

Dogrul, Ali , YASEMİN ARIKAN, F.Ç. (2010) 'A numerical investigation of air lubrication effect on ship resistance', in *INTERNATIONAL CONFERENCE ON SHIP DRAG REDUCTION (SMOOTH-Ships)*.

Ebrahimi, A. (2012) 'Numerical Study on Resistance of a Bulk Carrier Vessel Using CFD Method', *Journal of the Persian Gulf*, 3(10), pp. 1–6.

EJ Foeth, R Eggers, I van der Hout, F.Q. (2009) *Reduction of Frictional Resistance by Air Bubble Lubrication*. Wageningen Netherlands.

Elbing, B.R. *et al.* (2008) 'Bubble-induced skin-friction drag reduction and the abrupt transition to air-layer drag reduction', *Journal of Fluid Mechanics*, 612(May 2014), pp. 201–236. doi:10.1017/S0022112008003029.

Elbing, B.R. *et al.* (2013) 'On the scaling of air layer drag reduction', *Journal of Fluid Mechanics*, 717, pp. 484–513. doi:10.1017/jfm.2012.588.

Faison, L.A. (2014) *Design of a High Speed Planing hull with a Cambered Step and Surface Piercing Hydrofoils*.

Feng, Y.Y. *et al.* (2020) 'Microbubble effect on friction drag reduction in a turbulent boundary layer', *Ocean Engineering*, 211(June), p. 107583. doi:10.1016/j.oceaneng.2020.107583.

Ferrante, A. and Elghobashi, S. (2004) 'On the physical mechanisms of drag reduction in a spatially developing turbulent boundary layer laden with microbubbles', *Journal of Fluid Mechanics*, 503(503), pp. 345–355. doi:10.1017/S0022112004007943.

Foeth, E.J., Eggers, R. and H.. (2009) 'Reduction of frictional resistance by air bubble lubrication', in *SNAME Annual Meeting*.

Frisk, D. and Tegehall, L. (2015) *Prediction of High-Speed Planing Hull Resistance and Running Attitude*.

Gao, Q. *et al.* (2023) 'Experimental study on bubble drag reduction by the turbulence suppression in bubble flow', *Ocean Engineering*, 272(February), p. 113804. doi:10.1016/j.oceaneng.2023.113804.

Gel, A. *et al.* (2013) 'Validation and uncertainty quantification of a multiphase computational fluid dynamics model', *Industrial and Engineering Chemistry Research*, 52(33), pp. 11424–11435. doi:10.1021/ie303469f.

Ghassemi, H. *et al.* (2015) 'A HYDRODYNAMIC METHODOLOGY AND CFD ANALYSIS FOR', *Polish Maritime Research*, 22(2), pp. 23–31.

Goolcharan, J.D. (2016) *Computational Fluid Dynamic analysis of Microbubble Drag Reduction Systems at High Reynolds Number*. doi:10.25148/etd.FIDC000788.

H.Miyata, A.K.& (2001) 'A.Kanai & H.Miyata', *International Journal of Meth Fluids*, 35, p. 593.

H.Schlichting (1968) *Boundary-Layer Theory*. 6th editio. McGraw-Hill.

H K Versteeg, W.M. (2007) *An Introduction to Computational Fluid Dynamics The Finite*

Volume Method. 2nd edn. Pearson Education Limited.

Hao, W.U. and Yongpeng, O.U. (2019) 'Numerical simulation of air layer morphology on flat bottom plate with air cavity and evaluation of the drag reduction effect', *International Journal of Naval Architecture and Ocean Engineering*, 11(1), pp. 510–520. doi:10.1016/j.ijnaoe.2018.09.005.

Hara, K., Suzuki, T. and Yamamoto, F. (2011) 'Image analysis applied to study on frictional-drag reduction by electrolytic microbubbles in a turbulent channel flow', *Experiments in Fluids*, 50(3), pp. 715–727. doi:10.1007/s00348-010-0970-5.

Harleman, M.J.. (2012) 'On the effect of turbulence on bubbles: experiments and numercal simulations of bubbles in wall-bounded flows', p. Ph.D. Thesis, TU Delft, The Netherlands.

Hashim, A., Yaakob, O B, *et al.* (2015) 'Review of Micro-bubble Ship Resistance Reduction Methods and the Mechanisms that Affect the Skin Friction on Drag Reduction from 1999 to 2015', *Jurnal Teknologi*, 74(5), pp. 105–114.

Hashim, A., Yaakob, O. B., *et al.* (2015) 'Review of micro-bubble ship resistance reduction methods and the mechanisms that affect the skin friction on drag reduction from 1999 to2015', *Jurnal Teknologi*, 74(5), pp. 105–114. doi:10.11113/jt.v74.4650.

Hassan, Y A, C.C.G.-T. (2006) 'INVESTIGATION OF DRAG REDUCTION MECHANISM BY MICROBUBBLE INJECTION WITHIN A CHANNEL BOUNDARY LAYER USING PARTICLE TRACKING VELOCIMETRY', *Nuclear Engineering and Technology*, 38(8), pp. 763–778.

Hinze, J.O. (1955) 'Fundamentals of the hydrodynamic mechanism of splitting in dispersion processes', *AIChE Journal*, 1(3), pp. 289–295. doi:10.1002/aic.690010303.

Hoang, C.L., Toda, Y. and Sanada, Y. (2009) 'Full scale experiment for frictional resistance reduction using air lubrication method', *Proceedings of the Ninteteenth International Offshore and Polar Engineering Conference*, pp. 812–817.

HSVA (1990) *HYKAT*. Available at: https://www.hsva.de/facilities/hykat.html (Accessed: 15 June 2020).

Huang, Z. *et al.* (2016) 'Optimal annual net income of a containership using CO 2 reduction measures under a marine emissions trading scheme Optimal annual net

income of a containership using CO 2 reduction measures under a marine emissions trading scheme', *The International Journal of Transportation Research*, 7(April), pp. 24–34. doi:10.1179/1942787514Y.0000000030.

ICCT Transportation, T.I.C. of C. (2017) *GREENHOUSE GAS EMISSIONS FROM GLOBAL SHIPPING , 2013 – 2015*. Washington.

IMO (2011) *Energy Efficiency Measures*, *Energy Efficiency Measures*. Available at: http://www.imo.org/en/ourwork/environment/pollutionprevention/airpollution/pages/technical-and-operational-measures.aspx (Accessed: 22 July 2019).

IMO (2014) *Third IMO GHG Study*.

IMO (2018) 'INITIAL IMO STRATEGY ON REDUCTION OF GHG EMISSIONS FROM SHIPS', pp. 1–11.

Industries, M.H. (2012) *MHI Installs MALS (Mitsubishi Air Lubrication System) on a Ferry For First Time and Verifies Over 5% Fuel Efficiency Improvement*.

ITTC (2011) *Practical Guidelines for Ship CFD Applications*, *Recommended Procedures and Guidelines Practical Guidelines for Ship CFD. In: Proceedings of the 26th ITTC.*

ITTC (2021) 'The Specialist Committee on Energy Saving Methods: Final Report and Recommendations to the 29th ITTC', *Proceedings of the ITTC 2021* [Preprint]. Available at: https://ittc.info/media/9100/sc-energy-saving-methods.pdf.

J. Busch , W. Barthlott , M. Brede, W.T. and M.M. (2019) 'Bionics and green technology in maritime shipping : an assessment of the effect of Salvinia air-layer hull coatings for drag and fuel reduction', *Philosophical transactions of the Royal Society of London. Series A: Mathematical and physical sciences*, 377(2138). doi:10.1098/rsta.2018.0263.

J.s, M.J.S.. and U. (1989) 'Microbubble formulation and splitting in a turbulent boundary layer for turbulence reduction.', in *Advances in Fliuids Dynamics*, pp. 168–217.

Jacob, B. *et al.* (2010) 'Drag reduction by microbubbles in a turbulent boundary layer Drag reduction by microbubbles in a turbulent boundary layer', *PHYSICS OF FLUIDS*, 22(115104). doi:10.1063/1.3492463.

Jang, J. *et al.* (2014) 'Experimental investigation of frictional resistance reduction with

air layer on the hull bottom of a ship', *International Journal of Naval Architecture and Ocean Engineering*, 6(2), pp. 363–379. doi:10.2478/IJNAOE-2013-0185.

Jha, N.K., Bhatt, A. and Govardhan, R.N. (2019) 'Effect of bubble distribution on wall drag in turbulent channel flow', *Experiments in Fluids*, 60(8), pp. 1–18. doi:10.1007/s00348-019-2773-7.

Jiménez, J. and Pinelli, A. (1999) 'The autonomous cycle of near-wall turbulence', *Journal of Fluid Mechanics*, 389, pp. 335–359. doi:10.1017/S0022112099005066.

Kawakita, C., Sato, S. and Okimoto, T. (2015) 'Application of Simulation Technology to Mitsubishi Air Lubrication System', *Mitsubishi Heavy Industries Technical Review Vol. 52 No. 1 (March 2015)*, 52(1), pp. 50–56.

Kawamura, T. *et al.* (2003) 'Effect of bubble size on the microbubble drag reduction of a turbulent boundary layer', *Proceedings of the ASME/JSME Joint Fluids Engineering Conference*, 2 A, pp. 647–654. doi:10.1115/fedsm2003-45645.

Kawamura, T., Kakugawa, A. and Kodama, Y. (2002) 'Controlling the size of microbubbles for drag reduction', *3rd Symposium on Smart Control of Turbulence* [Preprint]. Available at: http://www.nmri.go.jp/turbulence/PDF/symposium/FY2001/Kawamura.pdf.

Kazuyasu, S., KAWAMURA, T. and TAKAGI, S. (2002) 'Numerical Simulations on Drag Reduction Mechanism by Microbubbles', *3rd Symposium on Smart Control of Turbulence* [Preprint]. Available at: http://www.turbulence-control.gr.jp/sympo_e/FY2001/.

Kinzel, M.P., Kunz, R.F. and Lindau, J.W. (2017) 'An assessment of CFD cavitation models using bubble growth theory and bubble transport modeling', *Open Archives of the 17th International Symposium on Transport Phenomena and Dynamics of Rotating Machinery, ISROMAC 2017*, pp. 0–11.

Kitagawa, A., Hishida, K. and Kodama, Y. (2005) 'Flow structure of microbubble-laden turbulent channel flow measured by PIV combined with the shadow image technique', *Experiments in Fluids*, 38(4), pp. 466–475. doi:10.1007/s00348-004-0926-8.

Kitagwa, A., Hishida, K. and K.Y. (2004) *Two phases turbulence structure in a micro*

bubble channel flow, *Proceedings of 5th Symp. on Smart Control of Turbulence. University of Tokyo*.

Kodama, Y., Kakugawa, A., Takahashi, T.,Nagaya, S.& Sugiyama, K. (2002) 'Microbubbles: drag reduction mechanism and applicability to ships', in *24th Symp. Naval Hydrodynamics*, pp. 1–19.

Kodama, Y . Kakugawa, A. Takahashi, T.K. (2000) 'experimental study on microbbubles and their applicability to ships for skin reduction', *International Journal Heat and Fluid Flow*, 21, pp. 582–588.

Kodama, Y. *et al.* (2000) 'Experimental study on microbubbles and their applicability to ships for skin friction reduction', *International Journal of Heat and Fluid Flow*, 21(5), pp. 582–588. doi:10.1016/S0142-727X(00)00048-5.

Kumagai, I., Takahashi, Y. and Murai, Y. (2015) 'Power-saving device for air bubble generation using a hydrofoil to reduce ship drag: Theory, experiments, and application to ships', *Ocean Engineering*, 95, pp. 183–194. doi:10.1016/j.oceaneng.2014.11.019.

Kumar, S., Huang, R.F. and Hsu, C.M. (2021) 'Effects of pulsation intensity on the flow and dispersion of pulsed dual plane jets', *International Journal of Mechanical Sciences*, 193(43), p. 106182. doi:10.1016/j.ijmecsci.2020.106182.

Kunz, R.F. *et al.* (2007) 'Validation of Two-Fluid Eulerian CFD Modeling for Microbubble Drag Reduction Across a Wide Range of Reynolds Numbers', *Journal of Fluids Engineering*, 129(January 2007), pp. 66–79. doi:10.1115/1.2375124.

Larsson L, Stern F, B. V (2003) 'Benchmarking of Computational Fluid Dynamics for Ship Flows: The Gothenburg 2000 Workshop.', *Journal of Ship Research*, 47(19), pp. 63–81.

Latorre, R. (1997) 'Ship hull drag reduction using bottom air injection', *Ocean Engineering*, 24(2), pp. 161–175. doi:10.1016/0029-8018(96)00005-4.

Legendre, D., Magnaudet, J. and Mougin, G. (2003) 'Hydrodynamic interactions between two spherical bubbles rising side by side in a viscous liquid', *Journal of Fluid Mechanics*, 497, pp. 133–166. doi:10.1017/S0022112003006463.

Legner, H.H. (1984) 'A simple model for gas bubble drag reduction', *Physics of Fluids*, 27(12), pp. 2788–2790. doi:10.1063/1.864592.

Lindstad, H., Asbjørnslett, B.E. and Strømman, A.H. (2011) 'Reductions in greenhouse gas emissions and cost by shipping at lower speeds', *Energy Policy*, 39(6), pp. 3456–3464. doi:10.1016/j.enpol.2011.03.044.

Lo, T.S., L'Vov, V.S. and Procaccia, I. (2006) 'Drag reduction by compressible bubbles', *Physical Review E - Statistical, Nonlinear, and Soft Matter Physics*, 73(3). doi:10.1103/PhysRevE.73.036308.

LTD, O.S.C. (2014) 'Energy Saving by air bubbles', in *Enviromental Technology Seminar*.

Lu, J., Fernández, A. and Tryggvason, G. (2005) 'The effect of bubbles on the wall drag in a turbulent channel flow', *Physics of Fluids*, 17(9), pp. 1–12. doi:10.1063/1.2033547.

Ma, J. *et al.* (2010) 'A quantitative sub-grid air entrainment model for bubbly flows - plunging jets', *Computers and Fluids*, 39(1), pp. 77–86. doi:10.1016/j.compfluid.2009.07.004.

Madavan K, Deutsch S, M.C. (1985) 'Numerical Investigations into the mechanisms of microbubble drag reduction', *Trans ASME*, 107, pp. 370–377.

Madavan, N.K., Deutsch, S. and Merkle, C.L. (1984) 'Reduction of turbulent skin friction by microbubbles', *Physics of Fluids*, 27(2), pp. 356–363. doi:10.1063/1.864620.

Mäkiharju, S.A., Perlin, M. and Ceccio, S.L. (2013) 'On the energy economics of air lubrication drag reduction', *Institure Journal of Naval Architecture and Ocea Engineering*, 4(4), pp. 412–422. doi:10.3744/JNAOE.2012.4.4.412.

Mancini, S., Dashtimanesh, A. and Bilandi, R.N. (2018) 'A Numerical Way for a Stepped Planing Hull Design and Optimization', *Technology and Science for the Ships of the Future*, (June), pp. 220–229. doi:10.3233/978-1-61499-870-9-220.

Mancini, S., Luca, F. De and Ramolini, A. (2017) 'Towards CFD guidelines for planing hull simulations based on the Naples Systematic Series', in *VII International Conference on Computational Methods in Marine Engineering*.

De Marco, A. *et al.* (2017) 'Experimental and numerical hydrodynamic analysis of a stepped planing hull', *Applied Ocean Research*, 64, pp. 135–154. doi:10.1016/j.apor.2017.02.004.

MARIN (2011) 'The efficacy of air-bubble lubrication for decreasing friction resistance',

The Naval Architect, (APRIL), pp. 44–46.

McCormick, M.E. and B.R. (1973) 'Drag Reduction of a submersible hull by electrolysis', *Naval Engineers Journal*, 85(2), pp. 11–16.

Merkle, C. L. and Deutsch, S. (1990) 'Drag Reduction in liquid boundary layers by gas injection', in *The Smithsonian/NASA Astrophysics Data System*, pp. 351–412. doi:10.2514/4.865978.

Mohanarangam, K. *et al.* (2009) 'Numerical simulation of micro-bubble drag reduction using population balance model', *Ocean Engineering*, 36(11), pp. 863–872. doi:10.1016/j.oceaneng.2009.05.001.

Møller, M.M. and Carbon, Z. (2022) *Are shipowners committed to a net zero future?*

Montazeri, M.H. and Alishahi, M.M. (2019) 'An efficient method for numerical modeling of thin air layer drag reduction on flat plate and prediction of flow instabilities', *Ocean Engineering*, 179(October 2018), pp. 22–37. doi:10.1016/j.oceaneng.2019.03.016.

Moriguchi, Y. and Kato, H. (2002) 'Infuence of micro bubble diameter and distribution on frictional resistance reduction', *J.Mar.Sci.Technol.*, 7(2), pp. 79–85.

Murai, Y. (2014) 'Frictional drag reduction by bubble injection', *Experiments in Fluids*, 55(7). doi:10.1007/s00348-014-1773-x.

Nations, U. (2015) 'Paris Agreement', in *Adoption of the Paris Agreement*. Paris: United Nations, p. 3.

Oeffner, J. *et al.* (2020) 'From nature to green shipping: Assessing the economic and environmental potential of AIRCOAT on low-draught ships', 1, p. 10.

Park, S.H. and Lee, I. (2017) 'Optimization of drag reduction effect of air lubrication for a tanker model', *International Journal of Naval Architecture and Ocean Engineering*, 10(4), pp. 427–438. doi:10.1016/j.ijnaoe.2017.09.003.

Pavlov, G.A. *et al.* (2020) *Air Lubricated and Air Cavity Ships*, *Air Lubricated and Air Cavity Ships*. doi:10.1007/978-1-0716-0425-0.

Perret, M. and Carrica, P.M. (2015) 'Bubble-wall interaction and two-phase flow

parameters on a full-scale boat boundary layer', *International Journal of Multiphase Flow*, 73, pp. 289–308. doi:10.1016/j.ijmultiphaseflow.2015.03.013.

Pineda-Pérez, H. *et al.* (2018) 'CFD modeling of air and highly viscous liquid two-phase slug flow in horizontal pipes', *Chemical Engineering Research and Design*, 136, pp. 638–653. doi:10.1016/j.cherd.2018.06.023.

Qin, S., Chu, N., Yao, Y., Liu, J., Huang, B. and Wu, D. (2017) 'Stream-wise distribution of skin-friction drag reduction on a flat plate with bubble injection', *Physics of Fluids*, 29(3). doi:10.1063/1.4977800.

Qin, S., Chu, N., Yao, Y., Liu, J., Huang, B., Wu, D., *et al.* (2017) 'Stream-wise distribution of skin-friction drag reduction on a flat plate with bubble injection', *PHYSICS OF FLUIDS*, 29(037103). doi:10.1063/1.4977800.

Qin, S.D.W. (2017) 'Experimental and Numerical Study of Bubble Drag Reduction on a Flat Plate', in *Proceedings of the ASME 2017 Fluids Engineering Division Summer Meeting*, pp. 1–11.

Roache, P.J. (1997) 'QUANTIFICATION OF UNCERTAINTY IN COMPUTATIONAL FLUID DYNAMICS'.

Sanada, T. *et al.* (2009) 'Motion and coalescence of a pair of bubbles rising side by side', *Chemical Engineering Science*, 64(11), pp. 2659–2671. doi:10.1016/j.ces.2009.02.042.

Sayyaadi, H. and Nematollahi, M. (2013) 'Determination of optimum injection flow rate to achieve maximum micro bubble drag reduction in ships; An experimental approach', *Scientia Iranica*, 20(3), pp. 535–541. doi:10.1016/j.scient.2013.05.001.

Sayyaadi, H and Nematollahi, M. (2013) 'Sharif University of Technology Determination of optimum injection flow rate to achieve maximum micro bubble drag reduction in ships ; an experimental approach', *Scientia Iranica*, 20(3), pp. 535–541. doi:10.1016/j.scient.2013.05.001.

Sharifi, Y., Ghassemi, H. and Zanganeh, H. (2017) 'Various Innovative Technologic Devices in Shipping Energy Saving and Diminish Fuel Consumption', *International Journal of Physics*, 5(1), pp. 21–29. doi:10.12691/ijp-5-1-4.

Shereena, S.G. *et al.* (2014) 'CFD Study of Drag Reduction in Axisymmetric Underwater Vehicles using Air Jets', *Engineering application of Computational Fluid Mechanics*, 7(2), pp. 193–209. doi:10.1080/19942060.2013.11015464.

Siemens (2019) 'Prism Layer Meshing for Effective Boundary Layer Capturing Agenda ':, (December).

SilverStream (2019) *Case Studies*.

Simman (2008) *MOERI Container Ship (KCS)*. Available at: http://www.simman2008.dk/KCS/container.html.

Sindagi, S. *et al.* (2019) *Numerical investigation of influence of microbubble injection, distribution, void fraction and flow speed on frictional drag reduction*, *Lecture Notes in Civil Engineering*. Springer Singapore. doi:10.1007/978-981-13-3119-0_17.

Sindagi, S. and Vijayakumar, R. (2020) 'Succinct review of MBDR/BDR technique in reducing ship's drag', *Ships and Offshore Structures*, 0(0), pp. 1–12. doi:10.1080/17445302.2020.1790296.

Sindagi, S., Vijayakumar, R. and Saxena, B.K. (2019) 'Parametric CFD investigation of ALS technique on reduction in drag of bulk carrier', *Ships and Offshore Structures*, 0(0), pp. 1–14. doi:10.1080/17445302.2019.1661617.

Skudarnov, P. V. and Lin, C.X. (2005) 'Density ratio and turbulence intensity effects in microbubble drag reduction phenomenon', *Proceedings of 2005 ASME Fluids Engineering Division Summer Meeting, FEDSM2005*, 2005, pp. 181–186. doi:10.1115/FEDSM2005-77075.

Sochacki, J.S. (2013) *Introduction to Compressible Computational Fluid Dynamics*. Available at: http://www.plumbingmart.com/water-hammer-information.html.

Stephani, K.A. *et al.* (2006) 'Drag Reduction using Trapped Bubbles on a Flat Plate Surface', in *American Institute of Aeronautics and Astronautics*, pp. 1–19.

Stern, F. *et al.* (1999) 'Verification and validation of CFD simulations', *Proceedings of the 1999 3rd ASME/JSME Joint Fluids Engineering Conference, FEDSM'99, San Francisco, California, USA, 18-23 July 1999 (CD-ROM)*, (407), p. 1.

Syamlal, M., Celik, I.B. and Benyahia, S. (2017) 'Quantifying the uncertainty introduced

by discretization and time-averaging in two-fluid model predictions', *AIChE Journal*, 63(12), pp. 5343–5360. doi:10.1002/aic.15868.

Takahashi, T. *et al.* (2001) 'Mechanisms and scale effects of skin-friction reduction by microbubbles', *Proc. 2nd Symp. smart Control Turbul.*, pp. 1–9.

Tanaka, T. *et al.* (2022) 'Frictional drag reduction caused by bubble injection in a turbulent boundary layer beneath a 36-m-long flat-bottom model ship', *Ocean Engineering*, 252(April), p. 111224. doi:10.1016/j.oceaneng.2022.111224.

Terwisga, V. (2016) 'On the physical mechanisms for the numerical modelling of flows around air lubricated ships', in *Proceedings of the12th International Conference on Hydrodynamics - ICHD 2016*.

Terziev, M., Tezdogan, T. and Incecik, A. (2022) 'Scale effects and full-scale ship hydrodynamics: A review', *Ocean Engineering*, 245(December 2021), p. 110496. doi:10.1016/j.oceaneng.2021.110496.

Tsai, J.-F. and Chen, C.-C. (2011) 'Boundary Layer Mixture Model for a Microbubble Drag Reduction Technique', *ISRN Mechanical Engineering*, 2011, pp. 1–9. doi:10.5402/2011/405701.

Verschoof, R.A. *et al.* (2016) 'Bubble Drag Reduction Requires Large Bubbles', *Physics Review Letters*, 117(September), pp. 1–4. doi:10.1103/PhysRevLett.117.104502.

Vijayan, S.N. *et al.* (2018) 'Cfd analysis of frictional drag reduction on the underneath of ship's hull using air lubrication system', *International Journal of Mechanical Engineering and Technology*, 9(4), pp. 408–416.

Watanbe, O., Masuko, A., and Shirase, Y. (1998) 'Measurements of drag reduction by microbubbles using very long ship models', *Journal of the Society of Nacal Architects Japan*, 183, pp. 53–63.

Weisheit, J. *et al.* (2021) 'Validation of a flow channel to investigate velocity profiles of friction-reducing ship coatings', *TransNav*, 15(1), pp. 225–231. doi:10.12716/1001.15.01.24.

Wendy C. Sanders, Erics S. Winkel, David R. Downing, M.P. and S.L.C. (2006) 'Bubble friction drag reduction in a high-Reynolds-number flat-plate turbulent boundary layer',

Journal of Fluid Mechanics, 552, pp. 353–380. doi:10.1017/S0022112006008688.

Whelan, J.R. (2004) *WETDECK SLAMMING OF HIGH-SPEED CATAMARANS WITH A CENTRE BOW*.

Winkel, E.S., Ceccio, S.L., Dowling, D.R. and Perling, M. (2004) 'Bubble Size distribution produced by wal-injection of air into flowing freshwater, saltwater and surfactant solutions', in *Experimental Fluids*, pp. 802–810.

Wu, S.J., Ouyang, K. and Shiah, S.W. (2008) 'Robust design of microbubble drag reduction in a channel flow using the Taguchi method', *Ocean Engineering*, 35(8–9), pp. 856–863. doi:10.1016/j.oceaneng.2008.01.022.

Xu, J., Maxey, M.R. and Karniadakis, G.E. (2002) 'Numerical simulation of turbulent drag reduction using micro-bubbles', *Journal of Fluid Mechanics*, 468, pp. 271–281. doi:10.1017/S0022112002001659.

Y.A Hussan, Claudia Del Carmen Gutiérrez-Torres, J. G. Barbosa-Saldaña, J.A.J.-B. (2008) 'Drag reduction by microbubble injection in a channel flow', *REVISTA MEXICANA DE FI´SICA*, 54(1), pp. 8–14.

Yan Yao, Jin-Ling Luo, Kun Zhu, Hai-bo He, Rui Wu, S.Q. (2011) 'STUDY OF MICROBUBBLES FOR SKIN-FRICTION DRAG REDUCTION', *Journal of Hydrodynamics*, 23(1), pp. 65–70.

Zhang, J., Yang, S. and Liu, J. (2019) 'Numerical Investigation of Frictional Drag Reduction with An Air Layer Concepton The Hull of Ship', *Journal of Hydrodynamics* [Preprint]. doi:10.1007/s42241-019-0063-8.

Zhao, X. and Zong, Z. (2022) 'Experimental and numerical studies on the air-injection drag reduction of the ship model', *Ocean Engineering*, 251(November 2021), p. 111032. doi:10.1016/j.oceaneng.2022.111032.

Appendix A – CFD Set Up Details

A.1 Domain Sizes

A.1.1 Domain Size Same Size Plate

Table 39: Table of Domain Size for 0.5 m Depth

Domain Size Model 0.5 m Depth		
Axis	(m)	(m)
X	5	12
Y	5	5
Z	5	5.5

Table 40: Table of Domain Size for 2 m Depth

Domain Model 2 m Depth		
Axis	(m)	(m)
X	5	12
Y	5	5
Z	5	7

Table 41: Table of Domain Size for 3.5 m Depth

Domain Size Model 3.5 m Depth		
Axis	(m)	(m)
X	5	12
Y	5	5
Z	5	8.5

Table 42: Table of Domain Size for 5 m Depth

Domain Size Model 5 m Depth		
Axis	(m)	(m)
X	5	12
Y	5	5
Z	5	10

Table 43: Table of Domain Size for 6.5 m Depth

Domain Size Model 6.5 m Depth		
Axis	(m)	(m)
X	5	12
Y	5	5
Z	5	11.5

A.1.2 Domain Size Reynolds Number Testing

Table 44: Table of Domain Size for 2.74E+07 Testing

Domain Size Model *2.74E+07*		
Axis	(m)	(m)
x	7	16.8
y	7	7
z	7	7.5

Table 45: Table of Domain Size for Re 2.68E+08 Testing

Domain Size Re Model *2.68E+08*		
Axis	(m)	(m)
x	32	76.8
y	32	32
z	32	32.5

Table 46: Table of Domain Size for Re 1.22E+09 Testing

Domain Size Model *1.22E+09*		
Axis	(m)	(m)
x	88	211.2
y	88	88
z	88	88.50

A.1.3 Domain Size Scaling up Plate Testing

Table 47: Table of Towing Tank Size for Medium Plate in Scaling Testing

Domain Size Medium Plate		
Axis	(m)	(m)
x	-35	84
y	-35	35
z	-38.5	35

Table 48: Table of Domain Size for Full-Size Plate in Scaling Testing

Domain Size Large		
Axis	(m)	(m)
x	65	126
y	65	65
z	-71.5	65

A.2 Meshing Details

A.2.1 Meshing Details Same Size Plate

Table 49: Table of Meshing Details for Same Size Plate Testing

Velocity (m/s)	y+	No. of Prism Layers	B.L. Thickness	P.L. Thickness	Time Step
1.93	6.50E-06	31	0.0725	0.0737	0.00647
2.18	5.80E-06	32	0.0707	0.0855	0.00573
2.43	5.20E-06	32	0.0692	0.0767	0.00514
2.68	4.80E-06	32	0.0679	0.0708	0.00466
2.93	4.40E-06	33	0.0667	0.0844	0.00426

A.2.2 Meshing Details Reynolds Number Testing

Table 50: Table of Meshing Details for Reynolds Number Testing

Velocity (m/s)	y+	No. Of Prism Layers	B.L. Thickness	P.L. Thickness	Time Step	Re
3.48	3.80E-06	34	0.0843	0.0947	0.00502	*2.74E+07*
7.45	2.10E-06	40	0.2442	0.2528	0.01073	*2.68E+08*
12.35	1.40E-06	45	0.4957	0.6258	0.01781	*1.22E+09*

A.2.3 Meshing Details Scaling up Plate Testing

Table 51: Table of Meshing Details for Medium Plate Scaling up Plate Testing

Velocity (m/s)	y+	No. Of Prism Layers	B.L. Thickness	P.L. Thickness	Time Step	Re
5.11	5.90E-06	37	0.2829	0.3233	0.01713	*2.01E+08*
5.77	5.30E-06	37	0.2761	0.2904	0.01517	*2.27E+08*
6.43	4.80E-06	38	0.2702	0.3419	0.01360	*2.53E+08*
7.09	4.40E-06	38	0.2649	0.3134	0.01234	*2.79E+08*
7.75	4.00E-06	38	0.2602	0.2849	0.01128	*3.05E+08*

Table 52: Table of Meshing Details for Full Size Plate Scaling up Plate Testing

Velocity	y+	No. of Prism Layers	B.L. Thickness	P.L. Thickness	Time Step	Re
6.96	4.60E-06	40	0.4363	0.5538	0.02335	*5.09E+08*
7.86	4.10E-06	40	0.4255	0.4936	0.020674	*5.75E+08*
8.76	3.70E-06	40	0.4166	0.4454	0.018547	*6.40E+08*
9.66	3.40E-06	40	0.4086	0.4091	0.016816	*7.06E+08*
10.56	3.10E-06	41	0.4014	0.4851	0.015382	*7.72E+08*

Appendix B – Injection Parameters

B.1 Same Plate Testing Appendix

B.1.1 Mass Flow Rates Used

Table 53: Mass Flow Rates for α 0.1

Mass Flow Rates kg/s						
Depth (m)	**Density (kg/m^3)**	**0.42 Fr**	**0.38 Fr**	**0.35 Fr**	**0.35 Fr**	**0.28 Fr**
0.5	1.192	*0.027*	*0.025*	*0.023*	*0.021*	*0.019*
2	1.373	*0.031*	*0.029*	*0.027*	*0.025*	*0.022*
3.5	1.562	*0.035*	*0.033*	*0.031*	*0.028*	*0.025*
5	1.726	*0.039*	*0.037*	*0.034*	*0.031*	*0.028*
6.5	1.916	*0.044*	*0.041*	*0.037*	*0.034*	*0.031*

Table 54: Mass Flow Rate for α 0.4

Mass Flow Rates kg/s						
Depth (m)	**Density (kg/m^3)**	**0.42 Fr**	**0.38 Fr**	**0.35 Fr**	**0.35 Fr**	**0.28 Fr**
0.5	1.192	*0.108*	*0.101*	*0.093*	*0.086*	*0.078*
2	1.373	*0.125*	*0.116*	*0.107*	*0.098*	*0.089*
3.5	1.562	*0.142*	*0.132*	*0.122*	*0.112*	*0.102*
5	1.726	*0.157*	*0.146*	*0.135*	*0.124*	*0.112*
6.5	1.916	*0.174*	*0.162*	*0.150*	*0.137*	*0.125*

Table 55: Mass flow rate for α 0.5

Mass Flow Rates kg/s						
Depth (m)	Density (kg/m^3)	0.42 Fr	0.38 Fr	0.35 Fr	0.35 Fr	0.28 Fr
0.5	1.192	0.135	0.126	0.117	0.107	0.097
2	1.373	0.156	0.145	0.134	0.123	0.112
3.5	1.562	0.177	0.165	0.153	0.140	0.127
5	1.726	0.196	0.183	0.169	0.155	0.140
6.5	1.916	0.218	0.203	0.187	0.172	0.156

Table 56: Mass Flow Rate for α 0.6

Mass Flow Rates kg/s						
Depth (m)	Density (kg/m^3)	0.42 Fr	0.38 Fr	0.35 Fr	0.35 Fr	0.28 Fr
0.5	1.192	0.163	0.151	0.140	0.128	0.116
2	1.373	0.187	0.174	0.161	0.148	0.134
3.5	1.562	0.213	0.198	0.183	0.168	0.152
5	1.726	0.235	0.219	0.203	0.186	0.168
6.5	1.916	0.261	0.243	0.225	0.206	0.187

Table 57: Mass Flow Rate for α 0.9

Mass Flow Rates kg/s						
Depth (m)	Density (kg/m^3)	0.42 Fr	0.38 Fr	0.35 Fr	0.35 Fr	0.28 Fr
0.5	1.192	*0.244*	*0.227*	*0.210*	*0.192*	*0.175*
2	1.373	*0.281*	*0.261*	*0.242*	*0.221*	*0.201*
3.5	1.562	*0.319*	*0.297*	*0.275*	*0.252*	*0.229*
5	1.726	*0.353*	*0.329*	*0.304*	*0.278*	*0.253*
6.5	1.916	*0.392*	*0.365*	*0.337*	*0.309*	*0.280*

B.1.2 Drag Reduction Results

Table 58: Results from 0.1 Testing

Drag Reduction (%)					
Depth (m)	**0.28 Fr**	**0.31 Fr**	**0.35 Fr**	**0.38 Fr**	**0.42 Fr**
0.5	*52.64*	*45.63*	*50.54*	*42.68*	*41.31*
2	*26.36*	*33.21*	*28.43*	*36.66*	*33.76*
3.5	*-19.14*	*8.79*	*15.56*	*32.73*	*24.64*
5	*-14.83*	*-12.05*	*7.59*	*19.89*	*17.99*
6.5	*-41.36*	*-28.73*	*-7.36*	*0.46*	*5.29*

Table 59: Results from 0.4 Testing

Drag Reduction (%)					
Depth (m)	**0.28 Fr**	**0.31 Fr**	**0.35 Fr**	**0.38 Fr**	**0.42 Fr**
0.5	*75.94*	*76.14*	*79.31*	*79.68*	*79.59*
2	*51.32*	*58.76*	*63.40*	*65.91*	*65.71*
3.5	*22.91*	*37.71*	*47.42*	*54.56*	*57.57*
5	*-9.47*	*19.64*	*31.56*	*40.85*	*46.67*
6.5	*-41.30*	*-3.62*	*14.83*	*27.69*	*35.97*

Table 60: Results from 0.5 Testing

Drag Reduction (%)					
Depth (m)	**0.28 Fr**	**0.31 Fr**	**0.35 Fr**	**0.38 Fr**	**0.42 Fr**
0.5	*76.19*	*77.19*	*79.80*	*80.72*	*81.58*
2	*51.90*	*59.98*	*64.28*	*67.82*	*68.53*
3.5	*23.35*	*39.19*	*46.54*	*54.86*	*59.34*
5	*-14.63*	*20.59*	*32.59*	*40.50*	*48.06*
6.5	*-44.66*	*-14.45*	*15.47*	*28.19*	*36.58*

Table 61: Drag Reduction from 0.6 Testing

Drag Reduction (%)					
Depth (m)	**0.28 Fr**	**0.31 Fr**	**0.35 Fr**	**0.38 Fr**	**0.42 Fr**
0.5	*76.28*	*78.16*	*80.46*	*76.60*	*78.46*
2	*46.97*	*60.63*	*63.73*	*67.36*	*69.86*
3.5	*24.98*	*38.38*	*48.46*	*54.24*	*58.72*
5	*-13.91*	*7.27*	*33.16*	*40.69*	*48.09*
6.5	*-39.26*	*-18.15*	*5.61*	*26.29*	*37.62*

Table 62: Drag Reduction from 0.9 Testing

Drag Reduction (%)					
Depth (m)	**0.28 Fr**	**0.31 Fr**	**0.35 Fr**	**0.38 Fr**	**0.42 Fr**
0.5	*54.03*	*58.99*	*58.40*	*59.92*	*59.82*
2	*32.68*	*49.21*	*44.28*	*49.25*	*53.67*
3.5	*0.75*	*20.19*	*26.61*	*34.86*	*39.33*
5	*-18.43*	*0.11*	*10.63*	*20.61*	*28.91*
6.5	*-45.42*	*-20.66*	*-6.03*	*8.52*	*18.15*

B.1.3 Sigma Data

Table 63: Table of 0.1 Sigma Values

0.1	
D.R.	Sigma
52.64	4.02971E-07
50.54	3.84825E-07
45.62	3.93273E-07
42.67	3.77362E-07
41.3	3.7069E-07
36.65	4.34358E-07
33.76	4.26679E-07
33.21	4.52672E-07
32.73	4.9433E-07
28.42	4.42949E-07
26.36	4.63835E-07
24.63	4.85591E-07
19.88	5.46137E-07
17.99	5.36481E-07
15.55	5.04107E-07
8.79	5.15172E-07
7.58	5.56938E-07
5.29	5.95486E-07
0.45	6.06203E-07

Table 64: Table of 0.4 Sigma Values

0.4	
D.R.	Sigma
79.68	1.50945E-06
79.59	1.48276E-06
79.31	1.5393E-06
76.14	1.57309E-06
75.94	1.61188E-06
65.91	1.73743E-06
65.71	1.70672E-06
63.4	1.7718E-06
58.76	1.81069E-06
57.57	1.94236E-06
54.56	1.97732E-06
51.32	1.85534E-06
47.42	2.01643E-06
46.67	2.14593E-06
40.85	2.18455E-06
37.71	2.06069E-06
35.97	2.38194E-06
31.56	2.22775E-06
27.69	2.42481E-06
22.91	2.11151E-06
19.64	2.27665E-06
14.83	2.47277E-06

Table 65: Table of 0.5 Sigma Values

0.5	
D.R..	Sigma
81.58	1.85345E-06
80.72	1.88681E-06
79.80	1.92413E-06
77.19	1.96636E-06
76.19	2.01485E-06
68.53	2.1334E-06
67.82	2.17179E-06
64.28	2.21475E-06
59.98	2.26336E-06
59.34	2.42795E-06
54.86	2.47165E-06
51.90	2.31918E-06
48.06	2.68241E-06
46.54	2.52053E-06
40.50	2.73068E-06
39.19	2.57586E-06
36.58	2.97743E-06
32.59	2.78469E-06
28.19	3.03102E-06
23.35	2.63938E-06
20.59	2.84582E-06
15.47	3.09096E-06

Table 66: Table of 0.6 Sigma Values

0.6	
D.R.	Sigma
80.46	2.31E-06
78.46	2.22E-06
78.16	2.36E-06
76.60	2.26E-06
76.28	2.42E-06
69.86	2.56E-06
67.36	2.61E-06
63.73	2.66E-06
60.63	2.72E-06
58.72	2.91E-06
54.24	2.97E-06
48.46	3.02E-06
48.09	3.22E-06
46.97	2.78E-06
40.69	3.28E-06
38.38	3.09E-06
37.62	3.57E-06
33.16	3.34E-06
26.29	3.64E-06
24.98	3.17E-06
7.27	3.41E-06
5.61	3.71E-06

Table 67: Table of 0.9 Sigma Values

0.9	
D.R.	Sigma
59.92	3.3963E-06
59.82	3.3362E-06
58.99	3.5395E-06
58.40	3.4634E-06
54.03	3.6267E-06
53.67	3.8401E-06
49.25	3.9092E-06
49.21	4.0741E-06
44.28	3.9865E-06
39.33	4.3703E-06
34.86	4.449E-06
32.68	4.1745E-06
28.91	4.8283E-06
26.61	4.537E-06
20.61	4.9152E-06
20.19	4.6366E-06
18.15	5.3594E-06
10.63	5.0124E-06
8.52	5.4558E-06
0.75	4.7509E-06
0.11	5.1225E-06

B.2 Reynolds Number Testing Data

B.2.1 Mass Flow Rates Used

Table 68: Table of Mass Flow Rates used in Reynolds Testing

Mass Flow Rate for Reynolds Testing Kg/s			
	Mixing Ratios		
Reynolds Number	0.4	0.5	0.6
$2.74x10^7$	*0.163*	*0.203*	*0.244*
$2.68x10^8$	*1.009*	*1.262*	*1.514*
$1.22x10^9$	*3.397*	*4.246*	*5.095*

B.3 Scaling Up Testing Data

B.3.1 Mass Flow Rates Used

Table 69: Table of Mass Flow Rate used in Medium Plate for Scaling Tests

Mass Flow Rate Kg/s			
	Mixing Ratios		
Fr	0.4	0.5	0.6
0.28	7.349	9.187	11.024
0.31	8.101	10.127	12.152
0.35	8.837	11.046	13.255
0.38	9.557	11.946	14.335
0.42	10.263	12.829	15.395

Table 70: Table of Mass Flow Rate used in Large Plate for Scaling Tests

Mass Flow Rate Kg/s			
	Mixing Ratios		
Fr	0.4	0.5	0.6
0.28	35.181	43.976	52.771
0.31	38.782	48.477	58.172
0.35	42.300	52.876	63.451
0.38	45.748	57.184	68.621
0.42	49.131	61.414	73.696